A

Presented to
the faculty of the School of Engineering and Applied Science
University of Virginia

in partial fulfillment
of the requirements for the degree

by

APPROVAL SHEET

This

is submitted in partial fulfillment of the requirements
for the degree of

Author:

Advisor:

Advisor:

Committee Member:

Committee Member:

Committee Member:

Committee Member:

Committee Member:

Committee Member:

Accepted for the School of Engineering and Applied Science:

Jennifer L. West, School of Engineering and Applied Science

Acknowledgements

I would first like to thank my advisor, Dr. Venkat Lakshmi, for his time and guidance over myself while pursuing this dissertation. Thank you for your constant motivation and feedback during numerous stressful revision processes for publications. You provided me with countless opportunities for networking and valuable internships. Additionally, you introduced me to the scientists at NASA Goddard Space Flight Center, which is home to one of the largest collection of Earth Scientists. Those connections have benefited my research and provided meaningful collaborations.

The scientists at NASA Goddard Space Flight Center deserve acknowledgment for their helpful suggestions and guidance regarding my research. Collaboratively, we have accomplished several publications. Thank you for your time spent revising manuscripts and providing thoughtful feedback. These scientists include Thomas Stanley, Dr. Dalia Kirschbaum, Dr. Nishan Biswas, Dr. Pukar Amatya, Dr. Robert Emberson, and Dr. John Bolten. I would like to specifically thank Thomas and Nishan for their assistance with coding and for your time discussing research strategies. Dalia deserves a special thank you for serving on this dissertation committee. Thank you for all the time spent guiding me in my research, providing internship opportunities, and allowing me to work collaboratively with scientists in the disasters team over the past few years.

My colleagues from the University of Virginia have supported me in my research and provided assistance in various ways. These include Bin, Benjamin, Robin, Runze, Gigi, Jessica, Sophia, Daniela, Avery, Ziyue, Duc, Aashutosh, Prakrut, Hung, and Hyung. Thank you all for facilitating the progression my research and providing feedback. Also, thank you for your friendship and continued support. I would like to give special acknowledgement to Dr. Bin Fang for the time you spent assisting me with coding and providing datasets for application in my research.

I would also like to thank the members of my dissertation committee. Thank you, Dr. Jon Goodall, serving as the chair of my committee, and Dr. Jim Smith and Dr. Matthew Reidenbach. I would like to thank you for your time commitment and providing meaningful feedback and encouraging the progression of my research.

My education has been influenced by numerous teachers, professors, and advisors. I would like to acknowledge my high school teachers, Richard Swayne, Denise Basham, Diane Stubbins, and Jennings Custis. Additionally, I want to thank Dr. Kenneth Pestka, Dr. Charles Ross, Dr. Timothy Holmstrom, and Dr. Joseph Garcia, as well as my undergraduate advisor, Dr. Michelle Parry, for their encouragement in my research and education at Longwood University.

Finally, I would like to acknowledge my family— my mother, step-father, and grandparents. You motivated me that I was capable of pursuing a PhD. Thank you for your constant support and encouraging me to be healthy and productive.

Table of Contents

List of Tables

List of Figures

Abstract

Landslides can result in devastating loss of life and property damage and are a growing concern from a local to global scale. In recent years, increased rainfall-triggered landslide events in the Lower Mekong River Basin (LMRB) have put communities at increased risk of damage from these disasters. This dissertation focuses on how remote sensing can be used to address landslide hazard at global scale and specifically in the Lower Mekong region. In the first part of this research, two satellite-based rainfall products, CHIRPS and TMPA, were compared with daily rain gauge observations from 2000 to 2014 in the Lower Mekong River Basin. Both products showed higher correlation with in-situ data during the wet season (June–September) as compared to the dry season (November–January). Our validation test showed TMPA to correctly detect precipitation or no-precipitation 64.9% of all days and CHIRPS 66.8% of all days, compared to daily in-situ rainfall measurements, indicating CHIRPS may be better at representing precipitation in this region. The second part of this research, the influence of land use and land cover (LULC) change and other causative factors of landslide susceptibility are evaluated in the LMRB using Frequency Ratio analysis and Logistic Regression models. Results indicate LULC change from agricultural land to forest have a positive correlation with landslide occurrence. However, the most statistically significant factors in the models are found to be slope and distance to roads. The third part of this research evaluates global patterns in landslide reporting from events in the Global Landslide Catalog. The most notable landslide hotspots are in the Pacific Northwest of North America, High Mountain Asia, and the Philippines. More landslides are reported in areas with high population density compared to remote locations. A bias towards English-speaking countries was also discovered in the catalog reports. Finally, the last part of this research assesses how remotely sensed hydrological products can be used to improve rainfall-triggered landslide monitoring and prediction in data-sparse regions like the Lower Mekong. High-resolution soil moisture is better able to capture the soil moisture profile than coarser resolutions. By incorporating high resolution soil moisture we can better investigate landslide hazard and prediction and evaluate landslide prone areas. The results of this dissertation can be used in local decision making and disaster preparation and mitigation in the Lower Mekong River Basin.

1. Chapter 1. Introduction

The Lower Mekong River Basin (LMRB) in Southeast Asia is particularly susceptible to precipitation-based natural disasters and is heavily dependent on proper water resource management to adequately sustain the more than 60 million inhabitants in the region whose livelihoods depend on the food and agriculture provided by the Mekong River and its many tributaries (Trisurat et al., 2017). The portion of the Mekong River in the lower basin is 1,485 miles (2,390 km) in length and drains into northeastern Thailand, the western slopes of Laos and Vietnam, and the majority of Cambodia, before reaching the ocean through the delta in southern Vietnam as shown in Figure 1.1. (Owen et al., 2023). In this region, rainfall seasonality causes droughts and floods that can negatively affect local resources associated with fishing and agriculture (Simery & Kean, 2009). Encompassing multiple countries, the Mekong River arouses conflict and collaboration among Cambodia, Laos, Thailand, and Vietnam regarding water resources (Owen et al, 2023). Being the most important river in southeast Asia, the Mekong is a significant water source and provides renewable energy and food security to people in the region. Increasing development and population demand alongside changes in climate are threatening the important resources in this region as more extreme precipitation and subsequent natural disasters like flooding and landslides are predicted (Try et al., 2020).

The climate of the LMRB is described as tropical monsoonal, and precipitation is dominated by the Southwest Monsoon. The monsoon season typically occurs from June to November, and the dry season ensues from December to May (Simery & Kean, 2009). The majority of rainfall occurs during the monsoon season, which is responsible for 80%–90% of the annual precipitation. The Northeastern monsoon wind, typically starting in November in southern regions, produces the dry season until May. Hence, the river flow is usually lowest in April and highest in October. Furthermore, the temperatures in the lower Mekong basin are generally warm throughout the year and exhibit little seasonal variation, with daily lows averaging 74 °F (23 °C) and highs averaging 89 °F (32 °C). However, the temperatures in the northernmost regions of Myanmar experience more seasonal variation (Owen et al., 2023). Precipitation in the lower basin follows an east to west gradient with the highest annual rainfall accumulation (3,000 mm) occurring in

the uplands of Laos and Cambodia and the least accumulation (1,300 mm) occurring in northeast Thailand (Simery & Kean, 2009).

Figure 1.1. Topography and river networks of Southeast Asia (Figure from Owen et al., 2023)

Due to the varying topography and intense rainfall, the LMRB is one of the most landslide-prone areas on the globe (Biswas et al., 2021). Landslides have economic, societal, and environmental impacts, and climate change is causing increased landslide events throughout the LMRB (Liu et al., 2020). Landslides can cause loss of life, damage to property, and negatively affect natural resources. To understand these disasters and reduce risk in the LMRB, landslide susceptibility and hazard analysis must be performed. Efforts have been made to describe and map landslide susceptibility (Stanley et al., 2017; Hong et al., 2007) and predict landslides (Stanley et al., 2021; Farahmand & AghaKouchak, 2013) at global scale but the causative factors of landslides in the LMRB are still not completely understood, and there is gap in the existing literature regarding landslide hazard studies in this region. The research presented here attempts to help fill that gap by addressing landslide hazard using novel applications of various satellite-based products with available in-situ data and statistical and empirical models t in the LMRB.

The LMRB lacks important hydrologic in situ data, and the data available generally are affected by spatial and temporal variability. For example, landslide inventories are a vital component for understanding past and future landslide hazard (Amatya et al., 2022). However landslides are not uniformly recorded between the countries of the LMRB. Often landslides occurring in remote locations go unnoticed and fatal landslides occurring in areas with denser populations are reported more often (Dandridge et al., 2023). The lack of landslide inventories in this region hinders landslide prediction and susceptibility analysis. However, recent advances in landslide mapping techniques and high resolution satellite imagery provides a greater ability to collect landslide information in the LMRB (Amatya et al, 2022). In addition to sparse landslide information, the region lacks altogether a consistent in situ soil moisture network, and limited in situ data is available regarding precipitation and streamflow (Dandridge et al., 2019). Soil moisture, rainfall, and streamflow are significant variables for hydrological modelling and analysis. To supplement the lack of in-situ measurements, remote sensing products can be used (Lakshmi et al., 2023). There have been numerous studies that have shown the benefits of using satellite data in data sparse regions like the LMRB (Fayne et al. 2017; Le et al. 2018; Mohammed et al. 2018; Mondal et al., 2022)

With recent advancements in remote sensing, basin characteristics can be better understood despite the lack of ground measurements and hence provide better management strategies for landslide mitigation.

Near real-time landslide prediction is essential for assessing hazard potential and disaster mitigation (Manconi & Giordan, 2016). In the current literature, various methods and modelling techniques are used for landslide prediction efforts. However, recent advances in machine learning has provided the ability to more reliably and accurately predict landslides (Micheletti et al., 2014). The machine learning algorithms are less susceptible to overfitting to the training data and can handle nonlinear relationships between landslides and causative variables (Wang et al., 2021). Random forest, fuzzy logic, artificial neural network, and extreme gradient boosting (XGBoost) are a few of the common machine learning techniques used for modelling landslide prediction. Numerous studies have applied machine learning methods for landslide prediction in various study locations across the globe. For example, Sahin (2020) compared the ability of several regression tree-based ensemble methods to predict landslides in the Black Sea region of Turkey. The results of their study indicate the XGBoost algorithm to have lower prediction error and higher accuracy results compared to other model frameworks considering a variety of accuracy metrics. Another study by Zhang et al., (2023) applied the XGBoost algorithm to several areas in China and found the model accuracy to be high regarding the ability to predict landslide occurrence despite the varying geomorphology of the regions analyzed. Rabby et al., (2020) found XGBoost to have the best performance and the highest AUC compared to random forest and K-nearest neighbor algorithms. Additionally, the recently updated methodology for NASA's global Landslide Hazard Assessment for Situational Awareness (LHASA) model incorporates the XGBoost machine learning framework for near real-time hazard awareness for landslide risk due to its ability to incorporate monotonicity and interaction constraints and its vast user community (Stanley et al., 2021). While these methods have been widely used, very few efforts have been made to apply machine learning for landslide prediction in the LMRB, a region that would benefit greatly from near real-time landslide assessment particularly during the monsoon season.

In this dissertation, the following broad questions will be addressed:

i. How can remotely-sensed and modelled datasets be applied for landslide hazard assessment in the LMRB to supplement sparse in situ data?

ii. What are the causative factors that contribute to landslide susceptibility in the LMRB? In particular, which dynamic land cover change scenarios influence landslide occurrence?

iii. What are the spatial and temporal patterns, biases, and limitations present in current landslide reporting? Specifically, to what extent are landslides in the LMRB represented in global catalogs?

iv. How can machine learning be applied for landslide prediction in the LMRB?

2. Chapter 2. Evaluation of Satellite-Based Rainfall Estimates in the Lower Mekong River Basin

Associated citations:

(1) Dandridge, C.; Lakshmi, V.; Bolten, J.; Srinivasan, R. Evaluation of Satellite-Based Rainfall Estimates in the Lower Mekong River Basin (Southeast Asia). Remote Sens. 2019, 11, 2709. https://doi.org/10.3390/rs11222709

(2) Dandridge, C., V. Lakshmi, J. Sutton and J. Bolten. (2017), Precipitation estimates and comparison of satellite rainfall data to in situ rain gauge observations to further develop the watershed-modeling capabilities for the Lower Mekong River Basin, H21E-1498 presented at 2017 Fall Meeting, AGU, December 11-15, New Orleans, LA

2.1. Introduction

Precipitation is one of the most important features in the global water and energy system and is vital to effective hydrology and climate research (Tang et al., 2016). Across the globe, precipitation is typically estimated via three methods—ground-based rain gauges, ground radars, and satellite remote sensing (Li et al., 2013). Traditionally, rain gauges are used to measure rainfall due to their accuracy and reliability. In this region, most of the rainfall used for decision-making purposes is measured directly by a multitude of rain gauge stations that cannot effectively reflect the spatial variation of precipitation due to its uneven distribution and limited representation as point measurements (Figure 2.1). Even though rain gauge stations provide the most accurate precipitation measurements, several sub-basins in the LMRB do not contain any gauges. Most sub-basins have very few or no stations and within the basins that do have stations, some stations might only record data for certain years or have temporal gaps in the data recording. The quality of data and techniques for data collection vary throughout the basin, which leads to a precipitation data set with significant spatio-temporal gaps and high latency (Ayehu et al., 2017). With such high limitations, it can take years to obtain suitable data for research. Ground radar systems can be useful in providing the spatial distribution needed for effective precipitation estimates at the basin-scale but could also have shortcomings due to limited area coverage, high costs, and requirements of extensive equipment maintenance (Lou et al., 2015). Therefore, in this study no ground radar data were used. Several studies indicate that high resolution satellite products are an effective alternative to ground and radar methods (Gebremichael et al., 2014; Golian et al., 2015). Allowing for continuous and repetitive rainfall measurements, remotely

sensed satellite precipitation estimates are, thus, very useful in the LMRB due to its large geographic extent. Utilizing remote sensing products and models is essential for addressing hydrological issues in the Mekong region (Mohammed et al., 2018). To effectively utilize satellite-observed precipitation products, their accuracies should be examined over various spatial extents and time periods. Uncertainties can rise from the retrieval algorithm, cloud contamination, and frequency of the satellite overpasses. Knowledge of their uncertainties over varied terrain will also help us to obtain a better understanding of their applications and limitations (Lu et al., 2018).

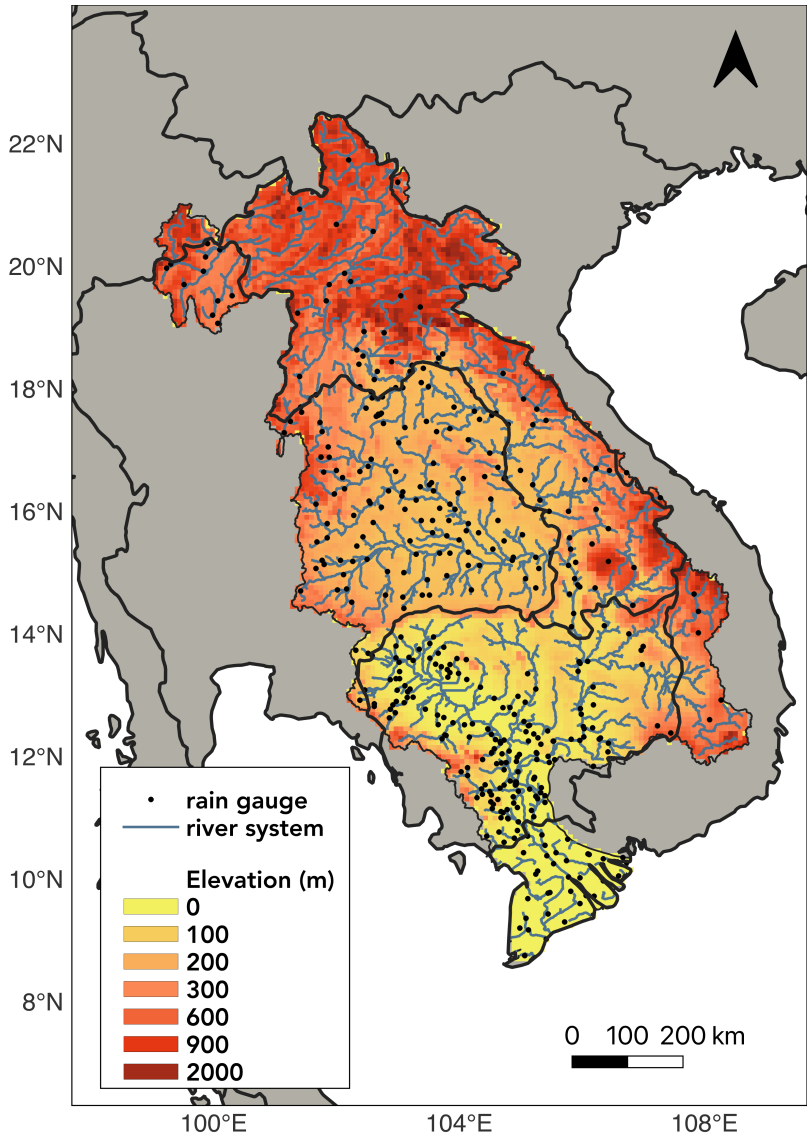

Figure 2.1. Map of the Lower Mekong River Basin in Southeast Asia and the locations of the rain gauge stations within the basin.

The Climate Hazards group Infrared Precipitation with station observations (CHIRPS) and NASA's Tropical Rainfall Measuring Mission (TRMM) Multi-Satellite Precipitation Analysis (TMPA) 3B42 v.7 were evaluated in this study (Funk et al., 2015; Huffman et al., 2016). It is important to note that the TRMM products applied in this study were phased out and replaced by Global Precipitation Mission (GPM) Integrated Multi-Satellite Retrievals for GPM (IMERG) product which has improved spatial and temporal resolution, i.e., 0.1° by 0.1° and half-hourly temporal resolution (Huffman et al., 2015). The IMERG product has also improved upon the biases and uncertainty present in older products. Thus, the results shown here are not expected to correlate closely with GPM IMERG. However, an interesting caveat is that the TRMM combined product was used as a calibration standard for the GPM IMERG algorithm, thus, warranting this inspection of the TMPA product over the Lower Mekong River Basin.

Being a relatively new precipitation product, CHIRPS has been involved in limited precipitation validation studies, but was found to correlate well with in-situ measurements (Xian et al., 2019; Tote et al., 2015; Kimani et al., 2017). These studies are different from our work presented here regarding methodology, study period, and region. For example, an evaluation of CHIRPS was performed by Guo et al. (2017) in the LMRB, but used only 38 rain gauge stations from the Global Summary of the Day (GSOD) for validation of the satellite-based product. They used the criteria of at having 30% or less missing values of the time-series record for considering individual rain gauges. This study found that CHIRPS was able to properly estimate periods of low rainfall that are associated with droughts in the region. An extensive comparison of CHIRPS was evaluated over mainland China by Bai et al. (2018) and used 2,480 stations for validation from 1981 to 2014. These authors evaluated the spatio-temporal aspects of CHIRPS and found it to perform better for large rainfall amounts than arid or semi-arid regions and found a strong relationship between CHIRPS and monsoon movement. Additionally, in this study, CHIRPS was found to perform better in the warm months than winter months due to its limited capability to detect snow. Similarly, several studies have found that TMPA was helpful in addressing a multitude of hydrological problems, such as predicting and monitoring precipitation (Hermance et al., 2018). A similar study by Wang et al. (2017) compared TMPA and GPM precipitation products over the entire Mekong basin, but only used data from 53 rain gauge stations over a 2-

year period from 2014 to 2016. These authors found that both IMERG and TMPA overestimated light rainfall and underestimated large rainfall events, but IMERG performed better overall. Several studies have found TMPA and CHIRPS to be comparable to direct rain gauge measurements in various regions with complex terrains including South America (Blacutt et al., 2015) and Africa (Dinku et al., 2008). Extensive validation studies have been done with TMPA, but these studies have not been conducted over the LMRB or with as many rain gauge stations as in this comparison. There were no previous studies that evaluated CHIRPS for as many years or against as many in-situ stations in the LMRB as the methodology presented here. Using a more extensive in-situ data set with 477 stations from the Mekong River Commission, this study aims to closely analyze TMPA and CHIRPS over the 15-year period from 2000 to 2014. The time period for this study is based on the availability of rain gauge data and satellite-based sensor operation.

This research aims to determine the extent to which the satellite precipitation products TMPA and CHIRPS are able to estimate precipitation in the LMRB and, thus, show their validity for consideration in basin-scale water management decisions. Unlike previous studies in this region of the world, this research uses an extensive in-situ gauge network for validation, satellite estimates were compared against the rain gauge measurement(s) for the same pixel in order to assess the performance of the satellite products. Comparisons were performed based on classifications of the rain gauge locations with respect to rainfall accumulation and elevation to examine the extent to which the amount of rainfall and topography plays a role in their performance. Additionally, a spatial correlation analysis was applied to both the satellite-based products to visualize the geographical relationship with in-situ measurements and assess any spatial bias. The results of this validation study have the ability to improve estimation of water resources and benefit flood and drought forecasting systems in the LMRB by presenting the capabilities and limitations of TMPA and CHIRPS. It is important to note that the final goal of this work was not to estimate floods and extreme events, but to evaluate the performance of satellite precipitation estimates so that future studies can feel confident about using these estimates in their models. This study and further research applying in-situ observations to determine accuracy of satellite product can aid in the improvement of basin-wide decision-making, flood prediction, and management of floodwaters and drought by providing validations

which suggest that satellite estimates can substitute for rain gauge measurements in areas with a sparse or absent in-situ network.

2.2. Data

2.2.1. In-Situ Measurements

Daily precipitation totals were provided by the Mekong River Commission (MRC) from 481 in-situ rain gauge stations located throughout the basin from 1920 to 2014 (Figure 2.1) and were available upon request. For the time period selected in this study, 2000 to 2014, 477 stations in the LMRB had available precipitation measurements for this time period. The rain gauge data set contained gaps where no precipitation measurements were taken during the extended time periods for some stations. Specifically, 21% of the total amount of days from 2000 to 2014 for all rain gauge stations had unavailable or missing rainfall measurements. Gauges were not available consistently across the basin, significantly limiting data availability over large areas of the basin, as a result (Figure 2.1). Additionally, the quantity of rain gauges did not satisfy the size of the LMRB (1 station per 1,580 km^2). Therefore, the data gaps and gauge sparsity in the LMRB make it impractical to use rain gauge data alone for hydrological decision making (Oddo et al., 2018). Here, the available in-situ data served as a validation dataset for evaluating the accuracy of the TMPA and CHIRPS satellite products.

2.2.2. Satellite Retrievals

Launched in 1997, NASA's TRMM Multi-Satellite Precipitation Analysis (TMPA) 3B42 v.7 is one of the most widely used satellite precipitation products and is very useful for hydrometeorological applications in data-sparse regions of the world (Prakash et al., 2013). TMPA combines information from the TRMM precipitation radar, passive microwave and infrared sensors from various satellites, and available rain gauge data to measure tropical rainfall for weather and climate research (Huffman et al., 2016). Monthly in-situ precipitation data were gathered from the Global Precipitation Climatology Project (GPCP) developed by the Global Precipitation Climatological Center (GPCC) and the Climate Assessment and Monitoring System (CAMS) developed by NOAA's Climate Prediction Center (CPC), and were used for calibration

of the TMPA product (Huffman et al., 2007). For a full explanation of the TMPA input datasets and algorithms, please refer to Huffman et al. (2007). Estimates were available at 3-hour intervals with 0.25° by 0.25° spatial resolution for the region 50° S to 50° N. In this study, the final daily product (TRMM_3B42_Daily) derived from the 3-hourly estimate (TRMM_3B42) was used in the analysis.

Climate Hazards Group InfraRed Precipitation with Station data (CHIRPS) is a quasi-global precipitation product that provides estimates for over 30 years (1981 to near-present) and is provided by the Climate Hazards Center (CHC) (Funk et al., 2015). CHIRPS uses a recently produced satellite rainfall algorithm that combines climatology data, satellite precipitation estimates, and in-situ rain-gauge measurements to produce a high resolution precipitation product. It utilizes 0.05° satellite imagery alongside in-situ station data to produce a gridded rainfall product. CHIRPS is widely used for rainfall trend analysis and seasonal drought monitoring. The climate data used in the CHIRPS methodology consists of two in-situ datasets, Agromet Group of the Food and Agriculture Organization of the United Nations (FAO) and Global Historical Climate Network (GHCN). These two data sets are long-term averages and were used to create the climate data used by CHIRPS. The station's historical data were mostly used in the calibration for the CHIRPS method instead of data from this study period, 2000–2014. It was also important to note that the CHIRPS methodology uses the TMPA product to calibrate global Cold Cloud Duration (CCD) precipitation estimates. For full data description please refer to Funk et al., (2015). Although CHIRPS has a higher spatial resolution (0.05°) than TMPA (0.25°), this does not necessarily translate into a higher accuracy. However, higher spatial resolution helps in the characterization of the spatial variability. Here, daily estimates from CHIRPS (CHIRPS Daily Version 2.0 Final) were used in the analysis.

2.3. Methodology

In this study, rain gauge measurements provided by the Mekong River Commission were used as a validation dataset for two satellite-based precipitation products, TMPA and CHIRPS, in a point to pixel comparison via the methodology outlined in Figure 2. First, the measurement value of –9999 was removed from all in-situ data and those were treated as missing observations

and were excluded from analyses. To match the daily satellite-based estimates of rainfall with the rain gauge measurements, the satellite pixel encompassing each rain gauge location was identified. In each pixel, we extracted the satellite-based estimate and paired it with the corresponding rain gauge data at a daily scale from 2000 to 2014. If more than one station was present within a satellite pixel, the rain gauge measurements were averaged before being compared to the satellite-based precipitation estimate in that pixel. Additionally, a validation study was employed to assess the satellite-based product's ability to correctly estimate precipitation (i.e., the rain–no-rain detection problem). This was done by determining the percentage that the satellite-based estimate and gauge measurement in a particular pixel were both wet (accumulating at least 0.06 mm of rainfall) or dry (below 0.06 mm of rainfall) and if one was wet and the other was dry.

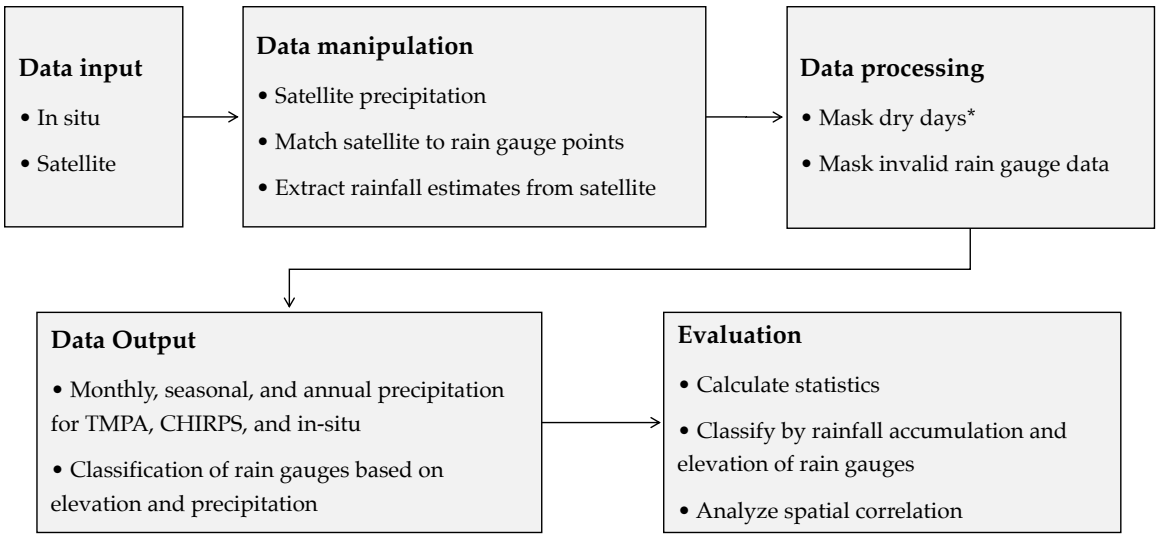

Figure 2.2. Methodology and workflow for this study. *Dry days are days where both satellite-based estimate and rain gauge measurement give a precipitation below the threshold of 0.06 mm. Dry days are excluded in some analyses but not all.

Daily TMPA and CHIRPS estimates and in-situ measurements were separately aggregated to monthly and annual accumulation. Similarly, daily precipitation was aggregated to seasonal

accumulation for comparison. The wet season included accumulations from June through September and the dry season included accumulations from November through February. Additionally, the rain gauges were categorized based on the average annual accumulation in the following ranges—0 to 1,000 mm, 1,001 mm to 1,500 mm, 1,501 mm to 2,000 mm, 2,001 mm to 2,500 mm, and greater than 2,500 mm. Classifying the rain gauges by monthly accumulation would reveal if and to what extent the amount of rainfall received could affect performance of the satellite-based product estimates. The rain gauges were also categorized based on elevation into the following ranges—0 to 100 m, 101 m to 300 m, 301 m to 500 m, 501 m to 1,000 m, and greater than 1,000 m. Classifying the rain gauges by elevation would determine the role topography plays in satellite-based product performance. For the monthly, annual, seasonal, and categorical analyses, dry days (days where the corresponding in-situ measurement and satellite-based estimates were below the threshold of 0.06 mm) were excluded in order to evaluate only days where both the rain gauge and the satellite-based product indicated precipitation. However, the dry days were not excluded from the rain–no-rain validation study described previously so that the days where CHIRPS and TMPA correctly estimated no precipitation from a rain gauge measurement could be counted and evaluated.

Several statistical metrics were employed for analyses between the satellite-based estimates and in-situ measurements. For the linear correlation analysis, the Pearson's correlation coefficient (r-value) was examined. The closer the r-value was to 1, the more highly correlated the satellite-based estimate was to the in-situ data. Bias was defined as the average of the difference between two quantities and showed the tendency of TMPA and CHIRPS to overestimate or underestimate corresponding in-situ measurements. The Root Mean Squared Error (RMSE) was used to assess the goodness of fit between the satellite-based and in-situ datasets. Lower RMSE values indicated a better fit between two variables, which here would imply a high correlation between satellite-based estimates and in-situ data. The Mean Absolute Error (MAE) provided the average of the absolute errors and measured the difference between two continuous variables, mean absolute error was defined as the average of all absolute differences between the two quantities. MAE provides further insight into the correlation between in-situ and satellite-based products. Each of

these statistics was analyzed separately for the monthly, seasonal, and annual data, as well as the categorized data based on rain gauge elevation and rainfall accumulation.

2.4. Results

In the LMRB, there were large variations in precipitation intensity, duration, and accumulation particularly between the dry and wet seasons. We found that these variations were realized differently between the two satellite-based precipitation products, CHIRPS and TMPA. In-situ monthly rainfall accumulation ranged from 0.10 mm to 1,748.0 mm, TMPA measured monthly rainfall from 0.09 mm to 1,279.9 mm, and CHIRPS measured monthly rainfall from 0.06 mm to 1256.0 mm. The dry season in-situ data produced anywhere from 0.30 mm to 612.07 mm per year were averaged over the 15-year study period. On the other hand, TMPA recorded the dry season range to be from 0.17 mm to 292.85 mm and CHIRPS from 1.07 mm to 692.93 mm. The wet season produced rainfall accumulation from 170.25 mm to 2,709.70 mm according to in-situ data, whereas TMPA estimated a range from 86.46 mm to 1,454.66 mm and CHIRPS estimated from 110.99 mm to 2,138.24 mm. In-situ cumulative annual rainfall ranged from 4.00 mm to 4,551.50 mm, TMPA measured annual rainfall from 3.72 mm to 3,029.82 mm, and CHIRPS measured annual rainfall from 1,376.9 mm to 2,136.4 mm. While the elevation decreased from greater than 2,000 m in the Northern reaches of the basin to the Southern Vietnam Delta at sea level, the precipitation followed an East to West gradient, with most rainfall accumulation in Vietnam, Laos, and Eastern Cambodia. Western parts of Thailand and Cambodia received the least amount of rainfall. Figure 2.3. shows the rainfall distribution patterns geographically for the dry, wet, and annual datasets derived from 2000 to 2014. Both CHIRPS and TMPA were able to represent the rainfall distribution over the basin in the dry season that was indicated by the rain gauges in Figure 2.3., although CHIRPS estimated much more precipitation in the Western part of the basin in Vietnam. A similar trend appeared in the wet season and the annual maps in Figure 2.3., such that TMPA and CHIRPS showed similar rainfall distributions over the LMRB with CHIRPS having slightly higher estimations. The annual distribution was very similar, aside from the satellite overestimating gauge measurements in several areas. Satellite-based estimates showed higher correlation with rain gauge measurements during the dry season and lower

correlation during the wet season where the in-situ data recorded much lower rainfall accumulation than the satellite-based estimation. Table 2.1 explains the rain–no-rain detection accuracy by CHIRPS and TMPA, when compared to the rainfall recorded by rain gauges. CHIRPS correctly detected rain 21.9% of the time and TMPA correctly detected rain 15.7% of the time, compared to the daily rainfall. CHIRPS agreed with the in-situ for no-rain days 44.9% of the time and TMPA agreed with in-situ for no-rain days 49.1% of the time. However, both TMPA and CHIRPS estimated rain for more than 20% of the days when the rain gauges did not measure any precipitation. CHIRPS agreed with in-situ 66.8% for rain or no-rain days and TMPA agreed with in-situ 64.9% for rain or no-rain days (Table 2.1). The validation study showed that CHIRPS was better able to estimate whether a dry or wet day was present.

Table 2.1. Rain–no-rain validation study results for daily precipitation from 2000–2014.

	CHIRPS - No Rain	CHIRPS - Rain
Rain Gauge - No Rain	44.9%	26.4%
Rain Gauge - Rain	6.8%	21.9%
	TMPA - No Rain	TMPA - Rain
Rain Gauge - No Rain	49.1%	22.3%
Rain Gauge - Rain	13.0%	15.7%
	Correct Detection	Incorrect Detection
CHIRPS	66.8%	33.2%
TMPA	64.9%	35.1%

For further analysis, the rain gauges were classified by the following ranges for annual accumulation—0 to 1,000 mm, 1,001 mm to 1,500 mm, 1,501 mm to 2,000 mm, 2,001 mm to 2,500 mm, and greater than 2,500 mm. Table 2.2 shows the analysis based on monthly rainfall accumulation, which analyzes the r-value, bias, MAE, and RMSE. For stations receiving more than 2,500 mm of annual rainfall, CHIRPS had an r-value of 0.83 and TMPA had an r-value of 0.65. Both CHIRPS and TMPA had better correlation with each subsequent accumulation category, indicating that the satellite-based products performed better in areas with high precipitation. There was no apparent relationship between the number of stations in each category in Table 2.2 and the correlation between in-situ and satellite-based estimates. CHIRPS detected rainfall in each class significantly better than TMPA. To visualize the monthly

correlations, Figure 2.4 shows a side-by-side boxplot comparison between the satellite-based and in-situ measurements of the average monthly rainfall accumulation from 2000 to 2014. The

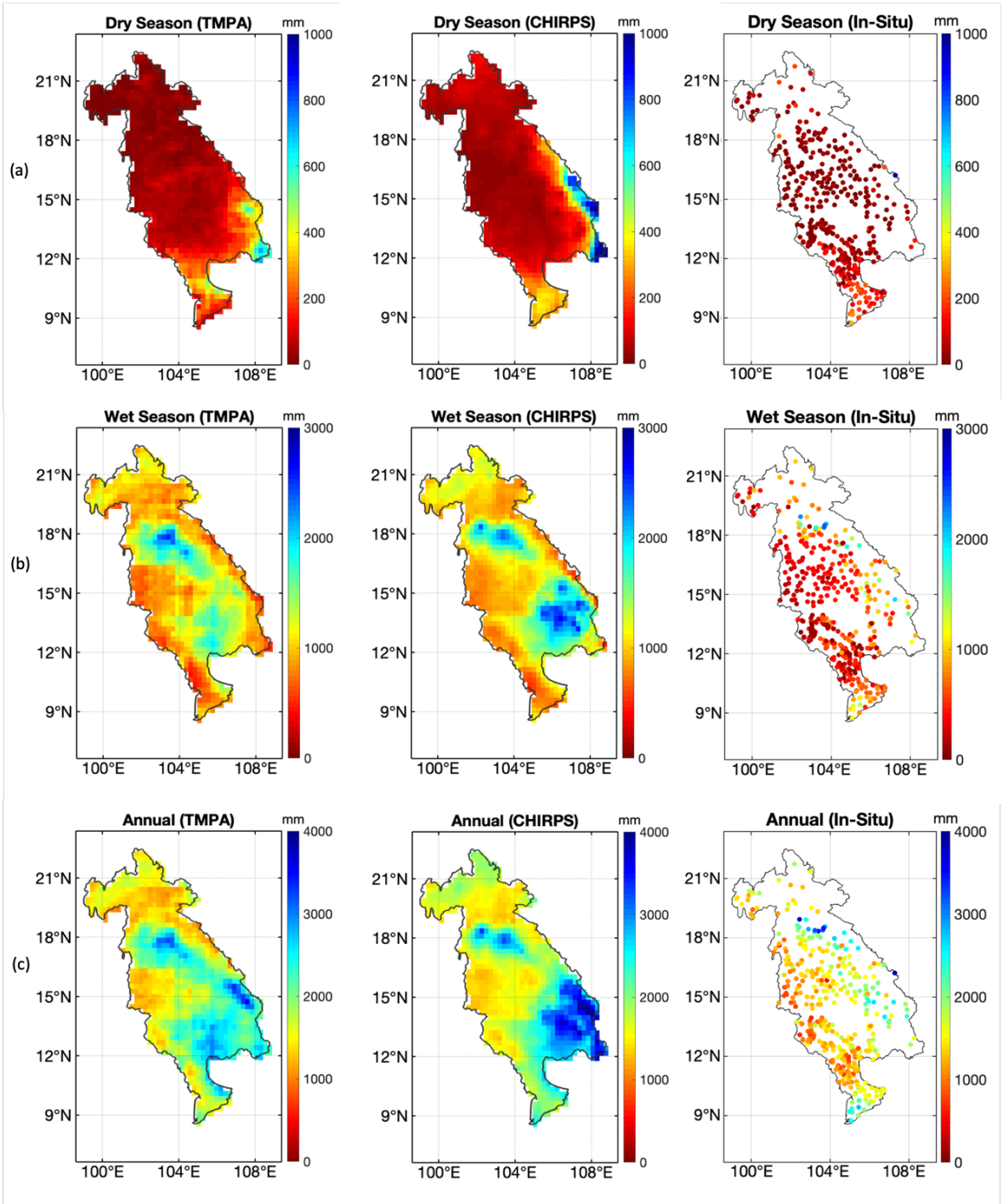

Figure 2.3. Rainfall Distribution in Lower Mekong River Basin. (a) Average (average over 2000 to 2014) seasonal rainfall accumulation during the dry season (November to February) for Tropical Rainfall Measuring Mission (TRMM) Multi-Satellite Precipitation Analysis (TMPA), Climate Hazards Group InfraRed Precipitation with Station (CHIRPS), and in-situ. (b) Average seasonal

rainfall accumulation during the wet season (June to September) for TMPA, CHIRPS, and in-situ. (c) Average annual rainfall accumulation for TMPA, CHIRPS, and in-situ.

seasonal data sets used in this study were configured from this plot using the four highest precipitation months (June, July, August, and September) for the wet season and the four lowest precipitation months (November, December, January, February) for the dry season. The satellite-based estimates overestimated rain gauges during the peak of the wet season (July and August) (Figure 2.4.). Further, TMPA and CHIRPS both recorded July as the peak of the wet season (the month with the highest average rainfall accumulation), whereas the rain gauges showed August to be the peak of the wet season. Similarly, TMPA and CHIRPS indicated January as the lowest accumulation of precipitation, whereas the rain gauges showed February to be the month with lowest rainfall accumulation. In each of the three boxplots, October had the highest variance in cumulative precipitation from 2000 to 2014, denoted by the largest vertical black bars. To this end, the months receiving lower rainfall amounts showed higher correlation between the satellite-based and in-situ measurements than the months receiving higher rainfall amounts. Figure 2.5. shows the time-series trend from the satellite-based estimates and provides a closer look of comparison on a monthly scale. From the time-series we conclude that the estimates from both CHIRPS and TMPA were closely correlated with the seasonal patterns of the in-situ measurements (Figure 2.5.).

Table 2.2. Comparison statistic results between rain gauge measurements and satellite-based precipitation estimates for monthly rainfall classes based on in situ accumulation from 2000 to 2014 for R, bias, mean absolute error (MAE), and RMSE.

In-Situ Annual Accumulation	Satellite-Based Product	r-value	Bias (mm)	MAE (mm)	RMSE (mm)
0 – 1000 mm	CHIRPS	0.72	-31.28	43.44	63.45
	TMPA	0.51	5.55	43.78	65.88
1001 – 1500 mm	CHIRPS	0.75	-36.28	52.52	76.49
	TMPA	0.56	9.82	59.48	91.72
1501 – 2000 mm	CHIRPS	0.79	-33.52	58.23	87.77

	TMPA	0.61	0.85	67.74	103.98
2001 – 2500 mm	CHIRPS	0.82	-31.01	72.28	117.38
	TMPA	0.64	-29.10	84.29	136.75
> 2500 mm	CHIRPS	0.83	-46.59	97.78	161.46
	TMPA	0.65	-88.51	129.40	208.06

For further comparison of the data products, the correlation coefficient, bias, MAE, and RMSE were determined. During the wet season, TMPA underestimated the rain gauge measurements more than during the dry season. The correlation coefficient (r-value) between the rain gauge and TMPA estimates was 0.38 for dry the season comparison, 0.48 for the wet season comparison, 0.49 for the annual comparison (Table S2). The CHIRPS comparison showed an r-value of 0.61 for the dry season comparison, 0.68 for the wet season comparison, and 0.58 for the annual comparison (Table S3). The average MAE for the comparison between in-situ and TMPA was 0.07 mm for the dry season comparison, –1.26 mm for the annual comparison, and –17.37 mm for the wet season comparison (Table S2). The comparison between CHIRPS and in-situ produced average MAE values of –2.81 mm for the dry season comparison, –23.91 mm for the annual comparison, and –162.46 mm for the wet season comparison (Table S3). Overall, TMPA and CHIRPS both correlated better during the wet seasons than the dry seasons most likely due to the low variance in the estimates from the dry season. The correlation between TMPA satellite-based estimates and rain gauge measurements in this study was ordered (from most correlation to least correlation) as follows—annual comparison, wet season comparison, monthly comparison, and lastly dry season comparison. However, CHIRPS correlated as follows—wet season, dry season, annual, and monthly.

Table 3 shows that the rain gauges were categorized based on their elevation and were used for analysis at different rainfall accumulation classes. They were classified into the following categories—0 to 100 m, 101 m to 300 m, 301 m to 500 m, 501 m to 1,000 m, and greater than 1,000 m subsets by quantile bins. From this table, we conclude that neither CHIRPS nor TMPA were significantly impacted by elevation nor was the correlation affected by the number of stations in

each category. CHIRPS was more highly correlated to in situ measurements for rain gauges at elevations between 101 m and 300 m, with an average r-value of 0.84 for these stations. TMPA also showed a better agreement with the in-situ data in this elevation category, but had an r-value of 0.69. At stations with elevations above 1,000 m, CHIRPS performed much better than TMPA, having an r-value of 0.81 as compared to TMPA which had an r-value of 0.54. It is important to note that as the elevation range increased, the number of rain gauges that fall within the subsequent category decreased. This could have affected the results of the study since each elevation category had unequal number of rain gage stations.

For spatial correlation analysis, the r-value at each station was determined based on the monthly rainfall accumulation and was plotted at each station location. The r-values could be visualized for CHIRPS and TMPA in Figure 6 and Figure 7, respectively. When comparing these two figures, it was apparent that CHIRPS was more highly correlated for the majority of all rain gauge stations across the basin than TMPA. CHIRPS did not display a distinct spatial pattern of correlation (Figure 6). Most stations had an r-value between 0.6 and 1.0 and were distributed widely across the basin. There were only few stations with r-values between 0.4 and 0.6 in the areas of Cambodia and no stations with r-values between 0.0 and 0.4. CHIRPS had the highest correlation in the northern and central areas and the Vietnam delta and the least correlation in the southwestern regions of Cambodia. With significantly less r-values, the TMPA analysis showed more of a spatial pattern of correlation than the CHIRPS spatial analysis (Figure 7). Stations with r-values between 0.8 and 1.0 were mostly collected in the central region of the basin in Eastern Thailand and Vietnam and represented the highest correlation between TMPA and in-situ measurements. Overall, CHIRPS had higher r-values than TMPA for the monthly rainfall spatial comparison, which indicated that CHIRPS might be able to better spatially represent precipitation in the LMRB.

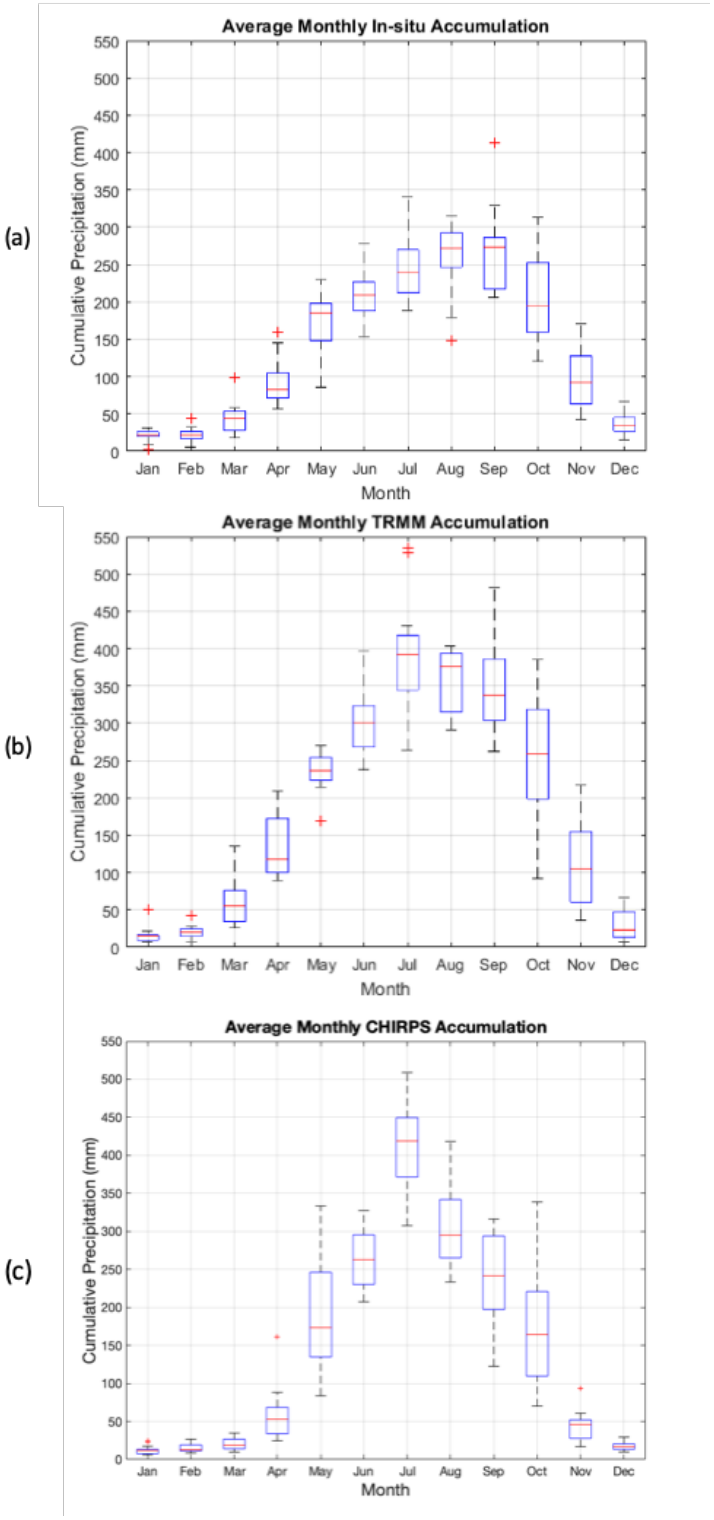

Figure 2.4. (a) Boxplot analysis of each month using rain gauge measurements. (b) Boxplot analysis of each month using TMPA estimates. (c) Boxplot analysis of each month using CHIRPS estimates. Each analysis uses data from 2000 to 2014. Red horizontal bars represent the median rainfall amount. The blue boxes represent the data

that is within the 25th and 75th percentiles. The black horizontal bars above and below the blue boxes represent the maximum and minimum rainfall amounts, respectively. The red '+' represent outliers in the data set.

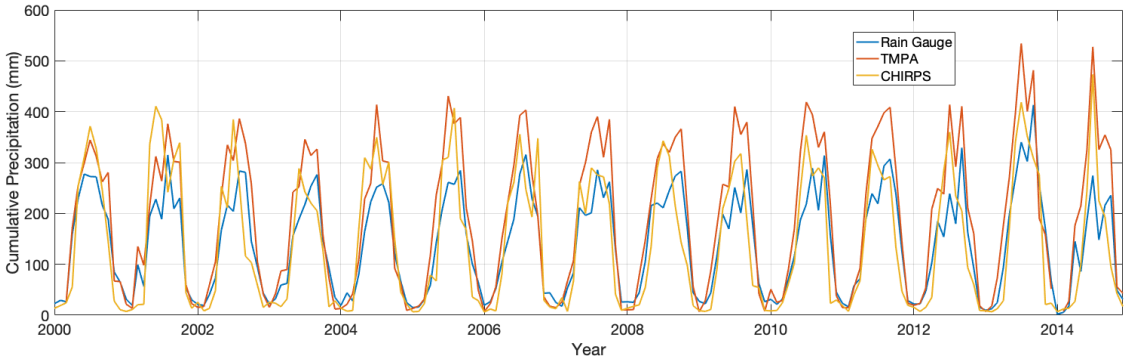

Figure 2.5. Time-series comparison of monthly averages from in-situ data and TMPA and CHIRPS satellite-based precipitation estimates from 2000 to 2014.

Table 2.3. Comparison statistic results between rain gauge measurements and satellite-based precipitation estimates for monthly rainfall categorized on the basis of elevation for R, bias, MAE, and RMSE.

Rain Gauge Elevation	Satellite-Based Product	R-value	Bias (mm)	MAE (mm)	RMSE (mm)
0 – 100 m	CHIRPS	0.79	-36.91	56.71	85.41
	TMPA	0.54	15.52	66.36	107.11
101 – 300 m	CHIRPS	0.84	-42.82	63.03	101.58
	TMPA	0.69	-33.49	69.50	111.71
301 – 500 m	CHIRPS	0.80	-15.07	59.57	98.56
	TMPA	0.63	-19.79	70.62	119.10
501 – 1000 m	CHIRPS	0.81	-5.41	57.69	95.20
	TMPA	0.59	-8.69	73.25	120.21
>1000 m	CHIRPS	0.81	-22.47	56.99	103.75
	TMPA	0.54	23.35	92.33	152.24

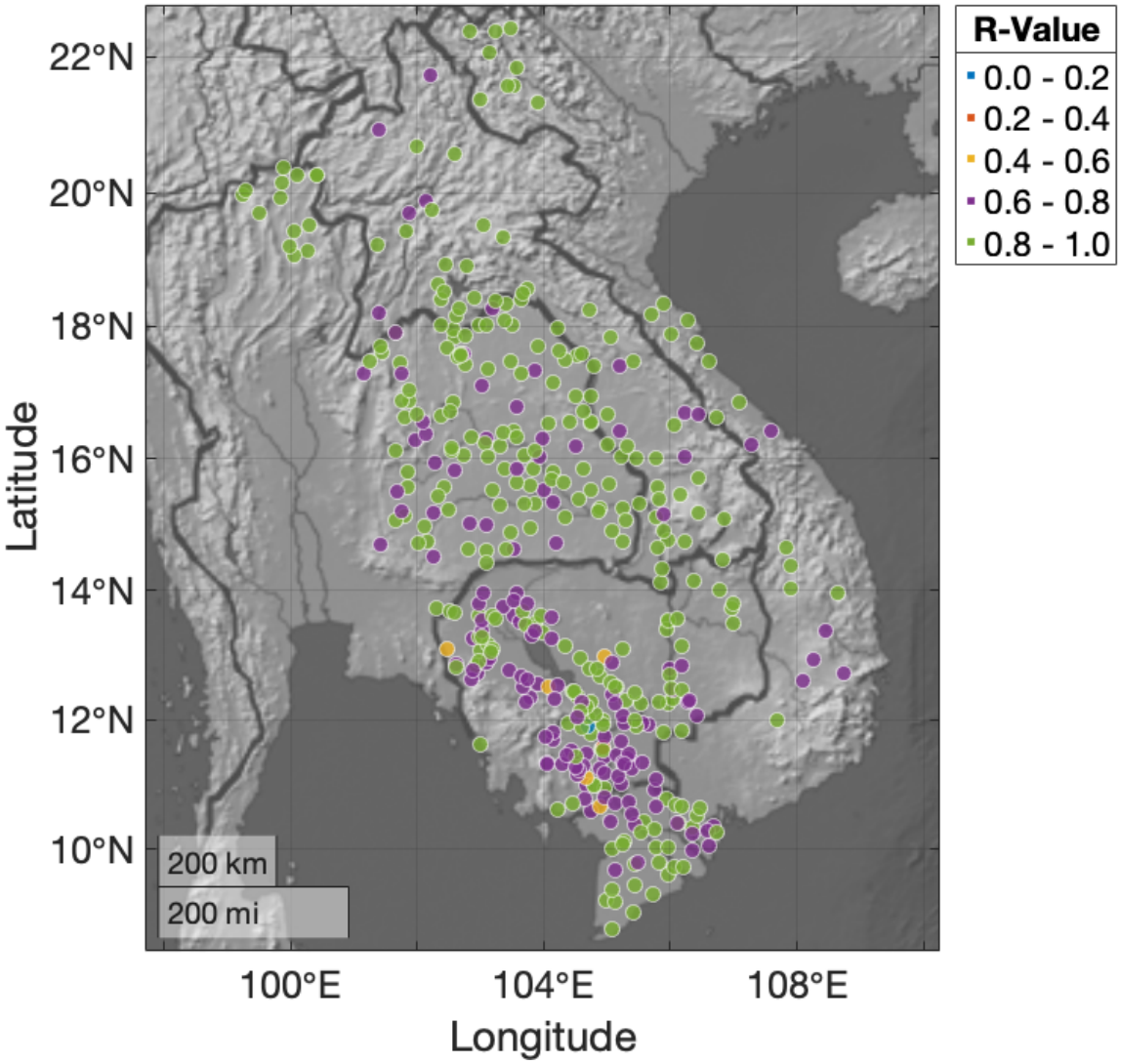

Figure 2.6. Spatial correlation results of mean r-value for each rain gauge stations against CHIRPS precipitation estimates for monthly rainfall.

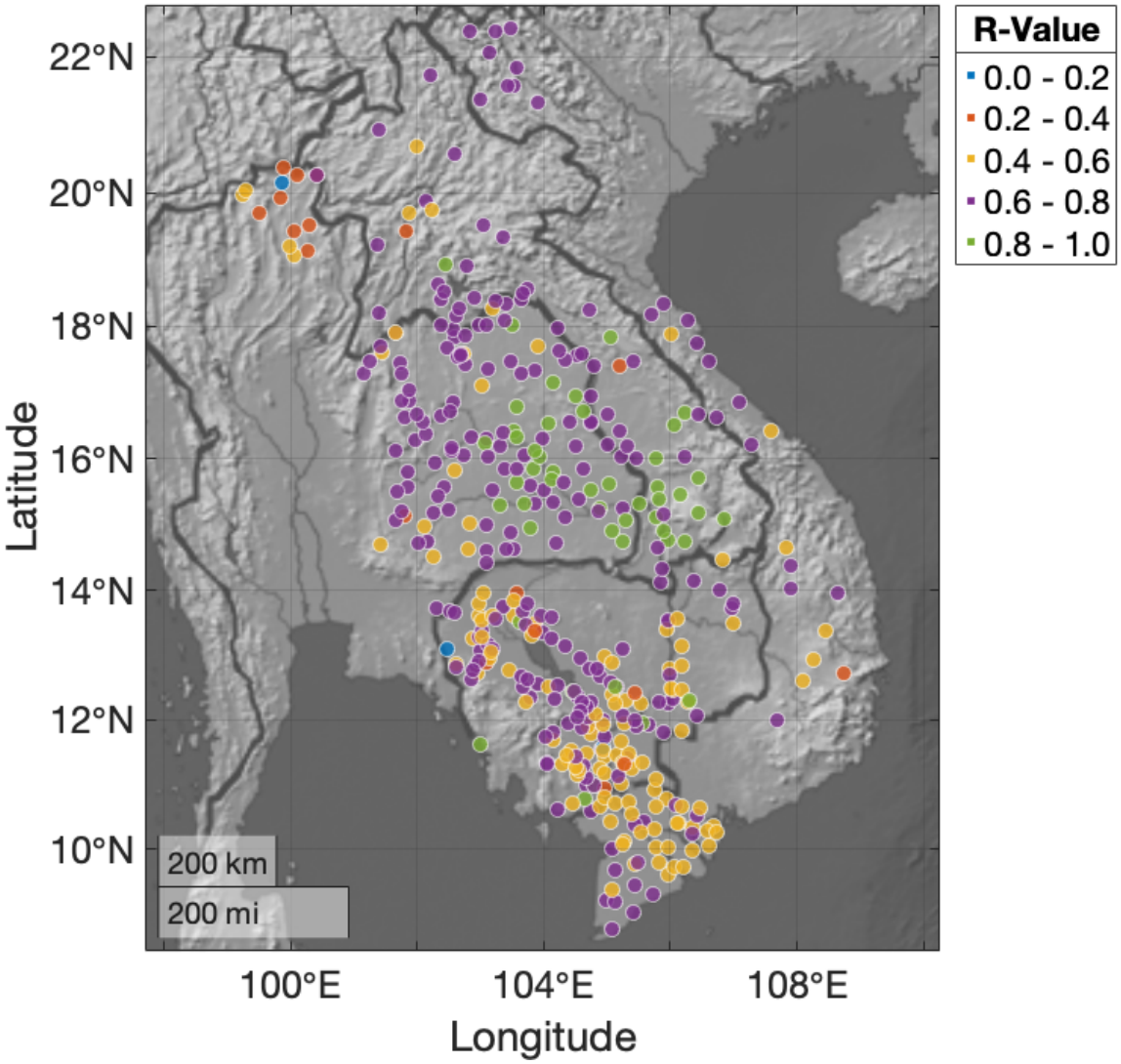

Figure 2.7. Spatial correlation results of mean r-value for each rain gauge stations against TMPA precipitation estimates for monthly rainfall.

2.5. Discussion

This study analyzed the performance of NASA's TMPA satellite-based precipitation estimates (3B42 v.7) and Climate Hazards Group InfraRed Precipitation with Station data (CHIRPS) in the Lower Mekong River Basin using an extensive rain gauge network for validation. A detailed comparison was performed between the satellite-based rainfall products and in-situ measurements from 477 rain gauge stations. A rain–no-rain detection analysis showed that TMPA made a correct detection of a wet or dry day 64.99% of total days and CHIRPS made a correct detection of a wet or dry day 66.8% of total days, when compared to all in-situ daily

measurements. With this validation study, we conclude that CHIRPS was better able to distinguish wet and dry days than TMPA. Satellite-based rainfall estimates were compared monthly, seasonally, and annually to in-situ data for the time period from 2000 to 2014. Additionally, rain gauges were categorized on the basis of elevation and mean rainfall accumulation and were compared to the corresponding TMPA and CHIRPS pixels to determine the effects of topography and amount of rainfall on satellite-based product estimation. When averaged over the entire LMRB, the satellite-based data mostly retained the overall annual precipitation patterns and geographic distributions. Overall, TMPA overestimated in-situ rainfall in the dry seasons, whereas CHIRPS underestimated rainfall in the dry seasons. Furthermore, both satellite-based estimates were more highly correlated to in-situ data during the wet season (June–September) than dry season (November–February). Similarly, the annual comparisons between in-situ and both satellite-based estimates showed higher correlations than the monthly comparisons when analyzed over the fifteen-year study period. The bias and false detections in the satellite-based estimates could be caused by topography, rain gauge data availability, or amount of precipitation received in certain locations. The r-values were determined at each station location based on monthly rainfall accumulation from in-situ measurements and both satellite-based products. CHIRPS was more highly correlated to the rain gauge stations across the basin than TMPA, with the majority of stations having r-values of 0.8 to 1.0, when compared to CHIRPS. Additionally, CHIRPS did not show a distinct spatial pattern of correlation, whereas TMPA did show a geographical pattern. The correlation dependence on geography and climate could be explained by TMPA being more affected by the annual monsoon movement. Overall, the spatial comparison showed CHIRPS to have a higher correlation than TMPA with rain gauge measurements in the LMRB, which indicated that CHIRPS might be able to better spatially represent rainfall.

As stated previously, other precipitation comparisons have been implemented and vary by location, number of rain gauges, satellite-based product, and study period. The results of these studies also differ in whether satellite-based estimates overestimated or underestimated in-situ measurements. A study by Katsanos et al. (2004), found a higher bias in the satellite-based estimates during peak precipitation periods, and this study also found high biases during peaks

in the wet season. For example, the results from this comparison were similar to a study by Collischonn et al. (2008) over the Tapajos River Basin in Brazil, in which TMPA estimates were found to be very close to the in-situ measurements when averaged over the entire river basin and that TMPA mostly underestimated precipitation in their study. Additionally, a study by Su et al. (2008) over the La Plata Basin in South America found TMPA to be less accurate during high rain rates at a daily time scale and to overestimate rainfall, which was similar to the results of this study during the wet season that was represented by high rain rates. In their study, TMPA was able to represent low flows but had a positive bias during peak flows in satellite-driven model simulations. In order to use TMPA in the LMRB for similar satellite-driven watershed modeling, such biases would need to be accounted for and adjusted to more accurately estimate streamflow and capture flooding events. After comparing TMPA and CHIRPS to rain gauge measurements, the results of this research showed that CHIRPS might be better at representing precipitation in the LMRB than TMPA. However, Xian et al. (2018) found TMPA to be superior to CHIRPS in hydrological simulation using SWAT. Furthermore, spatial resolution did play a role in the validation of these precipitation products. CHIRPS had a spatial resolution of 0.05° and TMPA had a resolution of 0.25°. Generally, higher spatial resolution translates to higher accuracy, but this was dependent on the method used to generate this product. What we imply is an inferior method used to generate a high spatial resolution product that might have a lower accuracy than a superior method used to generate a lower spatial resolution product. In this study we find that the accuracy of TMPA and CHIRPS were very close, but the higher spatial resolution of CHIRPS might provide an advantage in the accuracy when compared to rain gauges.

2.6. Conclusions

This work was one of the first attempts at evaluating the satellite-based precipitation data products in the Lower Mekong River Basin with such an extensive in-situ dataset. The hydrologic significance of TMPA and CHIRPS in the LMRB could be assessed from the results of this study and other analogous validation studies. In addition, a similar methodology to the one described here could be applied to the GPM IMERG data to further assess the performance of satellite-based precipitation products in the region. The important broad impacts of this research are the

implications of remotely sensed products in hydrologic cycle modeling, specifically in the LMRB or similar un-gauged basins. For future validation studies of satellite-based estimates, this methodology could be applied to new, higher resolution products like GPM IMERG, to look at the progression and advancement in satellite-based estimation. With better temporal and spatial coverage, satellite-based inputs will serve as an improvement, compared to precipitation from rain gauges for various modeling in basins like LMRB where there is a sparse coverage of rain gauges. Additionally, evaluation of satellite-based products is essential for improvement upon satellite-based algorithms and equipment. Given the observed increase in accuracy of remotely sensed precipitation products (sensor configurations, improved spatial resolution, and temporal repeat), a careful comparison of the fidelity of each product, as shown here, is helpful for assessing their utility for basin-scale modeling capabilities, particularly for water resource management applications in poorly-gauged basins such as LMRB. This study undertook a unique approach at comparing TMPA and CHIRPS estimates with in-situ observations in the LMRB. We conclude that precipitation from TMPA and CHIRPS could be used reliably in hydrological applications in rain gauge sparse regions of the world.

3. Chapter 3. The Influence of Land Use and Land Cover Change on Landslide Susceptibility in the Lower Mekong River Basin

Associated citations:
(1) Dandridge, C.; Stanley, T.A.; Kirschbaum, D.B.; Lakshmi, V. The influence of land use and land cover change on landslide susceptibility in the Lower Mekong River Basin. Natural Hazards 2022, 115, 1499–1523, https://doi.org/10.1007/s11069-022-05604-4
(2) Dandridge, C.; Stanley, T.A.; Kirschbaum, D.B.; Lakshmi, V. The Influence of Land Use and Land Cover Change on Landslide Susceptibility in the Lower Mekong River Basin, H030-0023 presented at 2020 Fall Meeting, AGU, December 1-17.

3.1. Introduction

A landslide encompasses a wide range of mass movements and can be defined as the downslope movement of soil, rock, or earth (Highland & Bobrowsky, 2008). The movements can be triggered by various external activities such as intense rainfall, earthquakes, changes in water level, waves, or stream erosion, which lead to a decrease in shear strength and an increase in shear stress on the slope (Dai et al., 2002). Landslides can also be caused by anthropogenic activities such as excavation, road construction, and land use changes. These factors often induce small, shallow landslides, but abrupt changes to the slope surface such as poor construction and planning can result in larger, more dangerous landslides (Jaboyedoff et al., 2016). Watersheds that have been recently affected by wildfires can be highly susceptible to rainfall-triggered landslides that usually occur within a short time following the burn (Degraff et al., 2015; Kean et al., 2011). This study focuses on rainfall-triggered landslides as they are the most frequent and cause loss of life and destruction of property across the globe (Froude & Petley, 2018). Rapid urbanization can increase the risk for landslides, especially along poorly constructed roads and deforested areas in mountainous regions (Forbes et al,. 2012). However, better land management of forests and cultivated areas can produce a decrease in rainfall-triggered landslide occurrence (Pisano et al., 2017).

In the Lower Mekong River Basin (LMRB) in Southeast Asia, the monsoon season brings an increase in flood and landslide disasters due to an increase in rainfall from large storms in combination with the complex topography of the region. The LMRB has

experienced extensive changes from urban and agricultural expansion, deforestation, river damming, and natural disasters such as flood and drought. In this region, changes in Land Use and Land Cover (LULC) are largely influenced by agricultural prices, road accessibility, construction projects, and climate change. Spruce et al. (2020) assessed LULC changes in the Lower Mekong using two maps from 1997 to 2010. In their analysis, 2.5% of the total area of permanent agriculture decreased which could be associated with the abandonment of crops or converting cropland to forests. They also identified an 6.7% increase of the total area categorized by scrub/shrub/herbaceous which could be attributed to abandoned cropland reverting back to forest. Looking at the changes between LULC classes, some cropland had changed to deciduous forest/scrub over time between 1997 and 2010. Changes in land cover can have variable impacts on landslide susceptibility. In some cases, human impacts such as deforestation and mining serve to exacerbate instability on slopes (Winter et al., 2010). In other examples, thoughtful engineering and planning can serve to stabilize slopes (Prastica et al., 2019).

The preconditions for landslides vary, but changes in land use and land cover (LULC) have been shown to have local impacts (e.g., Glade 2003; Hewawasam 2010; Mugagga et al. 2012; Reichenbach et al. 2014). Pisano et al. (2017) evaluated how land cover change affects slope stability over time in the Italian Southern Apennine Mountains by treating land cover as a dynamic variable, unlike many other landslides susceptibility studies that consider land cover as a static variable. This study found that a decrease in forest and cultivated land and increase in barren, pasture, and shrub land led to an increase in landslide susceptibility. A study by Persichillo et al. (2017) assessed shallow landslides in the northern Apennine Mountains in Italy in areas with land abandonment and changes in land management practices from 1954 to 2012. They found that cultivated lands that were abandoned and allowed to gradually recover naturally was the land cover change scenario most susceptible to landslides and land cover was the most predisposing factor in all study areas. Similarly, Deng et al. (2018) investigated landslide distribution and agricultural abandonment in several provinces in China's mountainous areas. They concluded that more landslides occurred in areas with high incidence of agricultural abandonment. Furthermore, the effects

of land use changes on landslides were analyzed in a landslide-prone region in Northeast Turkey with mountainous topography and high rainfall frequency by Karsli et al. (2009). Land cover changes and landslides were identified using aerial images taken in 1973 and 2002. Their results indicated that the land cover type played an important role in landslide occurrence as 95% of the landslides identified from the imagery were in areas with acidic soil weakened by fertilizer use in agriculture.

The effects of LULC on landslide susceptibility vary based on geographical location of the study area and methodology used for analysis. Remondo et al. (2003) applied various validation techniques for landslide susceptibility maps in the Deba Valley in northern Spain and state that while intense rainfall is the main triggering mechanism for shallow landslides, human activity affecting land cover changes are also influential as these alterations increase the sensitivity of the area to intense precipitation. Kafy et al. (2017) evaluated the association between LULC changes and landslides in the Chittagong Hill Tracts region, Bangladesh using a change detection technique to obtain the change over two decadal time periods from 1995 to 2005 and 2005 to 2015. They classified LULC as baresoil, hill forest, built-up area, and waterbody and found a positive relationship between landslide occurrence and decreasing hill forest. A study by Hewawasam (2010) investigated landslides in the Upper Mahaweli Catchment, Sri Lanka and stated that human activities were the primary cause of the increased landslide activity in the area, many of which occurred in agricultural areas on hillslopes. After the decline of the coffee industry in this region, many coffee lands that were deforested were restored as tea plantations, and out of 200 landslides the largest percentage, 35%, of landslides evaluated in their study occurred in LULC areas classified as tea plantation. Landslide occurrence in response to LULC change in New Zealand was assessed by Glade (2003), who found that forest clearance led to increased rates of landslides by evaluating sedimentation rates following land use modifications that triggered landslide activity. Lee and Sambath (2006) mapped landslide susceptibility in the Damrei Romel area in Cambodia and found higher landslide activity in areas with LULC classified as forest and shrubland than agriculture and grasslands due to landslides occurring in mountainous areas with steep slopes. Furthermore, Liu et al. (2021) examined changes in landslide susceptibility due to

LULC changes in Lixian County, China and also found that landslide-prone areas were attributed to LULC classifications of rainfed cropland and rural land, and forested areas had low landslide susceptibility. The results of these studies show that LULC is an important influencing landslide activity, but the relationship varies between studies.

Frequency Ratio (FR) analysis is a common method used to assess the relationship between susceptibility and the occurrence of a landslide event (Gariano et al., 2018, Pourghasemi et al., 2013). A study by Silalahi et al. (2019) used GIS mapping and FR analysis to assess the effects of contributing factors on landslides in Bogor, Indonesia. Their results indicated land cover as one of the most important factors contributing to landslides as well as lithology and soil type in this area. Additionally, Khan et al. (2019) used the FR to create a landslide susceptibility index which was used to produce a susceptibility map for northern Pakistan. Their study found barren land and irrigated agricultural land to have the highest FR values of the land cover classifications, however distance to roads was found to have the highest overall FR value. These and other studies use FR to assess conditioning factors and create susceptibility maps but however, rarely incorporate land cover as a dynamic variable. Additionally, statistical methods like Logistic Regression (LR) are effective in identifying input variable importance/significance and several studies have considered LULC within this framework (Reichenbach et al., 2018; Lee & Sambath, 2006; Das & Lepcha, 2019). LR has been an effective tool for developing landslide susceptibility maps and highlighting the significance of contributing variables however, few studies have considered how LULC can be considered dynamically in these models to explain changes over time in a region. Hemasinghe et al. (2018) analyzed susceptibility in mountainous regions predisposed to landslides in Sri Lanka. Their study examined slope, aspect, lithology, land cover, distance to rivers and roads as predictor variables. Land cover was determined to be the most influential factor in the study area. Known landslide locations were used to validate their susceptibility map, and a majority (76%) of the landslide points were in high and extremely high susceptibility areas. Land cover is similarly used as a static predictor variable in many other susceptibility studies, uniquely this study will treat land cover change as a dynamic variable that changes over time.

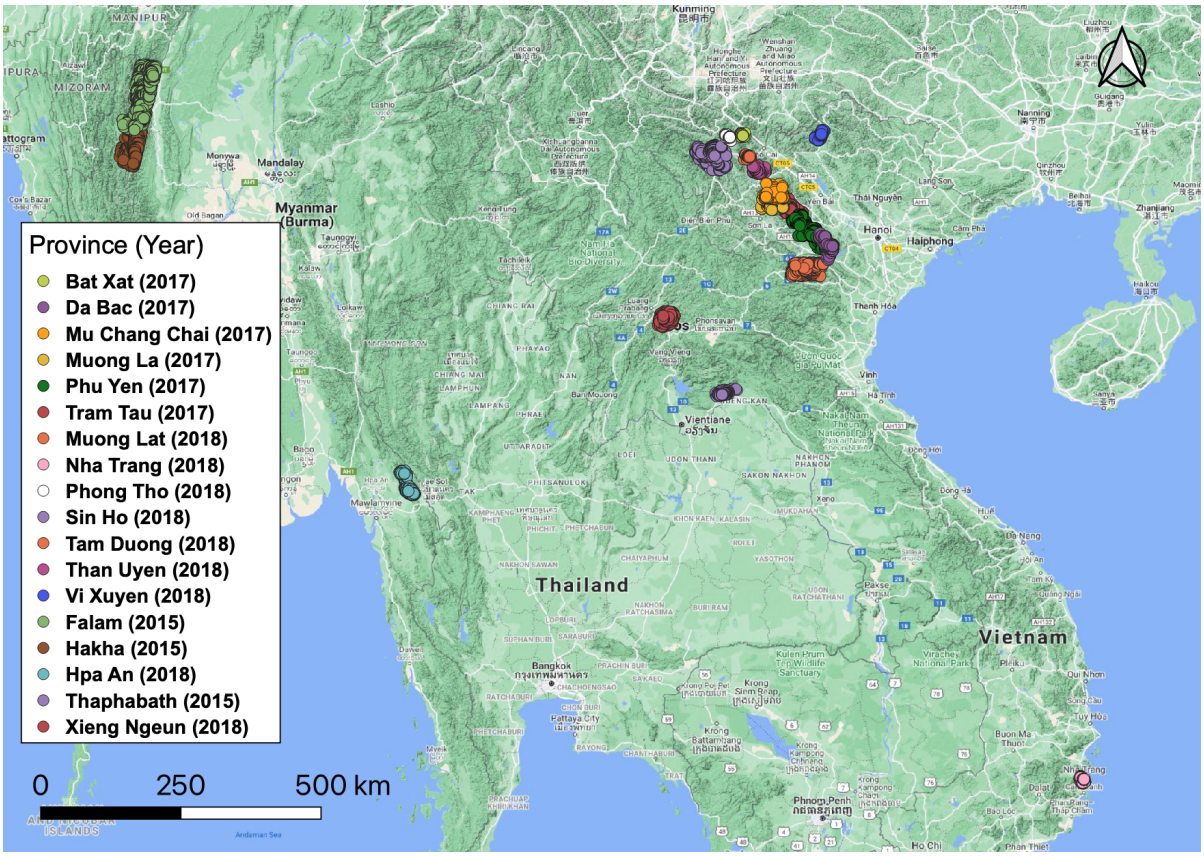

Figure 3.3.1. Geographic locations of the landslide inventories in the LMRB

The question posed in this study is - how do changes in land use and land cover (LULC) impact landslide susceptibility in the LMRB? We evaluate these interactions using several new landslide event inventories mapped between 2015 – 2018 that provide information within areas of Vietnam, Myanmar, and Laos (Amatya et al., 2021) (Figure 3.1.). Additionally, this study closely examines the effects of LULC change on landslide occurrence, a dynamic which is not completely understood in the LMRB. Our work seeks to understand the relationship of changing LULC over time and how this impacts susceptibility. The relationship between LULC changes and landslide occurrence will be analyzed using Frequency Ratio (FR) analysis and Logistic Regression (LR) modeling. The FR will be used to closely examine the frequency of landslides within the various LULC change scenarios present in each of the landslide inventory locations. This study will use the LR models to compare LULC changes with other contributing factors like slope, forest loss, soil properties described in Table 3.2. The FR and LR results will be compared to determine any similarities regarding the significance of LULC changes on landslide

occurrence. Results of this work are important as population expansion, road development and farming continue to increase (and hence changes in land cover) in the LMRB (Spruce et al., 2018). This work is part of a broader effort to characterize landslide susceptibility, hazard, and exposure within the LMRB for decision making at the country and municipal level using satellite remote sensing products.

3.2. Data

3.2.1. Landslide Inventory

The landslide inventories used in this research were mapped utilizing high-resolution satellite imagery from Planet using the modified framework of Semi-Automatic Landslide Detection (SALaD) system (Amatya et al., 2021). SALaD uses object-based image analysis and machine learning to map landslides. As we are focusing on rainfall event-based inventories, it is important we map landslides induced by that event only as pre-event landslides may have been triggered by phenomena such as earthquakes. A change detection-based approach was introduced to the SALaD framework (SALaD-CD) utilizing pre- and post-event imagery (Amatya et al., 2021). The new framework incorporates image normalization, image co-registration and change detection. The landslide polygons produced by SALaD-CD were manually corrected and converted to initiation points using NASADEM (NASA JPL, 2020). A total of 18 rainfall-triggered landslide inventories between 2015 and 2018 were used in this analysis: 13 in Vietnam, three in Myanmar, and two in Laos (Figure 3.1.). Details on the landslide inventories used in this study are provided in Table 3.1.

Table 3.1. Data descriptions, resolutions, and sources

Dataset	Derived variables	Spatial resolution	Source
DEM [raster]	Slope Aspect	30 m	NASA JPL (2020)
Land cover [raster]	Land use/land cover change (LULC)	30 m	Saah et al., (2020)
Roads [vector]	Distance to roads	—	Meijer et al., (2018)
Soil properties [raster]	Bulk density Organic carbon	250 m	Hengl et al., (2017)

Forest Cover [raster]	Forest cover loss	30 m	Hansen et al., (2013)

3.2.2. Digital Elevation Model (DEM)

NASADEM with 30 m spatial resolution was used to derive the input variables for slope and aspect [38]. NASA DEM is derived from SRTM, which was launched in 2000, with processing improvements, elevation control, void-filling and merging with data that was unavailable at the time of the mission. NASADEM also provides an improved spatial resolution from the original three-arcsecond SRTM DEM to one-arcsecond, making it the finest resolution, global, freely-available DEM product. Slope is one of the major influencers of landslide activity, and therefore was selected based on its likely correlation with landslide susceptibility (Indhanu et al., 2020). The aspect is derived using GIS and reclassified to represent North, South, East, and West facing slopes. Data is publicly available from https://doi.org/10.5067/MEaSUREs/NASADEM/NASADEM_HGT.001.

Table 3.2. Landslide inventory description

District	**Country**	**Year**	**Satellite**	**Landslides**	**Area [km²]**	**Landslide Area [km²]**
(BX) Bat Xat	Vietnam	2017	PlanetScope	99	255.96	0.26
(DB) Da Bac	Vietnam	2017	RapidEye	1086	1198.44	3.65
(MC) Mu Chang Chai	Vietnam	2017	RapidEye	1256	873.06	1.35
(ML) Muong La	Vietnam	2017	RapidEye	758	1002.56	1.14
(PY) Phu Yen	Vietnam	2017	RapidEye	1368	2500.00	5.47
(TT) Tram Tau	Vietnam	2017	RapidEye	1490	625.00	2.93
(MT) Muong Lat	Vietnam	2018	PlanetScope	1718	1354.85	5.47
(NT) Nha Trang	Vietnam	2018	PlanetScope	207	149.31	0.5
(PT) Phong Tho	Vietnam	2018	PlanetScope	302	150.01	0.58
(SH) Sin Ho	Vietnam	2018	RapidEye	707	3125.00	2.04
(TD) Tam Duong	Vietnam	2018	PlanetScope	159	188.02	0.75
(TU) Than Uyen	Vietnam	2018	PlanetScope	312	416.26	0.74
(VX) Vi Xuyen	Vietnam	2018	PlanetScope	157	333.34	0.17
(FM) Falam	Myanmar	2015	RapidEye	5086	3956.96	57.63
(HK) Hakha	Myanmar	2015	RapidEye	1737	2211.00	17.54
(HA) Hpa-An	Myanmar	2018	PlanetScope	992	679.59	2.07

(TB) Thaphabath	Laos	2015	RapidEye	242	1250.00	0.97
(XN) Xieng Ngeun	Laos	2018	PlanetScope	1178	831.86	2.58

3.2.3. Land Use/ Land Cover (LULC)

Land use and land cover (LULC) data from the Regional Land Cover Monitoring System (RLCMS) is available via the SERVIR-Mekong Land Use Portal and is presented at 30 m spatial resolution and yearly temporal resolution from 1987 to 2018 for the Lower Mekong River Basin (Saah et al., 2020). The RLCMS uses historical Landsat and MODIS data to create LULC maps. The methodology behind deriving the maps can be summarized, defining the classification typologies, creating the primitive layers using supervised classification and machine learning algorithms, combining the primitive layers into land cover maps, and lastly, an accuracy assessment. The typology classifications were determined by stakeholders from Cambodia, Laos PDR, Myanmar, Thailand, and Vietnam. LULC data from ten years prior to each landslide event, spanning from 2005 to 2018, were used for analysis in this study. Due to limited spatial representation of the original classifications, the land cover was reclassified into three categories shown in Table 3.3., similarly to the methodology in Chen et al. (2019). For more information on how this dataset was created and its details, please review Saah et al. (2020). Data is publicly available from https://landcovermapping.org.

Table 3.3. Reclassification of land cover categories

New classification	Original classification
Urban	Urban and built up
	Mining
	Aquaculture
Agriculture	Cropland
	Grassland
	Shrubland
Forest	Forest
	Evergreen Broadleaf
	Mixed Forest
	Orchard or Plantation Forest

3.2.4. Roads

Proximity to roads has been found influential on rainfall-triggered landslide occurrence in several areas in previous studies (Larsen & Parks, 1997; Penna et al., 2014; McAdoo et al., 2018). The construction of roads changes the hydrologic response and surface and subsurface flow paths in the affected area which can influence landslide susceptibility. McAdoo et al., (2018) found that within 100m of a road rainfall-triggered landslides were more than two times as likely to occur in Nepal. The Global Roads Inventory Project (GRIP) is compiled from publicly available national vector datasets from governments, research institutes, NGOs and crowd-sourcing initiatives and includes over 21 million km of roads. The GRIP dataset is available as a vector dataset for each region of the world. The Southeast Asia GRIP dataset was used to derive a distance to roads raster which represents the distance to nearby roads for each pixel in the selected extent using GIS software for each landslide inventory location. For more information on how this dataset was created and its details, please refer to Meijer et al. (2018). Data is publicly available from https://www.globio.info/download-grip-dataset.

3.2.5. Soil Properties

The World Soil Information Service (WoSIS) provides standardized soil profile data for various environmental applications at global scale. The most current WoSIS snapshot is a compilation of nearly 200,000 soil profiles from locations across the globe. These profiles are standardized and distributed using a database model, SoilGrids, which uses machine learning methods to map the spatial distribution of soil properties based on the soil profile observations (Hengl et al., 2017). Soil data is available for six standard depth intervals at 250 m spatial resolution. For a full description of this data, please refer to Batjes et al. (2020). Two soil layers representing bulk density and organic carbon were downloaded from SoilGrids for each study region at the at 0 – 5 cm depth. These variables were resampled to the resolution of the DEM at 30 m for model implementation. Data is publicly available from www.soilgrids.org.

3.2.6. Forest Cover Loss

Global Forest Change data is created from Landsat imagery at 30 m spatial resolution and characterizes forest extent, loss, and gain and is available from 2000 to 2019. In this study, this data is used to estimate the Forest Loss over the past ten years for each landslide inventory extent. For more information on the methodology and details of this dataset, please review Hansen et al. (2013). Data is publicly available from http://earthenginepartners.appspot.com/science-2013-global-forest.

3.3. Methodology

3.3.1. LULC Analysis

The landcover maps were reclassified from nine categories to three broader categories due to the limited spatial representation of the original land cover classifications in the small extents represented by the landslide inventory locations. These reclassification categories as well as the original categories represented in the study area described in Table 3.3. and shown in Figure 3.2. for the greater Lower Mekong region. The reclassified landcover maps were analyzed to estimate the amount and type of change over the 10-year time period prior to the landslide event in each study region as well as the overall LULC patterns in the greater Lower Mekong region from 1998 to 2018. Overall, the time frame used to analyze LULC changes varies in the literature. Several studies chose time intervals that ranged from five to 30 years due to the availability of aerial imagery (Persichillo et al., 2017; Deng et al., 2018; Karsli et al., 2009). The 10-year time period was selected based on previous studies that assessed LULC changes over time. Chen and Huang (2013) compared LULC changes over 10 years (1999 to 2009) to determine the relationship between LULC change and landslides triggered by Typhoon Morakot in Taiwan. They found that areas with a change in land cover had a higher frequency of landslides than non-changed areas. Here, the LULC change over the ten-year time-period was estimated by assigning a change scenario to each pixel based on its land cover classification in the two maps (i.e., map of landcover in 2018 compared to the map of landcover in 2008). There is a total of nine possible LULC scenarios for each pixel including three no-change scenarios where the type of land cover classification did not change.

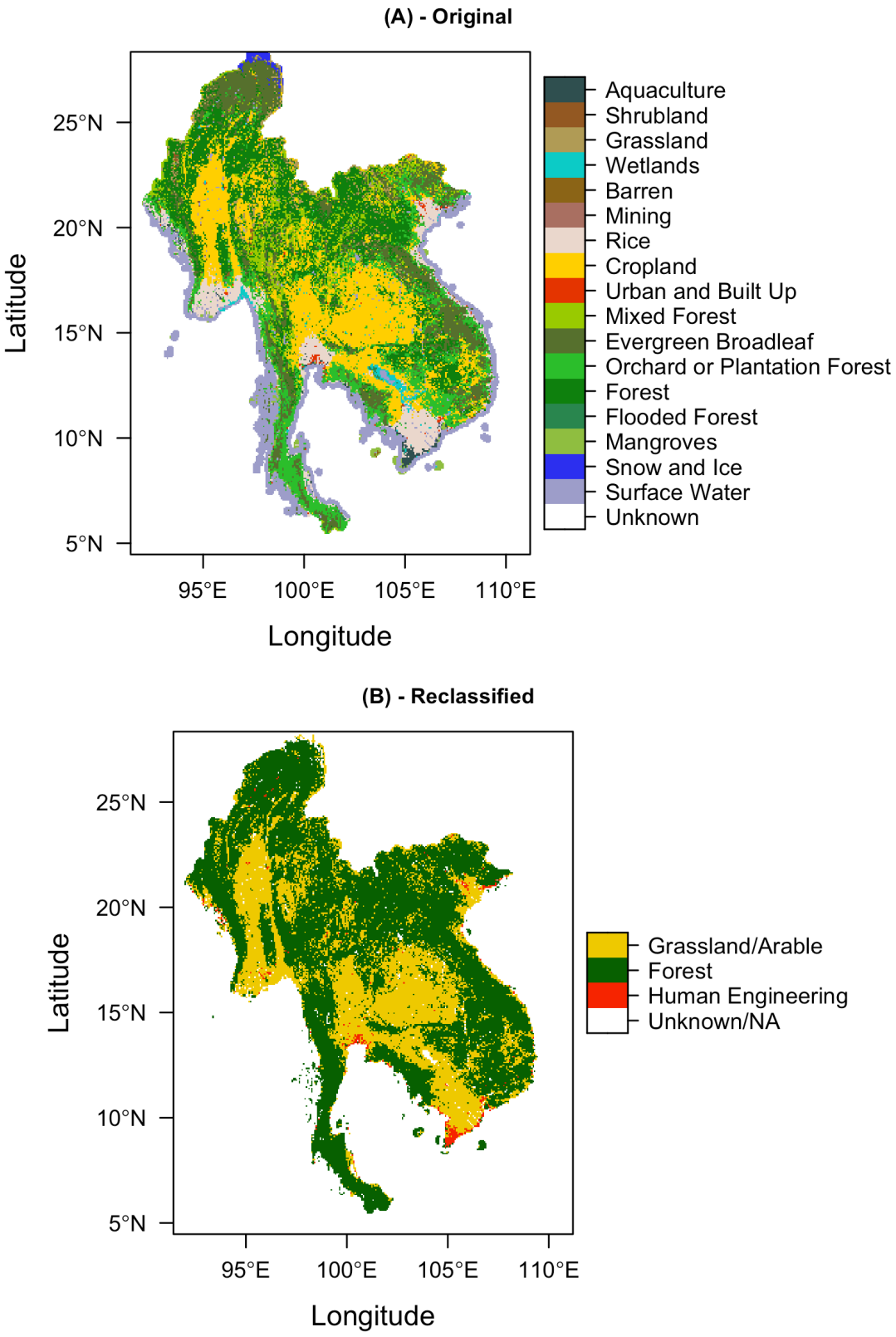

Figure 3.2. (A) The original LULC classifications and (B) the reclassified LULC classifications for the LMRB region in 2018.

over the specified time-period. The percentage of total area of each LULC scenario is estimated and reported for each landslide inventory location and shown in Figure 3.3. (A) and averaged over all locations in Figure 3.3. (B). Land cover classified as urban represents less than 1% in each study area except for one inventory, Nha Trang (NH), which is composed of 16% urban area. Only three of the inventories are characterized by greater than 25% agricultural area (Figure 3.3.A). Forests comprise over 50% of each area and 81% of the total area used for analysis. The LULC change scenario with the largest area represented in the study locations is from agriculture to forest, representing 2% of the total area and less than 5% in each inventory extent (Figure 3B).

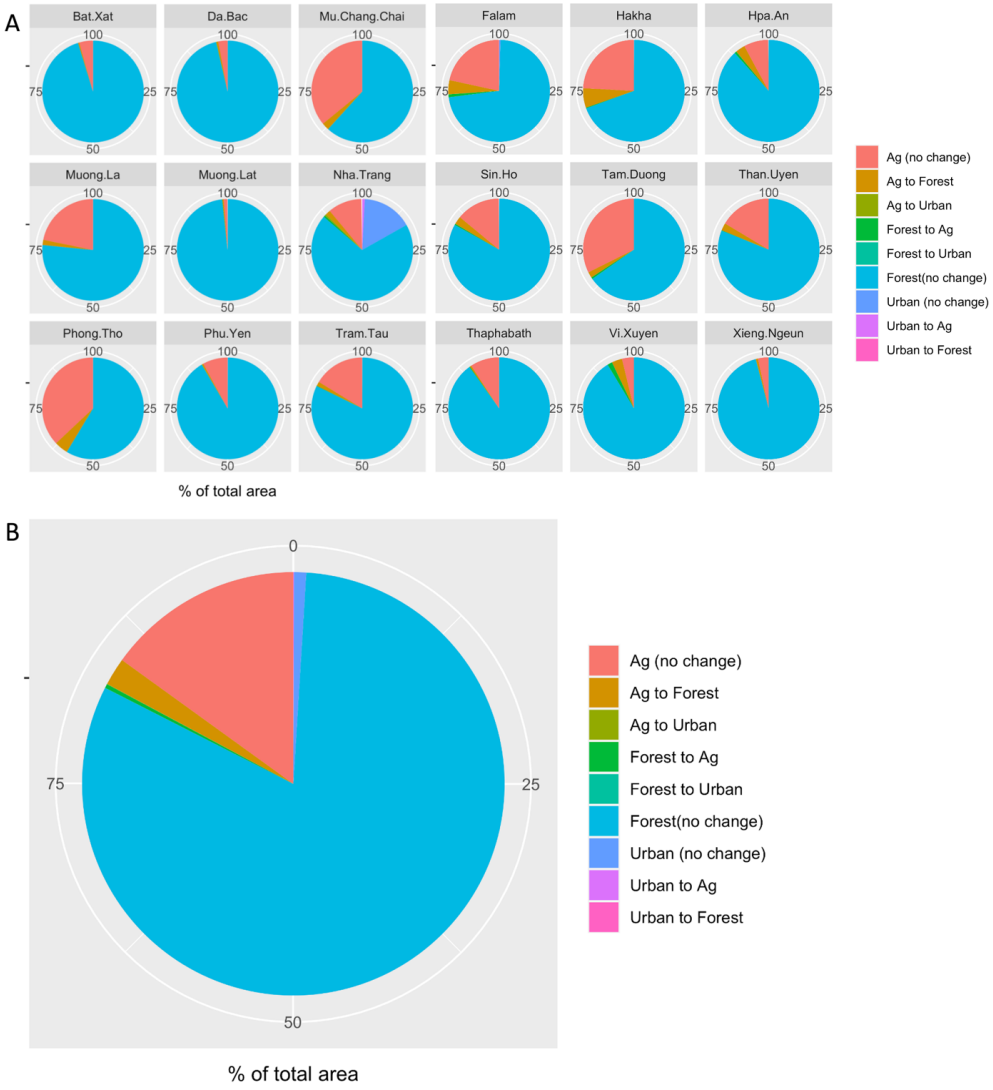

Figure 3.3. (A) Percentage of area for each LULC change scenario over 10 years for each inventory location (B) Percentage of area of each LULC change scenario averaged over all locations.

3.3.2. Frequency Ratio Analysis

Frequency ratio (FR) was used in this study to quantitatively examine the relationship between landslide occurrence and each LULC change scenario. The FR is the ratio of the percentage of landslide occurrence in a factor class to the total percentage of that factor in the area, and the average FR value is one (Khan et al., 2019). Values greater than one indicate that landslides occur more frequently relative to the total distribution within the variable being considered over the study area. FR values lower than one indicate a lower amount of landslide occurrence (Gariano et al., 2018). The equation used to calculate FR is as follows:

$$FR = \frac{M_i / \sum M_i}{N_i / \sum N_i} \qquad (1)$$

Where M_i = number of pixels containing landslides in LULC class i, $\sum M_i$ = total number of pixels containing landslides in the study area, N_i = total number of pixels in the study area for that particular LULC class, and $\sum N_i$ = total number of pixels in the study area. The FR of each LULC scenario is estimated for each study location.

3.3.3. Logistic Regression

A logistic regression model is used in this study to further assess the relationship between changes in LULC and landslide occurrence as well as determine any similarities with the results of the Frequency Ratio analysis. The model is outlined in the workflow diagram shown in Figure 3.4. Many susceptibility studies use logistic regression to evaluate binary response variables such as landslide occurrence (Pourghasemi et al. 2013; Lombardo & Mai, 2018; Horafas & Gkeki, 2017). Logistic regression models the probability of events based on the linear combination of independent contributing variables. The model produces coefficients for each input variable, which are used to predict the probability of landslides over the study area. Positive coefficients indicate that there is positive correlation with the presence of this conditioning factor and landslide occurrence, and negative coefficients

indicate a negative correlation between presence of the factor and landslide occurrence and there is an absence of this factor in locations where landslides occur. The predictions are used with raster data of each contributing variable to create a landslide susceptibility map. The equations used in logistic regression are as follows:

$$P = \frac{1}{1 + e^{-Z}} \qquad (2)$$

$$Z = b_0 + b_1 x_1 + b_2 x_2 + \cdots + b_n x_n \qquad (3)$$

Where P = probability of occurrence of the event occurring, Z = linear combination, b_0 = intercept, b_i = slope coefficients, and x_i = independent variables (Lee & Sambath, 2006). To create training and testing datasets, an equal number of non-landslide points are generated. The logistic regression model is used to create landslide susceptibility maps for each of the 18 study regions mapped in the landslide event inventory. The model is trained with 70% of the landslide inventory as well as randomly generated points that do not coincide with landslide locations. The following predictor variables are tested in the logistic regression model in this study: slope, aspect, LULC change, distance to roads, bulk density, organic carbon, and forest loss. These variables were selected based on their spatial and temporal availability and potential correlation with landslide occurrence as well as their significance in the logistic regression models determined by their corresponding p-values. A significance level of 0.01 implies there is less than 0.1 % chance that the coefficient may be equal to zero and therefore be insignificant in determining landslide susceptibility. A p-value less than 0.05 is statistically significant and p-values greater than 0.05 are determined as not statistically significant. All of the model input variables were reclassified into categorical factors for simplified comparison between the categories. The classifications of each factor are shown in Table 3.4. These maps were validated using the Receiver Operating Characteristic (ROC) curve and Area Under the ROC Curve (AUC) analyses, common statistics for assessing the predictive capacity of susceptibility models (Felicísimo et al., 2013). The ROC was derived using a testing dataset that is comprised of 30% of the landslide inventory as well as randomly generated non-landslide points. These metrics are often

considered to evaluate the performance of susceptibility models and the model with a larger AUC value is considered better predictive model (Gorsevski et al., 2006; Zhou et al., 2018).

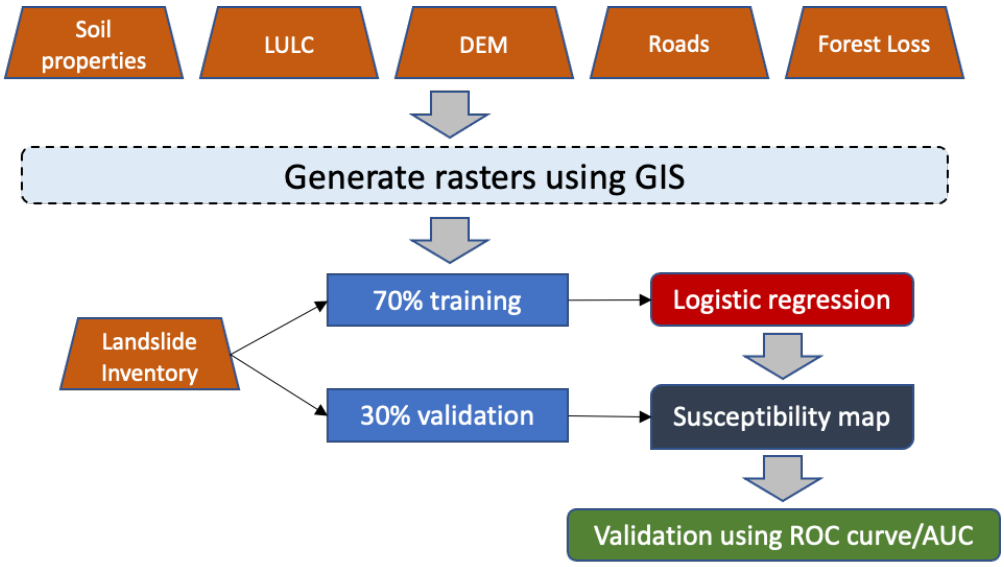

Figure 3.4. Workflow diagram for logistic regression modelling of landslide susceptibility

3.4. Results

Eighteen landslide inventories were used in this study to assess the relationship between land cover change and landslide occurrence. The percentage of total area represented by each LULC scenario averaged over all inventory locations is shown in Table 3.5. The number of total landslides occurring in each LULC scenario from the 18 inventories are shown in Table 3.6. The Frequency Ratio value averaged over all inventories for each LULC scenario is shown in Table 3.7. The category forest with no change in LULC over ten years prior to the landslide event made up about 82% of the total area when averaging over all 18 inventory locations (Table 3.5.). The majority of landslides (15,568) also occurred within this LULC category (Table 3.6.). The average FR for Forest with no change was 2.06 (Table 3.7.). The category making up the second largest percentage of total area is agricultural land with no change over ten years prior to the landslide event, which composed about 15% of the total area (Table 3.5.). This LULC category experienced 2,530 landslides (Table 3.6.) and had an average FR of 1.64 when averaged over all locations (Table 3.7.). The category of

urban with no change represented about 1% of the total area within the 18 inventory locations (Table 3.5.) and experienced no landslides. The LULC change scenario from agriculture to forest in the ten years prior to the landslide event comprised only 2.1% of the total area within all inventory locations (Table 3.5.). However, this area experienced 614 landslides (Table 3.6.) and had an average FR of 2.83 (Table 3.7.) for all locations. The results of the FR analysis could indicate that areas experiencing a change from agriculture to forest are more susceptible to landslides than other land cover change scenarios.

Table 3.4. Classification of factors for model input variables

Distance To Roads	**Forest Cover**	**Slope**	**Aspect**	**Land Cover Change**
< 10 m	no loss (0)	0° - 10°	flat (-1)	Urban (no change)
10 - 50 m	loss (1)	20° - 25°	north (0 - 22.5)	Urban to Forest
50 - 100 m		25° - 40°	northeast (22.5 - 67.5)	Urban to Agriculture
100 - 200 m		40° - 65°	east (67.5-112.5)	Forest to Urban
200 - 1000 m		> 65°	southeast (112.5 - 157.5)	Forest (no change)
> 1000 m			south (157.5 - 202.5)	Forest to Agriculture
			southwest (202.5 - 247.5)	Agriculture to Urban
			west (247.5 - 292.5)	Agriculture to Forest
			northwest (292.5 - 337.5)	Agriculture (no change)
			north (337.5 - 360)	

The Frequency Ratio (FR) aids in understanding location specific conditions for landslide occurrence by providing the ratio of the landslide area to the total area. Figure 3.5. shows a matrix diagram of the FR for each landslide inventory and LULC change scenario. FR values less than one are represented by dark blue. From Figure 3.5., we can see that all categories including urban produced FR values less than one. The scenario from forest to agriculture was only found significant in the Sin Ho, Vietnam with a FR of 1.63 and Hakha, Myanmar with a FR of 1.94. The scenario agriculture with no change in ten years prior to the landslide event had FR values greater than one for half of the inventory locations. Forests with no change had FR values greater than one for all but one location (Tam Duong, Vietnam). However, the highest FR values were for the LULC change scenario from agriculture to forest, ranging from 0 to 8.15 over the 18 landslide inventory locations. This

scenario had relatively high FR values of 5.14 for Nha Trang, Vietnam; 6.33 for Vi Xuyen, Vietnam; 6.72 for Muong La, Vietnam; and the highest FR value of 8.15 for the landslide inventory in Phu Yen, Vietnam. The change observed from agriculture to forest could be a representation of agricultural abandonment, where the agricultural fields are left to naturally recover and revegetate. Spruce et al. (2020) observed similar changes from agriculture to forest in the Lower Mekong between the period from 1997 to 2010. These high FR values could be explained by agricultural abandonment practices having an impact on landslide occurrence which would be consistent with the results found by Persichillo et al. (2017) and Deng et al. (2018).

Table 3.5. Mean percentage of total area averaged over all locations

LULC change scenario over 10 years			
	Urban	Forest	Agriculture
Urban	0.93 %	0.003 %	0.05 %
Forest	0 %	81.48 %	0.31 %
Agriculture	0.03 %	2.11 %	15.05 %

Table 3.6. Sum of landslides within all locations

LULC change scenario over 10 years			
	Urban	Forest	Agriculture
Urban	0	0	0
Forest	0	15,508	60
Agriculture	0	614	2,530

Table 3.7. Mean Frequency Ratio averaged over all locations

LULC change scenario over 10 years			
	Urban	Forest	Agriculture
Urban	NA	NA	NA
Forest	NA	2.06	0.20
Agriculture	NA	2.83	1.64

In addition to assessing the LULC within the extents of the 18 landslide event inventories, land cover changes were also analyzed over the greater Lower Mekong region from 1998 to 2018. The urban areas increased by 11.3% from 1998 to 2001 and increased constantly at an average rate of 1.2% per year. The area represented by forests decreased by 5.5% of the total area from 1998 to 2001 with an average decrease of 0.3% per year. In contrast, the amount of agricultural area increased drastically by 11.6% from 1998 to 2001 with an average increase of 0.6% per year. The percentage of total area represented by each of the three LULC categories from 1998 to 2018 are shown in Figure 3.7. From this figure we can observe that the amount of agricultural land increased by approximately the same area that of which the forests decreased from 1998 to 2001. Figure 3.7. shows that the majority of the Lower Mekong region is forested ranging from 67 – 63% of the total area for the time period from 1998 to 2018. About a third of the area is classified as agricultural land, ranging from 30 – 34%, and the smallest percentage of total area of the region is classified as urban, ranging from 0.9 – 1.1%. Figure 3.8. shows the percentage of total area represented by each LULC change scenario over the greater Lower Mekong region between 1998 and 2018. The LULC can be summarized as 62.1% forest unchanged, 29.1% agricultural area unchanged, 5.8% changed from agriculture to forest, 1.7% changed from forest to agriculture, 0.9% urban unchanged, and the combined land cover change scenarios of urban to forest, urban to agriculture, and agriculture to urban constitute merely 0.3% of the total area.

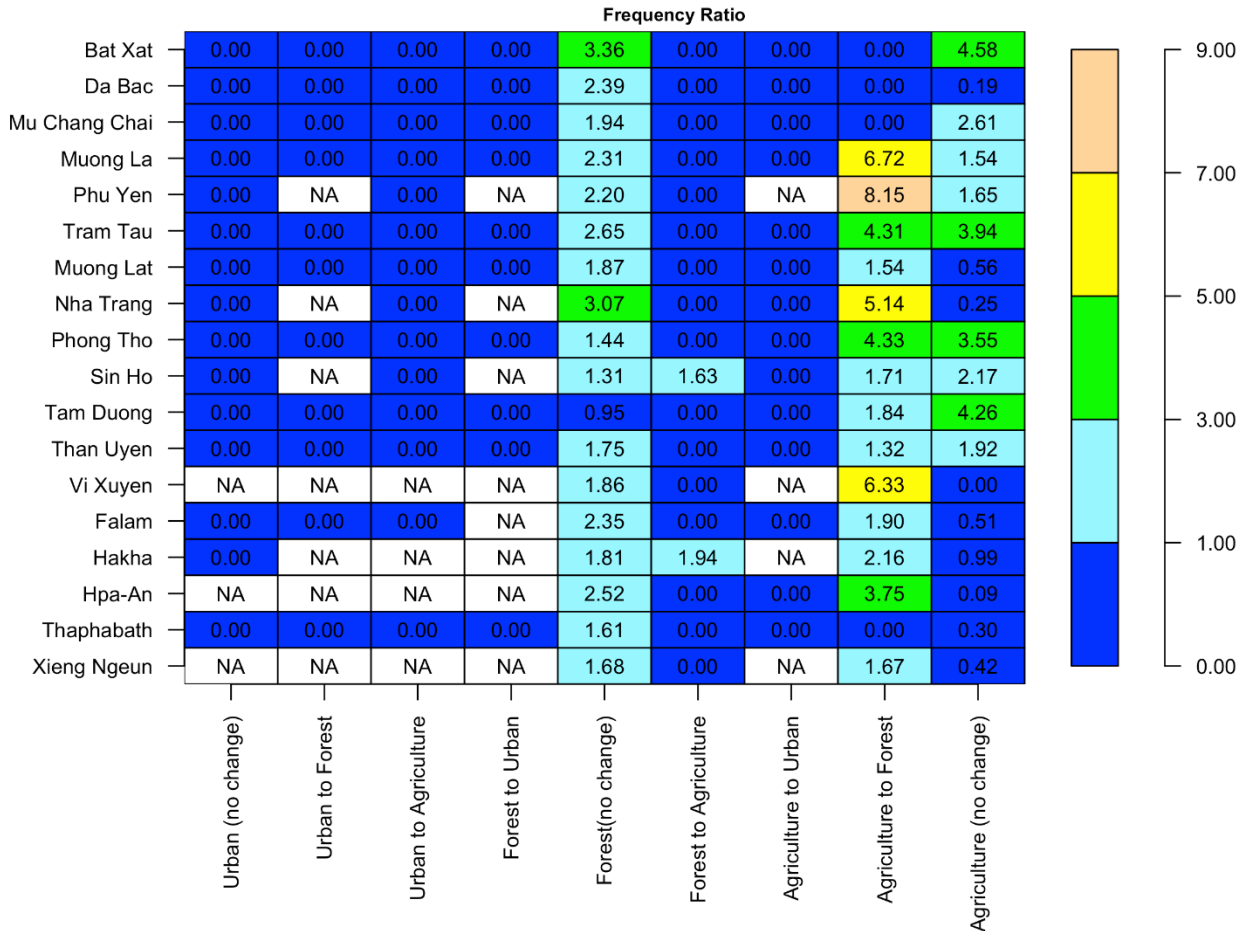

Figure 3.5. Matrix diagram displaying the FR for each landslide inventory location and LULC change scenario. FR values < 1 are represented by dark blue and no data values by 'NA' in white.

A logistic regression model was trained and validated for the extents of 18 landslide event inventories. Table 3.8. presents a summary of the logistic regression coefficients and p-values of all models for the landslide inventory locations with greater than 1000 landslides to avoid potential overfitting from the smaller observation counts. The logistic regression model results for each of the 18 inventories are provided individually in Online Resource 1. In Table 3.8., the inventory abbreviations are shown next to the corresponding values for the minimum and maximum coefficient and p-value for each category within the factors. From this table, Muong Lat (MT) represents the highest coefficients in the land cover change corresponding to forest (no change), agriculture to forest, and agriculture (no change). When examining the

LULC over the inventory location, the landslides largely occur in a forested area with no variation in land cover. The land cover in the Muong Lat (MT) area is fairly homogenous with minimal area represented by the land cover change scenarios other than forest (no change). However, several landslides did occur within areas that underwent deforestation for agriculture and in invariable agricultural areas. The model trained with the Da Bac (DB) inventory produces minimum coefficients for all distance to roads categories which indicates that in this area, the presence of roads is not very influential on landslide occurrence. When examining the Da Bac (DB) location, there is an ample road network throughout the province, but the landslide distribution does not appear to be influenced by the presence or absence of roads and the landslides do not cluster around roads.

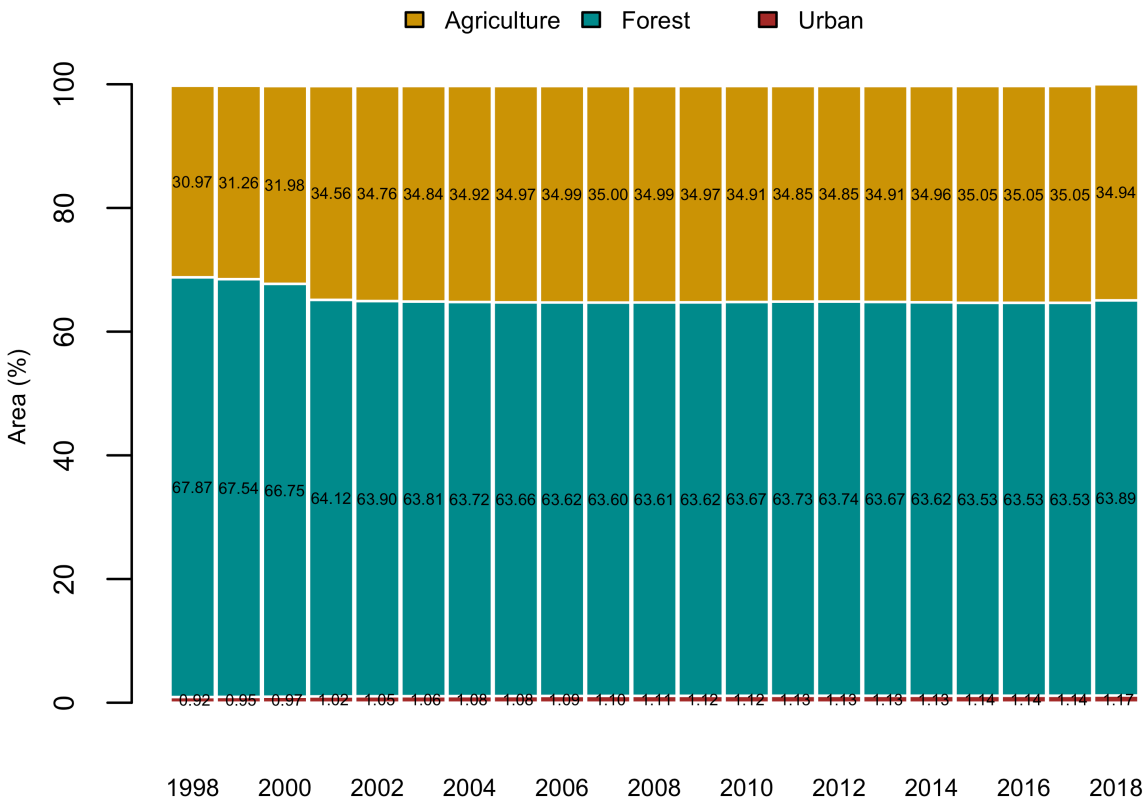

Figure 3.6. Bar plot of the percentage of total area of each land cover classification within the Lower Mekong River Basin annually from 1998 to 2018.

Furthermore, Mu Chang Chai (MC) contributes to the minimum coefficients for the slope categories which could indicate that slope is less influential in this location, even though the p-values corresponding to the slope factor were not significant. The inventory mapped in Mu Chang Chai (MC) occurred in a mountainous forested area with varying slope. The inventory in Mu Chang Chai (MC) produced the highest coefficient for forest loss and the minimum p-value which could be explained by a large cluster of landslides occurring around an area that had experienced substantial forest loss in the years prior to the event. Mu Chang Chai (MC) also represents the maximum coefficients for proximity to roads indicating that roads are more influential on landslides in this location compared to other inventories. When looking closely at the area, the landslide distribution appears to be influenced by proximity to the road network. However, the p-values corresponding to distance to roads in the Mu Chang Chai (MC) inventory indicate this factor was not found to be statistically significant in the logistic regression model. Overall, the coefficients for distance to roads decrease with distance indicating that road proximity has an influence on landslide occurrence. This would agree with the findings of Larsen & Parks (1997) which identified that landslide frequency decreased as distance to roads increased in Puerto Rico.

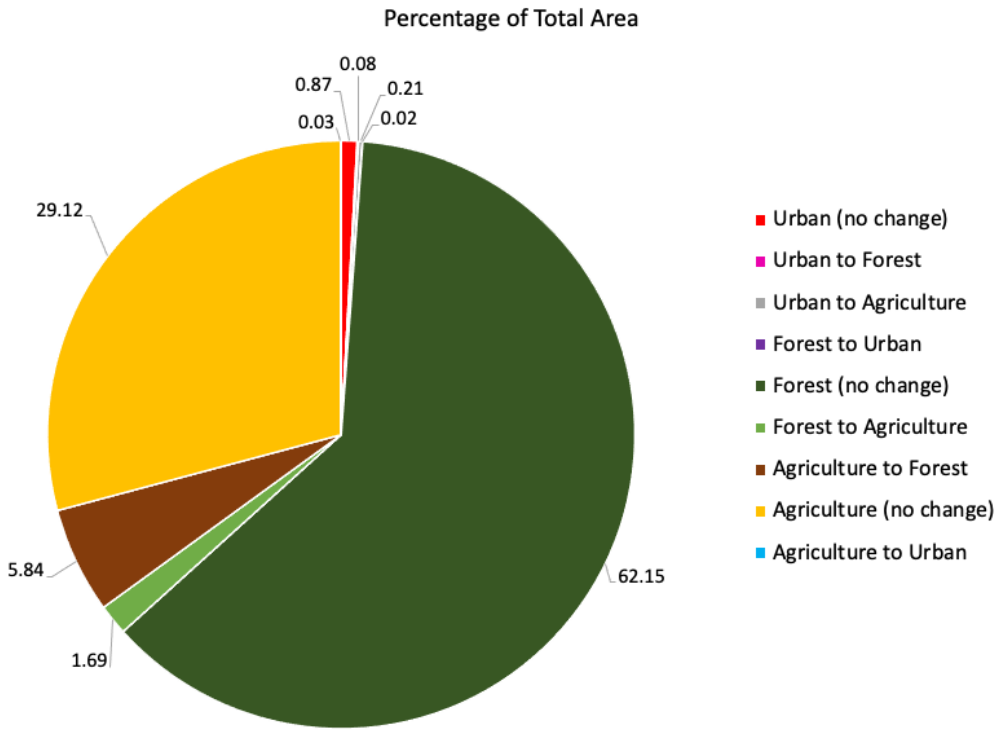

Figure 3.7. Pie chart depicting the percentage of total area represented by each LULC change scenario over the greater Lower Mekong region between 1998 and 2018.

The Logistic Regression models were validated using 30 % of the landslide inventories as well as randomly generated non-landslide points. The models were validated by plotting the true positive rate versus the false positive rate (ROC) and calculating the area under the resulting curve (AUC). The AUC values from the validation of the Logistic Regression model and the number of landslides within each landslide inventory are presented in Table 3.9. The model validation results found all AUC values to be estimated above 0.7 except for one inventory in Hakha, Myanmar with an AUC value equal to 0.697. This was the lowest AUC amongst the model results indicating the model trained for Hakha, Myanmar did not perform as well compared to the other locations. The model trained for Thaphabath, Laos outperformed the other models based on having the highest AUC value of 0.958. The average AUC value of all 18 models is 0.82. Based on the model validation results in Table 3.9., the number of landslides and AUC values are not correlated indicating the number of landslides within each location used to train the models did not affect the model performance.

Table 3.8. Summary of Logistic Regression Coefficients and P-Values over all inventory locations

Factor	Category	Coefficient			P-value		
		min	max	mean	min	max	mean
	Intercept	-21.78 MT	-2.84 DB	-13.02	1.99E-05 PY	9.83E-01 MC	6.24E-01
Land Cover Change	Urban to Forest	-9.76 FM	0.71 MT	-3.51	8.02E-02 PY	1.00E+00 MT	6.88E-01
	Forest to Urban	-15.73 PY	-9.11 FM	-12.63	9.73E-01 PY	9.84E-01 HK	9.79E-01
	Forest (no change)	-0.61 DB	16.33 MT	5.48	6.71E-06 FM	9.87E-01 MT	4.29E-01
	Forest to Agriculture	-13.65 XN	3.99 MT	-5.41	4.39E-01 FM	9.98E-01 TT	8.83E-01
	Agriculture to Urban	-13.12 PY	-10.58 FM	-12.02	9.71E-01 FM	9.91E-01 PY	9.82E-01
	Agriculture to Forest	-15.46 MC	16.01 MT	0.26	3.39E-05 FM	9.87E-01 MT	5.03E-01
	Agriculture (no change)	-1.29 DB	14.79 MT	3.76	2.20E-25 MC	9.88E-01 MT	3.19E-01
Distance to Road	20 - 50 m	-2.06 DB	15.54 MC	4.15	5.20E-02 DB	9.86E-01 MC	6.50E-01
	50 - 100 m	-1.04 DB	15.65 MC	2.73	1.67E-01 FM	9.86E-01 MC	6.05E-01
	100 - 200 m	-1.30 DB	16.02 MC	4.21	1.77E-01 DB	9.86E-01 MT	6.76E-01
	200 - 1000 m	-0.65 DB	16.30 MC	4.53	3.80E-01 FM	9.85E-01 MC	6.79E-01
	> 1000 m	-1.19 DB	15.86 MC	5.45	2.20E-01 DB	9.87E-01 XN	6.39E-01
	60 - 100 cg/cm^3	-1.13 PY	-0.88 FM	-1.01	1.12E-01 PY	3.61E-01 FM	2.36E-01

Soil Bulk Density	100-130 cg/cm^3	-1.32	FM	1.28	MT	-0.36	2.28E-18	MC	6.77E-01	DB	2.93E-01
Forest Loss	forest loss = 1	-0.77	FM	2.48	MC	0.67	4.13E-14	MC	4.73E-01	HK	6.47E-02
Slope	10 - 20 deg	0.58	DB	2.07	XN	1.41	1.26E-15	FM	1.95E-01	DB	2.76E-02
	20-25 deg	0.49	MC	3.17	MT	2.12	2.95E-24	FM	7.29E-02	MC	9.13E-03
	25 - 40 deg	0.22	MC	4.09	MT	2.70	5.15E-32	FM	3.93E-01	MC	4.92E-02
	40 - 65 deg	0.40	MC	4.42	DB	2.97	2.30E-27	FM	3.67E-01	MC	4.59E-02
	> 65 deg	-15.52	MC	3.33	XN	-9.60	2.41E-02	XN	9.93E-01	PY	8.33E-01
Aspect	North	-2.20	TT	-0.64	FM	-1.24	9.32E-06	FM	1.34E-01	XN	3.20E-02
	East	0.35	HK	1.85	DB	1.16	1.69E-12	FM	3.09E-02	HK	3.87E-03
	Southeast	0.96	HK	2.90	DB	1.94	3.18E-26	FM	1.34E-09	HK	1.68E-10
	South	0.53	HK	3.12	DB	1.80	5.27E-21	DB	1.32E-03	HK	1.66E-04
	Southwest	-0.12	HK	2.48	DB	1.27	4.77E-14	XN	5.11E-01	HK	6.39E-02
	West	-0.53	HK	1.64	XN	0.24	1.70E-08	XN	4.43E-01	PY	1.51E-01
	Northwest	-2.50	TT	0.98	XN	-0.86	1.77E-06	HK	5.95E-01	MC	7.78E-02

*Color coded abbreviations correspond to the landslide inventories in Table 3.9.
**Red mean values represent the maximum within each factor and blue mean values represent the minimum within each factor

Table 3.9. Model validation results (AUC) for each inventory location

District	**Country**	**Landslides**	**Validation Landslides**	**AUC**
(BX) Bat Xat	Vietnam	99	33	0.820
(DB) Da Bac	Vietnam	1086	358	0.892
(MC) Mu Chang Chai	Vietnam	1256	414	0.854
(ML) Muong La	Vietnam	758	250	0.835
(PY) Phu Yen	Vietnam	1368	451	0.856
(TT) Tram Tau	Vietnam	1490	492	0.844
(MT) Muong Lat	Vietnam	1718	567	0.794
(NT) Nha Trang	Vietnam	207	68	0.853
(PT) Phong Tho	Vietnam	302	100	0.906
(SH) Sin Ho	Vietnam	707	233	0.816
(TD) Tam Duong	Vietnam	159	52	0.838
(TU) Than Uyen	Vietnam	312	103	0.713
(VX) Vi Xuyen	Vietnam	157	52	0.755
(FM) Falam	Myanmar	5086	1678	0.732
(HK) Hakha	Myanmar	1737	573	0.697
(HA) Hpa-An	Myanmar	992	327	0.869
(TB) Thaphabath	Laos	242	80	0.958
(XN) Xieng Ngeun	Laos	1178	389	0.740

* Colors correspond to landslide inventories highlighted in Table 3.8.

3.5. Discussion

The land cover of the inventories used in this study were dominated by forests with minimal LULC changes present. According to Table 3.5., the scenarios of LULC change from forest to urban, agriculture to urban, urban to forest, and urban to agriculture combined make up only 0.082 % of the total area averaged over the 18 inventory locations. Looking at the LULC analysis over the LMRB in Figure 3.7., the relatively small area occupied by urban areas may make it difficult to see any conclusive patterns in landslide activity. The LULC scenarios involving urban activities were less prominent in the landslide inventories used in this study, but also occupy the lowest amount of total land area in the greater Lower Mekong region so this category is not only less represented in the 18 landslide inventory area locations, but overall in the Lower Mekong River Basin. The amount of area occupied by urban and built-up classification is not comparable to the amount of agricultural and forested areas in the LMRB. Additionally, the scenario involving urban activities did not experience any landslides within the 18 inventories used in this study. Therefore, the impact of LULC change scenarios to or from the urban classification cannot be fully determined using the 18 inventories presented in this study.

The Frequency Ratio (FR) reveals potential correlation between landslide locations and causative factors in the area. Overall, the scenario from agriculture to forest had the highest average FR value followed by the scenario of forest with no change (Figure 3.5.). The forested areas that experienced no change had an average FR value of 2.06 when averaged over all 18 study locations, and this is most likely due to the prevalence of forested mountainous regions with steep slopes where most landslides occur in this region. The results of this study indicate that the land cover change scenario from agriculture to forest could have an impact on landslide occurrence and that areas changing from agriculture to forest may be more susceptible to landslides in the years following the land cover change. This could indicate that abandoned agricultural lands left to naturally recover are more susceptible to landslide activity than other land cover change scenarios, which would be similar to the conclusions drawn by Persichillo et al. (2017) and Deng et al. (2018). Agricultural areas on mountainous slopes have a higher

probability of being abandoned, and dense forests following agricultural abandonment have been shown to increase landslide susceptibility (Mantero et al., 2020; Faccini et al, 2017; Pisano et al., 2017).

Further evaluation of land cover change from agriculture to forest with landslide inventories where this LULC change scenario is more prevalent than the inventories used here needs to be executed to further understand the impact of land use changing from agriculture to forest as invariable forests dominate the areas used in this study. Additionally, the FR being a univariate analysis must be taken into consideration. The areas where landslides occurred that were deforested for agricultural purposes could be influenced by additional factors. Other limitations include the spatial resolution and the availability of remotely-sensed datasets for the region. For example, the finest resolution for publicly available DEM data for the Lower Mekong River Basin is 30 meters, which is much coarser than other regions such as USA with one-meter DEM available. With landslides ranging in size, coarser spatial resolutions may not accurately represent the environment of very small, shallow slope failures. Enhanced spatial resolution of remotely sensed data would greatly benefit modelling efforts for landslide susceptibility in the Lower Mekong River Basin.

We can make generalized conclusions for the 18 inventory locations and models regarding landslide causative factors using the coefficients and p-values from Table 3.8. When averaged over all 18 models the causative factors associated with distance to roads, forest loss, and slope display positive coefficients, which is expected considering these variables are known to be influential on landslide occurrence. Overall, the most significant variables based on the mean p-values were slope and aspect. The high significance of aspect could be explained by the models using flat as the basis factor. When considering all 18 inventories, the logistic regression models did not indicate that areas changing from agriculture to forest were as influential on landslide occurrence as the FR analysis did, which could be explained by the FR being a univariate analysis and the Logistic Regression being multivariate. However, the average coefficient for the LULC change category of agriculture to forest has the only positive coefficient of any of the change scenarios besides forest and agriculture with no change. Forest with no LULC change had the

highest and only positive average coefficient relative to the other land cover change scenarios which is most likely due to the majority of landslides in this study occurring in steep forested areas and the considerable amount of forested area throughout the study locations. Areas that changed from forest to urban have the lowest average coefficient which could be explained by the limited number of landslide points within the area represented by this scenario in the inventories. Alternatively, this could mean that areas being developed are not susceptible to landslides due to other factors such as low slope which could indicate informed land management decisions in the region.

3.6. Conclusions

Land use and land cover (LULC) changes can affect slope stability and geological conditions that may influence the occurrence of landslide activity. This study assessed the influence of LULC changes on landslide susceptibility for 18 locations throughout the Lower Mekong River Basin (LMRB). The majority of landslides occurred in the LULC change scenario with the largest land coverage percentage, which is forested areas that did not experience any change in land cover. However, the LULC change scenario from agriculture to forest had the highest FR values overall. Both the FR analysis and LR models indicated that the LULC change scenario from agricultural land to forest could positively correlate with landslide occurrence. However, for real-time analysis the LULC data available on the SERVIR-Mekong Land Cover Portal would be needed to be updated each year as currently, maps are only available only up to 2018.

There were data limitation issues regarding the representation of land cover changes in the extent of the landslide inventories. Not all land cover change scenarios are represented in these study areas, more locations with landslide inventories that experienced land cover changes are needed to fully analyze the influence of LULC on landslide susceptibility. This method can further be applied to new landslide inventories for other locations in the Lower Mekong River Basin as the data becomes available to discover more consistent correlations between LULC change and landslide susceptibility. Specifically, the relationship between agricultural abandonment and landslide occurrence could be further analyzed to determine how this LULC

change influences susceptibility in the Lower Mekong Region. The inclusion of dynamic LULC in landslide susceptibility models could greatly improve hazard assessment and should be investigated as the combination of land use changes over time due to population expansion and disturbances caused by climate change. This analysis is done primarily using remote sensing products, making it transferable to other landslide-prone regions around the world. Additional research efforts could further investigate the role of agricultural abandonment and natural recovery on rainfall-triggered shallow landslides.

4. Chapter 4. Spatial and Temporal Analysis of Global Landslide Reporting

Associated citations:
(1) Dandridge, C.; Stanley, T.A.; Kirschbaum, D.B.; Lakshmi, V. Spatial and Temporal Analysis of Global Landslide Reporting Using a Decade of the Global Landslide Catalog. Sustainability, 2023, 15, 3323. https://doi.org/10.3390/su15043323
(2) Dandridge, C.; Stanley, T.A.; Kirschbaum, D.B.; Lakshmi, V. A Decade of the Global Landslide Catalog: Spatial and Temporal Analysis, Applications, and Limitations, NH35E-0501 presented at 2021 Fall Meeting, AGU, December 13-17.

4.1. Introduction

Rainfall-triggered landslides are a mounting global concern due to increased frequency of extreme precipitation due to climate change (Crozeir, 2010; Gariano & Guzzetti, 2016; Marc et al., 2022). Quality landslide inventories are necessary for assessing landslide risk and hazard (Froude & Petley, 2018; Emberson et al., 2022). NASA's global landslide catalog (GLC) compiles a record of rainfall triggered landslides globally from news reports, academic papers, and pre-existing databases at NASA Goddard Space Flight Center. Landslides are not recorded consistently across the globe, with that being said the GLC represents a minimum number of landslide reports from 2007 to 2018. The original framework and collection methods for the GLC are detailed in Kirschbaum et al. (2010). Comprehensive analyses of the GLC database were also undertaken in Kirschbaum et al. (2012) and Kirschbaum et al. (2015). Single event entries in the GLC may consist of multiple landslides near one another triggered by the same rainfall event. The GLC is published along with other landslide inventories in the Cooperative Open Online Landslide Repository (COOLR), which contains landslides reported by citizen scientists and other inventories from the broader research community (Juange et al., 2019). Even though the GLC is no longer being compiled, landslides can still be reported using the Landslide Reporter application and added to the COOLR collection. The GLC represents all landslides triggered by rainfall including mudslides, rockslides, and debris flows. Each event includes location information (nominal and geographic), time of event, triggering mechanism, type of landslide, relative size, location accuracy, impacts such as estimated economic damage, casualties, and

fatalities. The location accuracy is based on a qualitative radius of confidence in kilometers. Location accuracy provided in the GLC is affected by the capability of the news reports to convey the location information and preciseness. Additionally, the GLC may not be complete for non-English-speaking countries due to the collection method and most reports originating from English-language media (Kirschbaum et al., 2015). The year 2010 yielded the highest number of annually recorded events in the GLC, which can be attributed to unusually high precipitation and increased landslide events globally compared to other years. A detailed analysis of the anomalies in 2010 has been performed and discussed by Kirschbaum et al., (2012).

Historically, there have been few efforts to compile landslides at global scale (Petley, 2012). Detailed landslide inventories are more commonly found at regional or national scale (Abella & Van Westen, 2007; Chau et al., 2004, Guzzetti, 2000; Mirus et al., 2020; Hughes & Schulz, 2020) or are event-based after a significant rainfall event (Bhandary et al., 2013; Amatya et al., 2022; Marc et al., 2018). However, Froude and Petley (2018) present a global database of fatal landslides from 2004 to 2016, but it does not include non-fatal events. There are several methods to produce landslide inventories and most are event-based or region-specific. For example, Bessette-Kirton et al. (2019) present landslides triggered by Hurricane Maria in 2017 in Puerto Rico that were mapped using post-storm satellite and aerial imagery. From their mapping, an estimated 40,000 landslides occurred as a result of the hurricane event. The national landslide inventory for Cuba only represents landslides that cause major damage and does not reveal qualitative information for most of the landslides in the inventory or represent the entire country (Abella & Van Westen, 2007). The AVI project is the most extensive database for landslides and floods in Italy with events manually gathered from historical news articles and scientific reports from 1918 to 1990 (Guzzetti et al., 1994). Alternatively, Amatya et al. (2019) utilized high-resolution imagery from 2012 and 2018 with object-based image analysis to map a landslide inventory along the Karnali Highway in Nepal, and then several inventories in Southeast Asia in Amatya et al., (2021). This method was able to identify almost 60% of the landslides identified manually. The Fatal Landslide Event Inventory of China (FLEIC) is a record of 1911 landslides from 1950 to 2016. Each entry represents a single landslide gathered from geological records, media reports, and literature (Lin & Wang,,

2018). The GLC can be used to supplement existing inventories that may be limited temporally or spatially.

Several landslide studies have used the GLC in their creation of landslide databases and to assess global patterns of landslides. Lin and Wang (2018) used events in the GLC to analyze fatal landslides in China and create the Fatal Landslide Event Inventory of China (FLEIC). They also used the same methodology to determine the location and radius of confidence for additional landslides in China. This study noted that the short time period available in the GLC (less than ten years) limited temporal trend analysis. Chandrasekaran et al. (2013) investigated damages to infrastructure in Nilgiris, India caused by rainfall-induced landslides using the GLC. They found that roughly ten percent of global landslide fatalities occurred in India. Benz and Blum (2019) proposed an algorithm to detect global landslide clusters triggered by the same rainfall event and applies it to events reported in the GLC. They found that more than 40% of events can be related to another event, and 14% of events are part of a cluster with more than ten landslides triggered by the same rainfall event with results varying greatly geographically. Culler et al. (2021) evaluates post-fire landslide susceptibility in different regions across the globe using the GLC for landslide events and comparing antecedent precipitation at burned and unburned locations from MODIS. They found that wildfires increase landslide susceptibility, but post-fire landslides are not uniform and vary geographically. This study noted that the GLC was chosen because it offered the largest spatial and temporal range of any landslide inventory. Whiteley et al. (2019) included the GLC in their review of geophysical monitoring of global rainfall-triggered landslides to draw the conclusion that landslide distribution is not uniform across the globe. Additionally, Froude and Petley (2018) used the GLC in their analysis of global fatal landslides from 2004 to 2016. They found that most fatal landslide clusters occur around cities in countries with lower gross national income.

Furthermore, the GLC has been used in several studies to train and validate landslide models. Lin et al. (2017) used landslides from the GLC and the World Geological Hazard Inventory as training and validation data for a logistic regression model for global landslide susceptibility. Farahmand and Aghakouchak (2013) used 581 events from 2003, 2007, 2008, and 2009 in the GLC as training and validation data for a support vector machines machine learning

algorithm to predict global landslides. This study noted that the GLC is composed of major landslides and therefore, the model is not calibrated for small landslides. The model reliably predicted historical landslides. Liao et al. (2010) proposed an early warning system for rainfall-triggered landslides over Java Island, Indonesia using events in the GLC from 2003 and 2007 and the SLIDE (slope infiltration distributed equilibrium) model with NASA's Tropical Rainfall Measurement Mission (TRMM) precipitation estimates. Kirschbaum et al. (2015a) used the GLC within the LHASA framework for Central America and Hispaniola. This study related GLC events to long-term precipitation from TMPA from 2001 to 2013. The LHASA model was able to correctly identify the potential for most GLC events. This study noted that the GLC is the only event-based database for landslides across all countries within Central America and the Caribbean region. Furthermore, Kirschbaum et al. (2012) compared GLC events from Hurricane Mitch in Central America in 1998 to the susceptibility maps globally and regionally, and all the nine landslides occurred in high susceptibility zones in the regional map, and eight landslides occurred in high susceptibility zones in the global map.

Following the analysis of the GLC by Kirschbaum et al. (2015b), this research further examines various attributes and limitations associated with the landslide information reported by the GLC using a longer time period of recorded events. Global patterns of landslides and associated fatalities are examined both geographically and temporally. Fatality and landslide hotspots are assessed at global and continental scale. The GLC has not previously been compared against other landslide inventories. Here, we evaluate twenty-seven region-specific event inventory databases and their similarities and differences against events reported in the GLC. A quantitative spoken language analysis has yet to be performed with the GLC reports. To determine if there is any bias regarding the language of reported events in the GLC, the relationship between spoken language and landslide reporting is investigated. The economic status of varying regions could affect the amount and method of landslide reporting, thus economic variables are compared against landslide activity reported in the GLC to determine the effect of economic status on landslide event reporting. The results of this study give a deeper understanding of the global patterns of landslide reporting, and are also useful for applying the GLC in rainfall-triggered landslide analysis.

4.2. Data

This section lists and describes the datasets used for analysis in this research and organizes the information in Table 4.1.

Table 4.1. Data descriptions and source information.

Name	Description	Source
Global Landslide Catalog	Global compilation of rainfall-triggered landslides from 2007 to 2018	[6]
Area (km^2)	A country's total area	[32]
Population Density (people/km^2)	Midyear population divided by land area in square kilometers	[33]
GDP per Capita (USD)	Gross Domestic Product (GDP) divided by the midyear population	[34]
Landslide Hazard	Global landslide susceptibility map	[5, 35]
Landslide Inventories	Landslide event inventories from 2008 to 2018	[3, 17, 36–38]
	Region-specific landslide inventory for the Apulian region of southern Italy collected from 2008 to 2016	[39]

4.2.1. GLC

The Global Landslide Catalog (GLC) is a record of landslides collected from news reports, academic articles, and pre-existing inventories. The GLC is compiled and maintained at NASA Goddard Space Flight Center. However, the GLC is no longer active and no additional years beyond 2018 will be added. There are a total of 11,334 landslides in the GLC that occur between 2007 and 2018, which are publicly available as geospatial point or tabular data (Kirschbaum et al., 2010).

4.2.2. Land Area

The land area data from World Bank is defined as a country's total area, excluding area under inland water bodies, national claims to continental shelf, and exclusive economic zones. The land area estimates are reported in km^2. A full data description and download information are available from https://data.worldbank.org/indicator/AG.SRF.TOTL.K2.

4.2.3. Population Density

The population density data from World Bank is defined as the midyear population divided by land area in square kilometers. A full data description and download information are available from https://data.worldbank.org/indicator/EN.POP.DNST.

4.2.4. Gross Domestic Product per Capita

The Gross Domestic Product (GDP) data from World Bank is the sum of gross value added by all resident producers in the economy plus any product taxes and minus any subsidies not included in the value of the products. The GDP per capita is the GDP divided by the midyear population. Values are collected from the latest year available for each country. A full data description and download information are available from https://data.worldbank.org/indicator/NY.GDP.PCAP.CD.

4.2.5. Landslide Susceptibility

The global landslide susceptibility map has a spatial resolution of roughly 1 km and covers most of the world's land surface, but not Antarctica. The susceptibility model combines slope, geology, road networks, faults, and forest loss using a heuristic fuzzy methodology (Emberson et al., 2022; Stanley & Kirschbaum, 2017). Susceptibility is classified by increasing severity as very low, low, medium, high, and very high. The receiver operating characteristic (ROC) curve and area under the curve (AUC) is used to assess the performance of the global susceptibility map. The AUC ranges from 0.61 to 0.85 when compared against local landslide inventories from varying locations across the globe, and the AUC when compared against the GLC is 0.82. Further explanation on the quality of the map can be found in Stanley and Kirschbaum (2017). In this research, the global susceptibility rating is extracted for each point representing an event in the GLC.

4.2.6. Landslide Inventories

Twenty-seven landslide event inventories from 2008 to 2018 were created via object-based image analysis, developed by Amatya et al. (2022); Chang et al. (2014); Chen et al. (2013); Marc et al. (2018); and Van Westen and Zhang, (2018). These inventories consist of landslides mapped after considerable rainfall events in various locations. Most landslides are able to be detected

using object-based image analysis, but the areas are not always accurate and manual correction is often necessary. Additionally, a landslide database for the Apulian region of southern Italy was collected from 2008 to 2016 by Vennari et al. (2022) and used for comparison in this study. The event inventories are provided as point or polygon shapefiles which are compared directly to the points provided in the GLC using GIS to determine how many GLC points lie within the inventories mapped extent.

4.3. Results

4.3.1. Geographic and Temporal Distribution

A global landslide susceptibility map produced by Emberson et al. (2020) and Stanley and Kirschbaum (2017) is overlaid with landslide events and hotspot estimation and shown in Figure 4.1.A. The susceptibility map is used to allocate a susceptibility rating for each point in the GLC by extracting the susceptibility map pixel value at each event location. The most notable landslide hotspots, which are highlighted in red, are in the Pacific Northwest, High Mountain Asia, and the Philippines. Figure 4.1.B shows the number and percentage of events as well as the number of fatalities for each susceptibility class. Regarding all GLC events from 2007 to 2018, 77% of reports occur in medium or higher susceptibility areas, and 32% of reports occur in very high susceptibility areas. Furthermore, areas described as having very low susceptibility are reported to have the least number of events with only 6.8% of all landslides and have the least number of fatalities associated with landslides. Overall, the number of fatalities increases with susceptibility as shown by the blue line. Figure 4.1.C shows the average number of events in black and the average number of fatalities in blue by month. On average, most events are reported in the months July, August, and September, and the least reports occur in February and November. Most fatalities are reported in June and August, and like the number of reports, the least number of fatalities are reported in February and November.

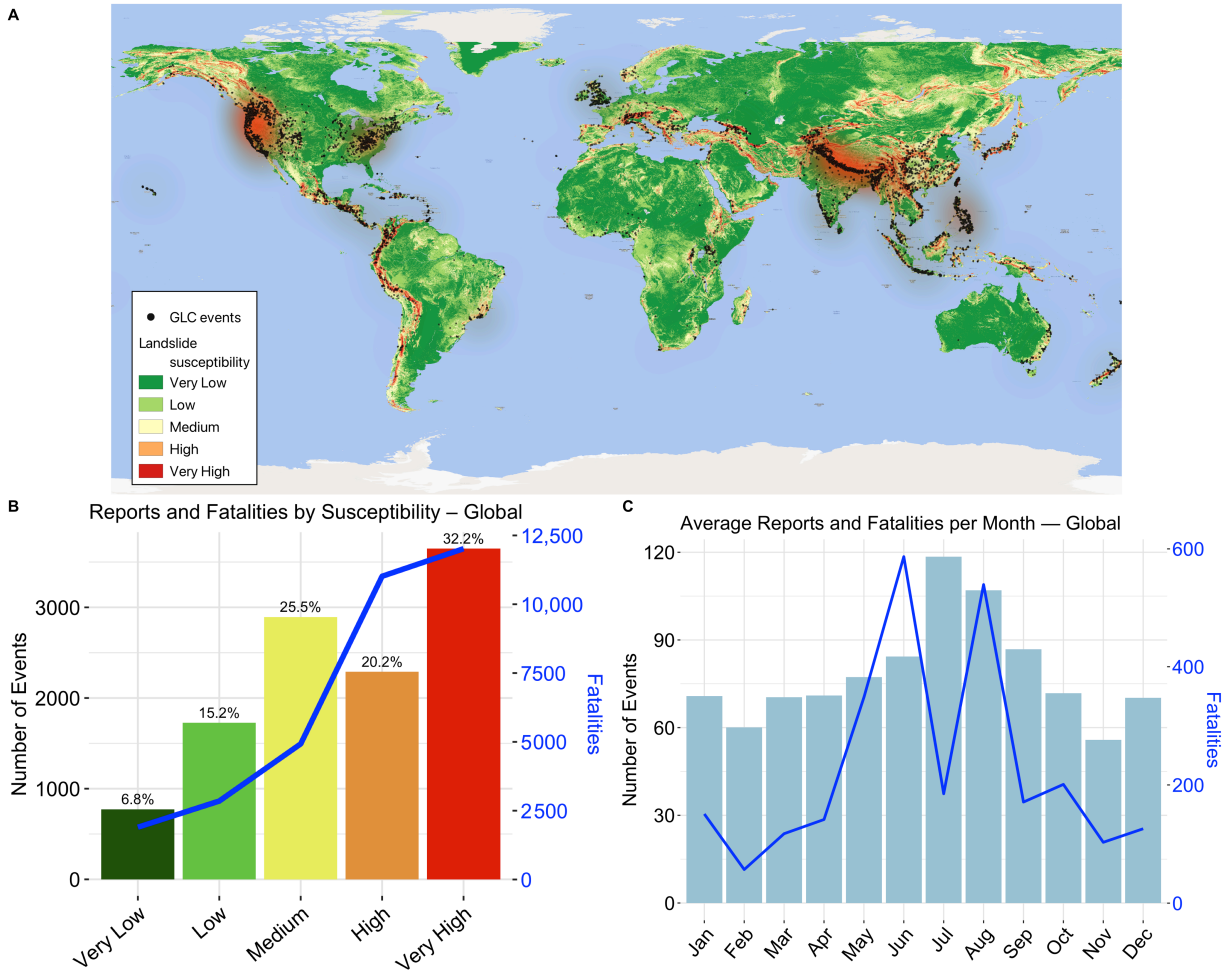

Figure 4.1. (A) Global susceptibility map overlaid with landslide events and hotspot estimation (red); (B) Total and percentage of reports and number of fatalities for each landslide susceptibility class; (C) Average number of reports and fatalities for each month.

The landslide susceptibility map and reported events as well as the distribution of fatalities throughout Asia are shown in Figure 4.2.A. Many reported events in Asia and fatalities in the GLC occur near the Himalayan Arc. Another landslide hotspot in Asia is the Philippines, reporting 769 events between 2007 and 2018. The largest fatal event in the GLC was reported to have a death toll of 5000 people and occurred after the highest 24 h rainfall in city history triggered a very large landslide near Kedarnath, India in 2013. Oddly, only 22 total events were

reported in the Russian Federation from 2007 to 2018 despite the presence of large areas susceptible to landslides. This may indicate that landslide events in the Russian Federation are underrepresented. Figure 4.2.B shows the largest portion (38%) of reports and the most fatalities occurred in very high susceptibility areas. Generally, the amount of fatalities reported increases with susceptibility. Looking at the average number of reports and fatalities by month in Figure 4.2.C, most landslides were reported in June–October with most fatalities being reported in June and August. This trend correlates with the monsoon season experienced in Southeast Asia which lasts approximately May to October (Loo et al., 2015; Petley et al., 2007).

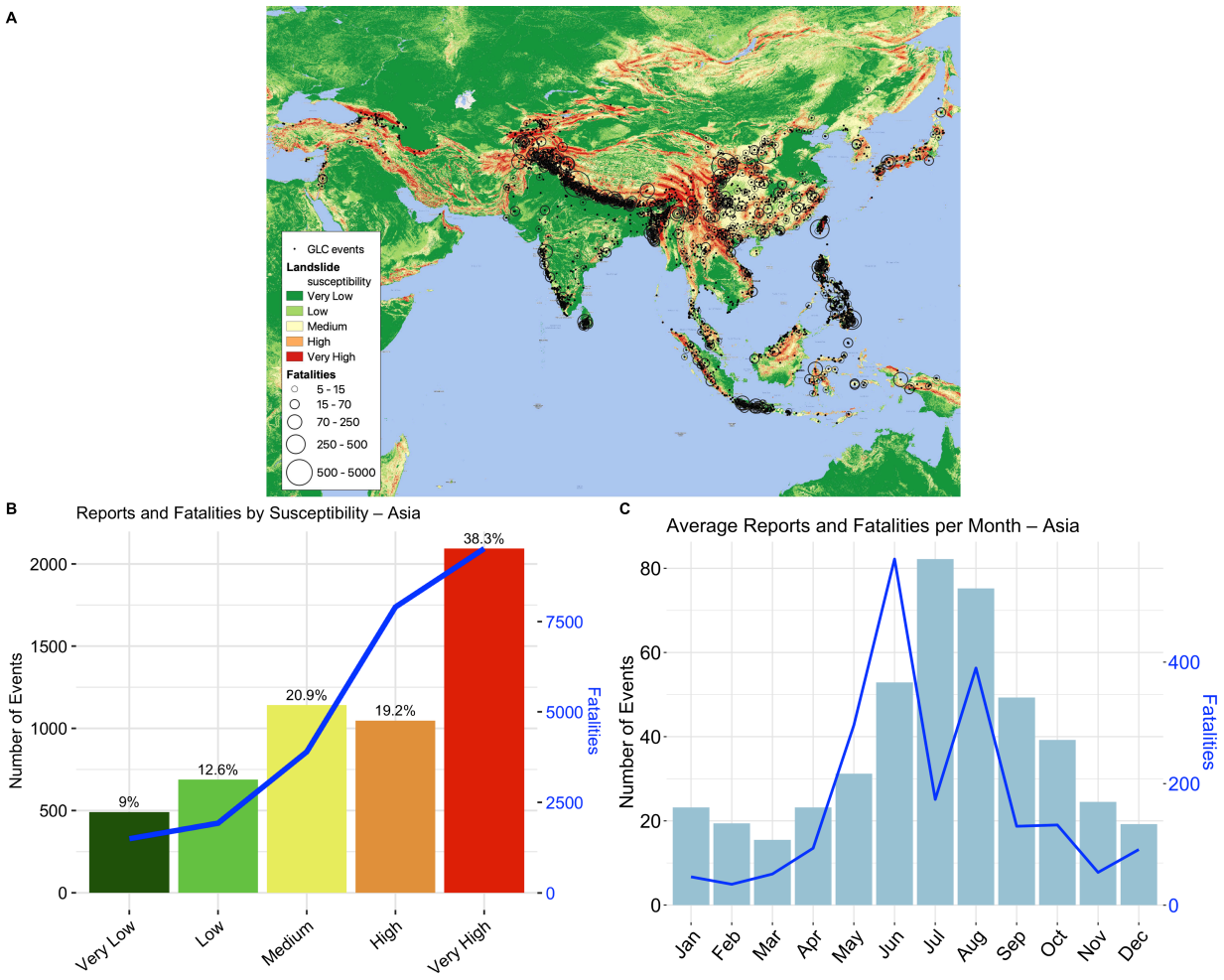

Figure 4.2. (A) Susceptibility map of Asia overlaid with landslide events and fatalities; (B) Total and percentage of reports and number of fatalities for each landslide

susceptibility class over Asia; (C) Average number and percentage of reports and fatalities for each month over Asia.

3.2. Spoken Language Analysis

The reporting language of GLC events was assessed to determine the extent of bias regarding the language of reported events in the GLC. The relationship between spoken language and landslide reporting is investigated and reported in Figure 4.3. The spoken language for each event was designated by the official language of the country reported in the GLC. The total number and percentage of reports by language are shown in Figure 4.3.A, and the number of fatal events and associated fatalities are shown in Figure 4.3.B. While the plurality (41%) of total events reported in the GLC are from English-speaking countries, the number of fatal events and total fatalities are highest for Hindi-speaking countries. The large number of fatalities reported in Hindi is a result of the 5000 fatalities associated with a single event in India. When excluding this outlier event, Chinese followed by English and Spanish have more total fatalities reported than Hindi. Hindi, Spanish, Chinese, and Nepali-speaking countries report more fatal events than English. Furthermore, India, China, Nepal, and the Philippines make up the countries with the highest number of fatal landslide events in the GLC, reporting 321, 258, 220, and 209 fatal events, respectively. This shows a reporting bias towards English-speaking countries and bias in the collection methods of the reports. More fatal landslides are reported more often than non-fatal landslides regardless of the language spoken in that location.

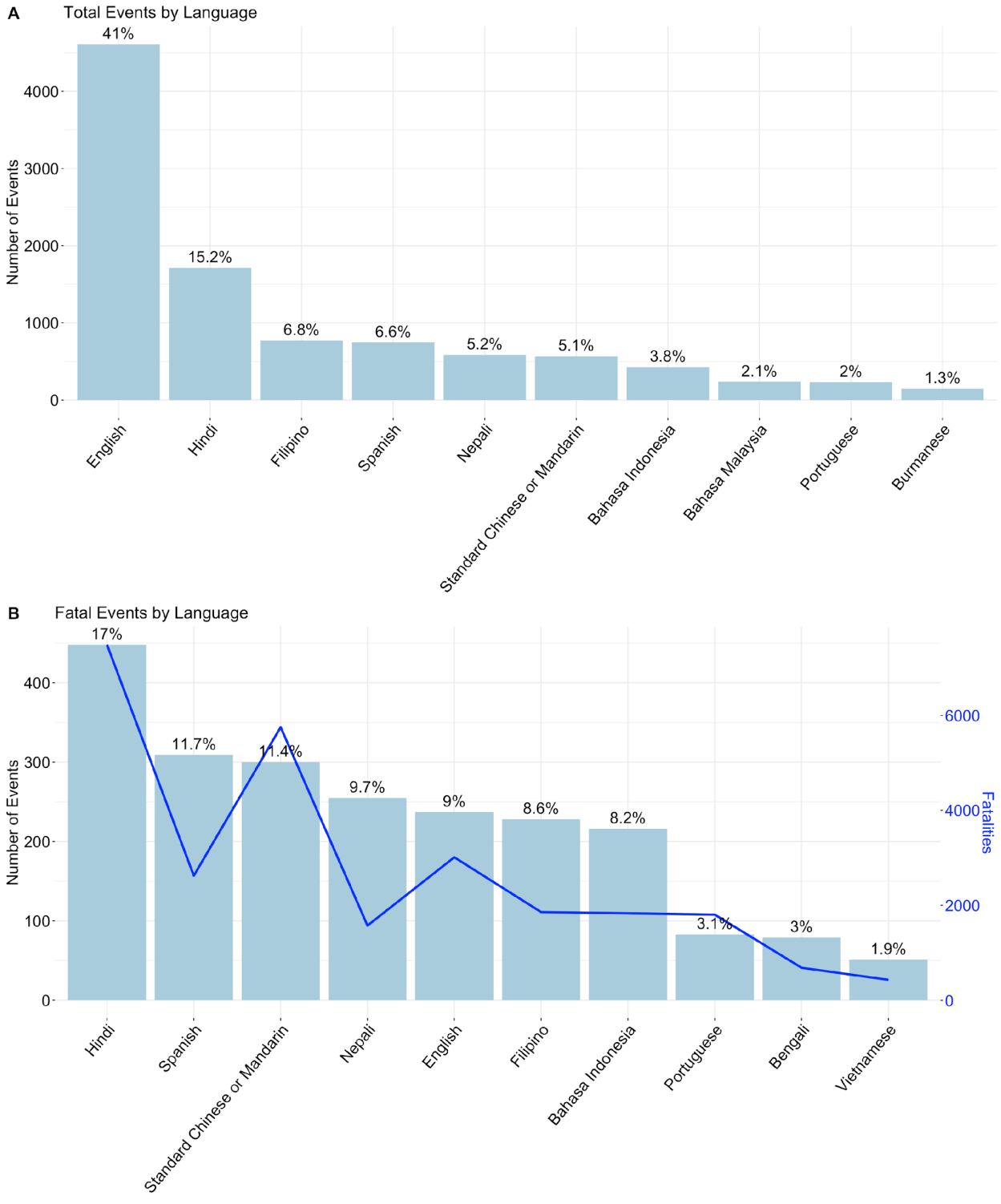

Figure 4.3. (A) Total number and percentage of total events by language; (B) Number of fatal events, percentage of total events, and number of fatalities by language.

4.3.3. Attribute Assessment

A general assessment of the GLC event attribute information is performed to observe trends in the event data. The known versus unknown values of several important attributes that are reported for each event are compared. The landslide category, location accuracy, size, and triggering mechanism attributes were mostly complete with known values for 90% or greater of reported events. However, the event time and landslide setting attributes were reported with more unknown values than known. Over 50% of events in the GLC are known within a five kilometer radius of confidence as shown in Table 4.2. Only 6.8% of events did not report a radius of confidence, and less than 20% of events have a radius of confidence greater than 25 km. This shows that generally, the location of the landslide reported from GLC events is relatively known within a small radius. The location accuracy is beneficial when using the GLC events for application in model training or validation. Furthermore, the distribution of the event size reported in the GLC is evaluated and the results are displayed in Table 4.3., which shows 72% of GLC events as medium size, and less than 9% of events are classified as large or very large. As the GLC is a collection of rainfall-triggered landslide events, we evaluated the triggering mechanism reported for each event. The distribution of triggering mechanisms are shown in Table 4.4., and 83% of events from 2007 to 2018 are in response to some type of precipitation. This attribute can be used to filter events for rainfall-triggered landslide studies that implement the use of the GLC. The reported events in the GLC per year are assessed and a cumulative sum per year is shown in Figure 4.4. The first three years on record, 2007–2009, consist of less reported events compared to later years, which could indicate that the first several years of landslide event collection are incomplete. The cumulative sum was also assessed by continent and similarly showed fewer reports for the first few years of record. No other regional patterns were discernible from the annual analysis. Furthermore, the reporting of events in the GLC by day of the week per year was evaluated in this study, and no distinct pattern was observed. The year 2010 holds the highest number of landslide events, and as mentioned, this anomaly year has been investigated and justified by extreme and prolonged precipitation in several landslide prone regions by Kirschbaum et al. (2012) [8]. This year also experienced greater numbers of fatal landslides and fatalities associated with landslides.

Table 4.2. Distribution of the radius of confidence of the reported location for all events.

Location Accuracy	Number of Events	Percentage of Total Events (%)
Exact	1386	12.7
1 km	2185	19.8
5 km	3178	28.8
10 km	1435	13.0
25 km	1470	13.3
50 km	794	7.2
100 km	25	0.2
250 km	16	0.1
Unknown	542	4.8

Table 4.3. Distribution of reported landslide size for all events.

Size	Number of Events	Percentage of Total Events (%)
Small	3199	28.2
Medium	6880	60.7
Large	900	7.9
Very large	118	1.0
Catastrophic	8	0.1
Unknown	229	2.0

Table 4.4. Distribution of triggering mechanism for reported events in the GLC.

Triggering Mechanism	Number of Events	Percentage of Total Events (%)
downpour	4836	42.68
rain	2874	25.3
unknown	1174	10.36
continuous rain	839	7.41
tropical cyclone	601	5.30
monsoon	245	2.16
snowfall snowmelt	155	1.37
mining	117	1.03
construction	102	0.90
earthquake	99	0.87
flooding	92	0.81
no apparent trigger	73	0.64
freeze–thaw	41	0.36
other	41	0.36
dam embankment collapse	19	0.17
Leaking pipe	17	0.15
volcano	4	0.04
vibration	1	0.01

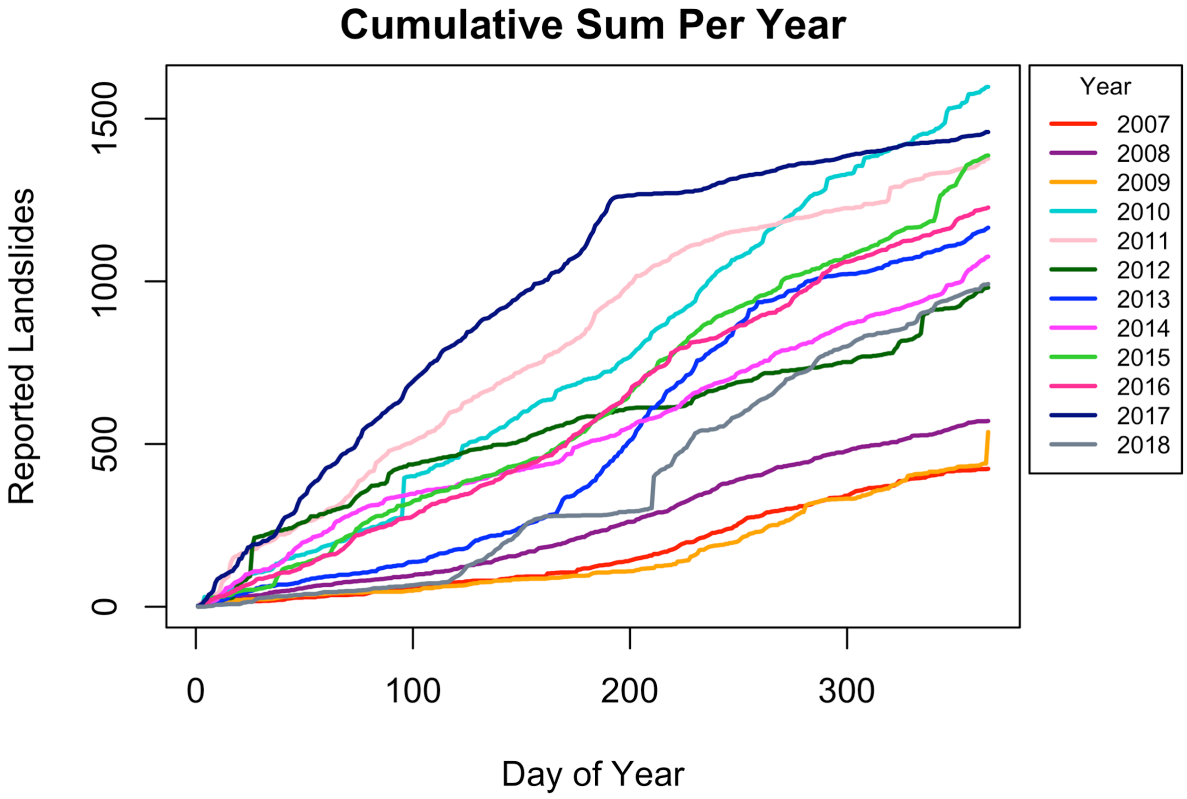

Figure 4.4. The cumulative sum of reported events in the GLC for each year from 2007 to 2018.

4.3.4. Inventory Comparison

There are landslide inventories available at global scale as well as focused on individual countries or states. These inventories vary in terms of source, mapping method, and attribute information. To compare the GLC against other landslide inventories, we look at several region-specific inventory databases and their similarities and differences against the GLC methodology. The location, number of points in the inventory, rainfall event date, number of points represented in the GLC, and source of each inventory are shown in Table 4.5. Only 9 out of the 27 event inventories are represented in the GLC by at least one point. A total of 25 points in the GLC coincide with the extent of the event inventories, which collectively report 17,893 landslides. One small, twelve medium, eight large, and four very large landslides represent the sizes reported by the GLC points and are shown in the reported size column in Table 4.5. Additionally, the location accuracy reported by the GLC was evaluated using the event inventories and are reported in the

location accuracy column of Table 4.5. Of the 25 points, 22 contained event inventory landslides reported within the location accuracy radius, 3 were near the landslide inventory area but exceeded the reported location accuracy radius, and 1 GLC point that was 5 km from the event inventory reported the location as unknown. These event inventories consist of between 131 and 21,379 points or polygons, and the GLC consists of at most 16 points for the corresponding event in Teresópolis, Brazil, which provides 7268 landslide polygons. Additionally, we compared the GLC events to a local landslide inventory from Vennari et al. (2022) for the Apulian region of southern Italy collected from 2008 to 2016. We found that no landslides are reported in the GLC in the extent of the Apulian region, while the local inventory reports 107 landslide points. While the GLC does not provide as many points as the event inventories evaluated here, one point in the GLC could be representative of all the landslide activity in that region for the specific event. However, the number of landslides represented in event inventories is up to several orders of magnitude greater than the number of reported landslides in the GLC for the same date and location as the landslide event mapped. This comparison shows that the GLC is less representative of small regions and event-specific landslides. Of the 19 inventories mapped in the Lower Mekong region, only five are represented in the GLC by one point, and one is represented by two points. This landslide inventories are mapped in primarily forested mountainous areas and the lack of representation in the GLC indicates that events occurring in remote locations are largely underreported.

Table 4.5. Rainfall-induced landslide event inventories used in this study.

Location	Number of Points	Rainfall Event Date	Points in GLC	Size	Location Accuracy	Source
Khao Phanom, Thailand	225	30 March 2011	2	Large (1) Medium (1)	5 km (2)	[17]
Falam, Myanmar	5086	30–31 July 2015	1	Medium	5 km	[17]
Hakha, Myanmar	1737	30–31 July 2015	1	Small	5 km	[17]
Thaphabath, Laos	242	11 September 2015	0			[17]
Mu Chang Chai, Vietnam	1256	2–3 August 2017	0			[17]

Muong La, Vietnam	758	2–3 August 2017	0			[17]
Bat Xat, Vietnam	99	23–28 August 2017	1	Large	25 km	[17]
Da Bac, Vietnam	1086	10–11 October 2017	1	Large	5 km	[17]
Phu Yen, Vietnam	1368	10–11 October 2017	0			[17]
Tram Tau, Vietnam	1490	10–11 October 2017	0			[17]
Sin Ho, Vietnam	707	23–24 June 2018	0			[17]
Tam Duong, Vietnam	159	23–24 June 2018	0			[17]
Than Uyen, Vietnam	312	23–24 June 2018	0			[17]
Vi Xuyen, Vietnam	157	23–24 June 2018	0			[17]
Hpa-An, Myanmar	992	28–30 July 2018	0			[17]
Phong Tho, Vietnam	302	3 August 2018	0			[17]
Xieng Ngeun, Laos	1178	30 August 2018	0			[17]
Muong Lat, Vietnam	1718	27 August – 1 September 2018	0			[17]
Nha Trang, Vietnam	207	18 November 2018	1	Medium	5 km	[17]
Blumenau, Brazil	597	20–25 November 2008	0			[18]
Teresópolis, Brazil	7268	11–13 January 2011	16	Medium (8) Large (4) Very Large (4)	1 km (1) 5 km (9) 10 km (6)	[18]
Salgar, Colombia	131	17–18 May 2015	0			[18]
Dominica	1756	25–28 August 2015	1	Large	5 km	[38]
Dominica	21,379	18–22 September 2017	0			[38]
Kii Province, Japan	1901	2–5 September 2011	0			[18]
South Taiwan	429	15–18 July 2008	1	Medium	10 km	[18, 37]
Taiwan	10,236	6–9 August 2008	0			[18, 36–37]

4.3.5. Economic Status Assessment

Economic variables are compared against landslide activity reported in the GLC to determine the effect of a country's economic status on landslide event reporting. The income status of each country is classified as low, lower middle, upper middle, or high and compared against the number of reported landslide events as well as landslide density. The landslide density is determined by the number of events in the GLC per land area of each country. The comparisons are shown in Figure 4.5.A,B, respectively. The largest percentage of events (40.8%) was reported in lower middle income status countries, which is slightly higher than the percentage of events reported in high income status countries (39.9%), and interestingly, only 18.1% of events were reported in countries associated with upper middle income status (Figure 4.5.A). In both income status comparisons with number of events and landslide density, countries considered to have low income status represent much less landslide activity (less than 2%) compared to higher income statuses. However, countries classified as having high income status experienced greater landslide density than countries with lesser income statuses, and an increase in landslide density with increasing economic status is apparent in Figure 4.5.B. Furthermore, the gross domestic product (GDP) per capita is compared against landslide event density for countries represented in the GLC and is shown in Figure 4.6., which reveals a positive correlation between the two variables. The countries shown represent the top 25% of countries with the highest GDP per capita to highlight outliers within the comparison. A log transformation of the data was used for better visualization. Similarly, the population density of each country represented in the GLC is compared against landslide density in Figure 4.7. This comparison reveals a positive correlation between population density and landslide reporting, which can be explained by increased landslide exposure near dense populations. However, the trend of increased GLC events in wealthier or more populated countries suggests that more landslides are reported but does not necessarily indicate that more landslide events occur in these countries.

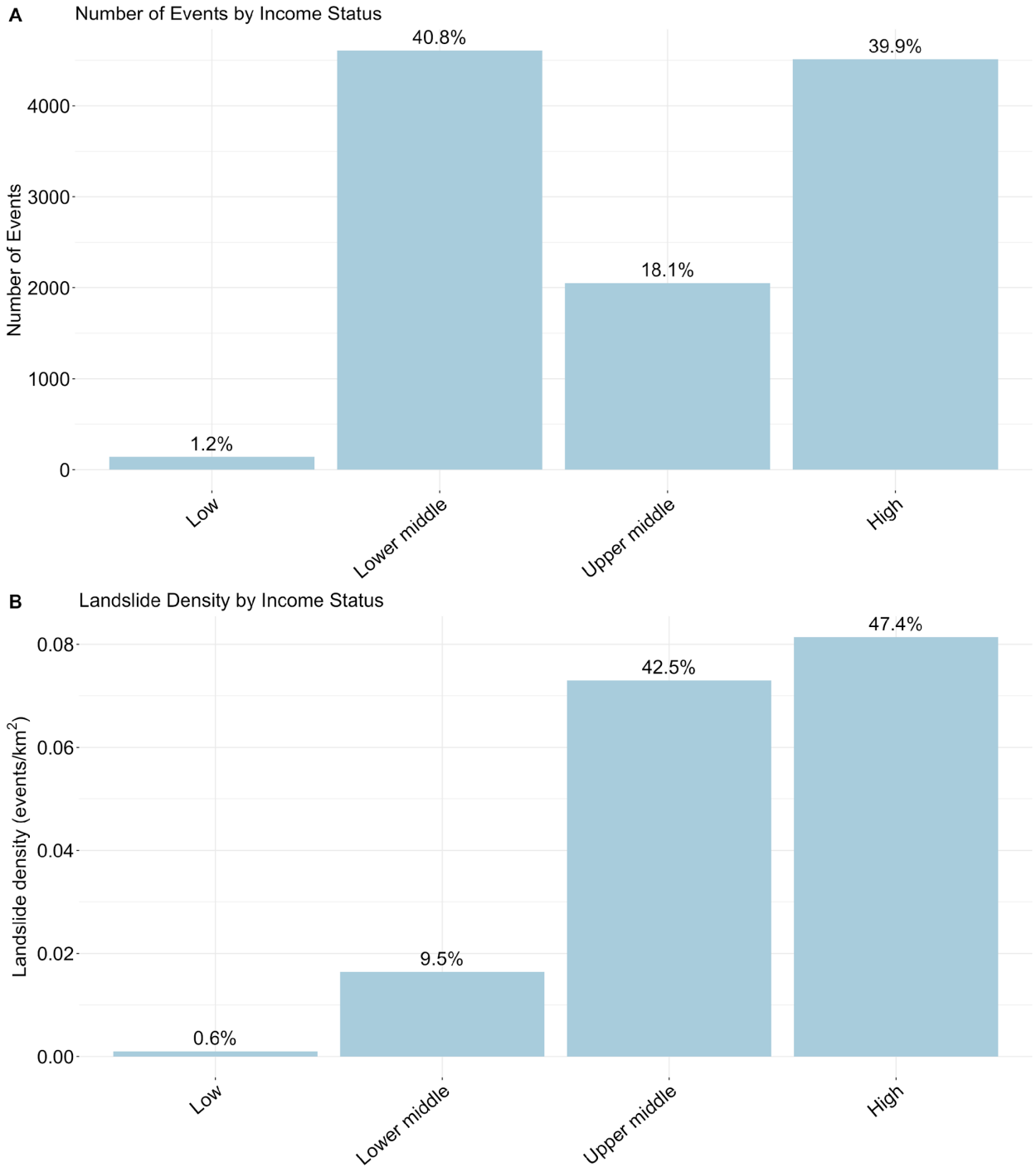

Figure 4.5. (A) Total reported events per income status classification; (B) Landslide density (events per km^2) per income status classification. The income status represents the reported income status of each country represented in the GLC.

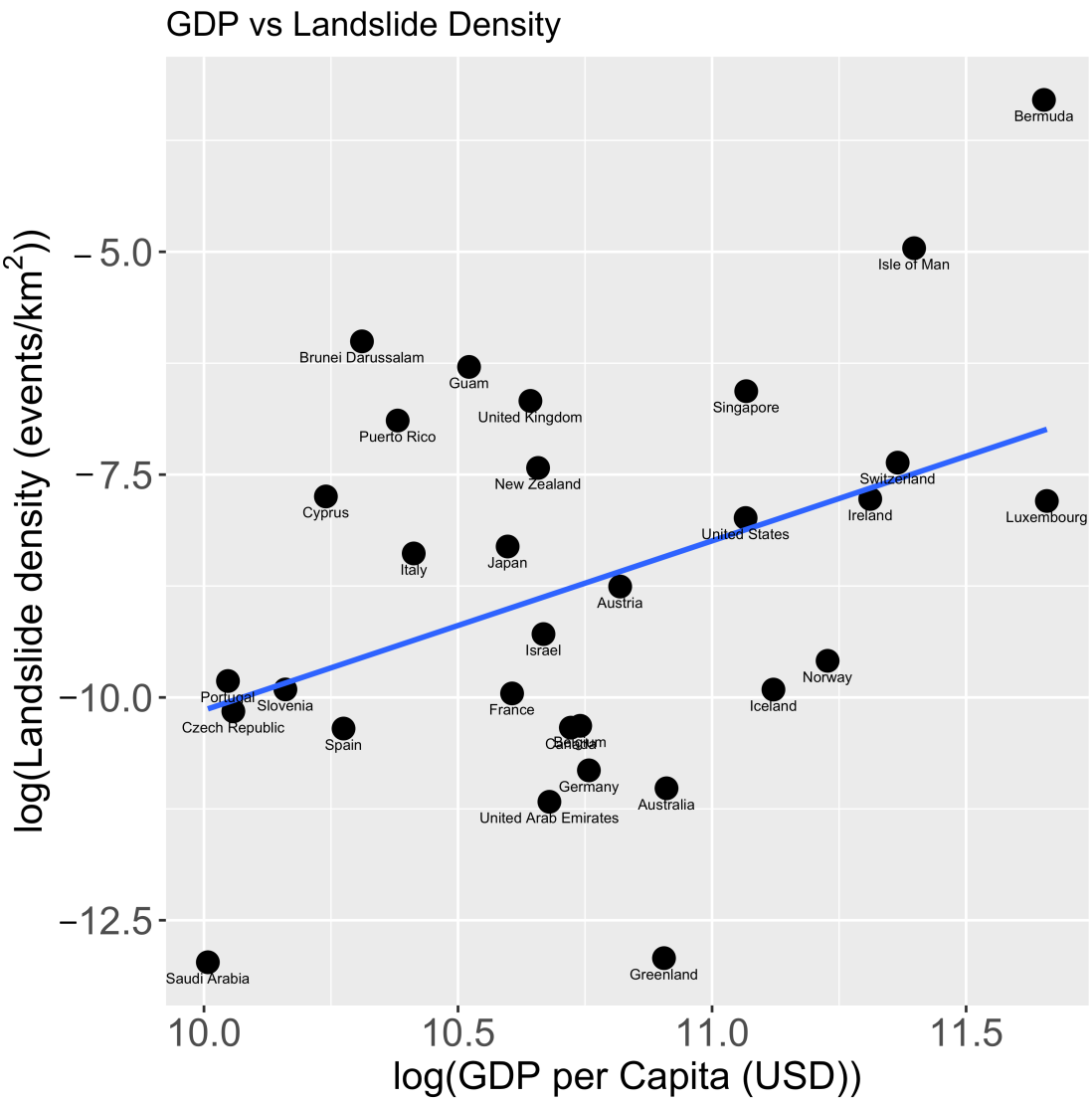

Figure 4.6. The log of the Gross Domestic Product (GDP) per capita in US dollars versus the log of the landslide density (events per km^2) for countries reported in the GLC with the highest reported GDP per capita.

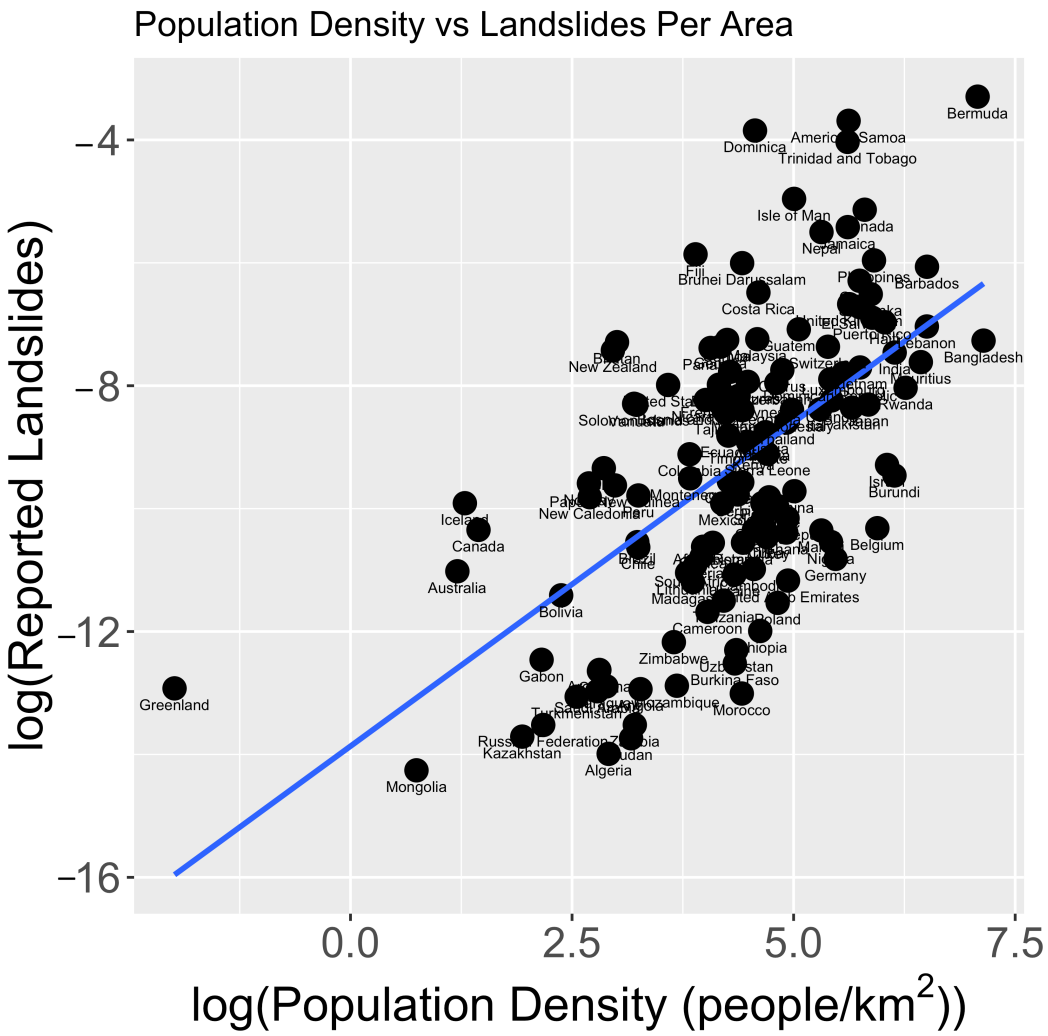

Figure 4.7. The log of the Population density (people per km²) versus the log of the landslide density (events per km²) for each country reported in the GLC.

4.4. Discussion

This study evaluates the spatial and temporal distribution of global landslide events and global patterns of landslides represented in this dataset including hotspot location and investigation of fatalities associated with landslides. The most notable landslide event hotspots at global scale appear to be in the Pacific Northwest, High Mountain Asia, and the Philippines as reported in the GLC. The GLC contains several outlier events that lead to large spikes in the data trend lines representing fatalities and number of events per month (Figures 1C–7C). For example,

the average number of fatalities in August for the continent of Africa is 133, almost twice as high as any other month (Figure 4.2.C). The large number of August fatalities can be attributed to one outlier event that occurred during this month and reported 1141 fatalities. Similar spikes in fatalities can be seen in other geographic locations due to anomaly events with large fatality counts. While the accuracy of these descriptors is not analyzed in depth, important attributes such as landslide category, location accuracy, landslide size, and triggering mechanism reported with each landslide event were assessed and found mostly complete, which further supports the application of the GLC in rainfall-triggered landslide studies. Furthermore, the most landslide events were reported in English-speaking countries, but the most fatal landslide events were reported in India, China, and Nepal. This indicates a clear reporting bias in the GLC towards English-speaking countries.

A positive correlation was discovered between the economic status of countries and the landslide density present in that country's borders, which indicates that richer countries are more prone to reporting landslides than poorer regions with less available resources. Countries with higher economic status have advanced natural disaster mitigation and more detailed landslide recording than low-income countries with less effort to prevent landslide disasters. This does not indicate that low-income countries have fewer landslides within their borders than high-income countries, but landslide events are reported more often and more precisely. Similarly, a positive relationship was found between population density and landslide reporting, which indicates that more landslides are reported in populated areas versus remote locations. Landslides are more likely to be reported in populated locations rather than remote areas due to greater risk of economic damage and casualties. These biases should be considered when applying the GLC. While the GLC shows a level of bias in regards to reporting language and underrepresentation of landslide activity in certain regions, it still can be beneficial for rainfall-triggered landslide research including landslide prediction and hazard awareness.

4.5. Conclusions

The research presented here evaluates the spatial and temporal distribution of global rainfall-triggered landslide reporting using NASA's Global Landslide Catalog (GLC), which presents a

minimum number of events and is recorded from 2007 to 2018. The collection of this dataset is no longer active and will not be updated past 2018. However, the GLC covers one of the largest spatiotemporal ranges of any landslide inventory. Hotspot analysis of global landslide reports and fatalities associated with landslides as well as temporal trends in reporting can be visualized using the GLC and show that most landslides occur in High Mountain Asia and the Pacific Northwest and more landslides occur globally from July to September. The majority of event locations reported in the GLC are known within a small radius of confidence and coincide with NASA's global landslide susceptibility map. The GLC also contains various attributes that describe each event in terms of size, impact, location, and casualties. However, the GLC has several limitations that should be considered when using this dataset. The GLC represents global landslides with less spatial precision than local landslide inventories and inventories mapped via image analysis. Outliers in fatalities associated with landslide events make it difficult to assess temporal trends in global landslide casualties. Additionally, landslide reporting is geographically biased towards English-speaking populations largely due to the method of compiling the GLC. Landslide reporting also occurs more regularly and consistently in areas with high economic status compared to low economic regions. Similarly, this study reveals greater landslide reporting in areas with high population density, which can be attributed to increased landslide exposure near dense populations. Despite its limitations and biases, the GLC is shown to be a useful tool for rainfall-triggered landslide research.

Chapter 5. Evaluation of Satellite-Based Soil Moisture Products for Landslide Monitoring

Associated citations:

(1) Dandridge, C.; Fang, B.; Lakshmi, V. Downscaling of SMAP Soil Moisture in the Lower Mekong River Basin. Water 2020, 12, 56. https://doi.org/10.3390/w12010056

(2) Dandridge, C.; Stanley, T.A.; Biswas, N. Kirschbaum, D.B.; Lakshmi, V. Evaluation of Satellite-Based Soil Moisture Products using the Landslide Hazard Assessment for Situational Awareness (LHASA) Model for Landslide Prediction and Hazard Analysis in the Lower Mekong River Basin, H42G-1378 iPoster at 2022 Fall Meeting, AGU, December 12-16.

This chapter is in preparation for submission to a peer-reviewed journal. The current co-authors are Thomas Stanly, Nishan Biswas, Dalia Kirschbaum, and Venkat Lakshmi.

5.1. Introduction

Soil moisture content affects the shear strength of a soil body and plays an important role in slope stability (Li et al., 2021). Changes in subsurface hydrological conditions such as increased pore water pressure after precipitation can result in slope failure and thus induce landslides (Whiteley et al., 2019). Obtaining soil moisture measurements can be achieved using a variety of remote sensing instruments or ground-based systems. In situ measurements can provide very accurate moisture information, but the cost of maintenance is high and usually the network is not dense enough for effective applications over large areas (Zhao et al., 2021) In large river basins where in situ data are limited or absent, satellite-based soil moisture estimates can be used to supplement ground measurements for land and water resource management solutions (Dandridge et al., 2020). Consistent soil moisture estimation can aid in monitoring droughts, forecasting floods, monitoring crop productivity, and natural hazard monitoring. Satellite-based radars can measure soil moisture at high resolution but are limited in spatial coverage and temporal frequency (Dandridge et al., 2020). Recent advances in available soil moisture products are able to provide high resolution soil moisture estimates that can be applied directly to improve landslide hazard mitigation. Unfortunately, the LMRB does not have a consistent in situ soil moisture measuring system, which makes satellite-derived soil moisture estimates appealing for application in watershed-scale hydrological modelling in this region. However, the lack of ground measurements for soil moisture also complicates validation of remotely-sensed estimates

over the LMRB (Naeimi et al., 2013). This study compares the applicability of four satellite-based soil moisture products available over the LMRB to assess how soil moisture products can be used for landslide hazard assessment and to estimate landslide susceptibility. These products vary by not only spatial and temporal resolution, but assimilation methodology and depth of the soil profile estimated. By comparing these products, we can gain better insights into the relationship between satellite and modelled soil moisture and landslide hazard in the LMRB.

There have been several attempts at landslide prediction at regional (Wilkinson et al., 2002; Ponziani et al., 2012; Luo et al., 2016) and global scale (Farahmand & AghaKouchak, 2013; Stanley et al., 2021). Biswas et al., (2021) successfully implemented a version of the LHASA model in the LMRB. The model was able to capture the seasonal variability of the region with low probabilities during the dry season with low seasonal rainfall and higher probabilities during the monsoon season. However, there is still a gap in the literature regarding comparisons of soil moisture products in the LMRB and their applications in landslide prediction and monitoring. The Landslide Hazard for Situational Awareness (LHASA) has been updated from version 1 to version 2 at global scale (Stanley et al., 2021). The updated structure utilizes an XGBoost machine learning framework, a methodology that is now widely used for landslide applications. With the innovative model framework, LHASA version 2 was found to be able to predict historical landslides twice as much as version 1. The full methodology behind LHASA is described in Stanley et al., 2021. Due to the successful performance of this methodology in the literature, and its application in the global LHASA model, the XGBoost framework was selected for this research study to predict landslide potential using a similar framework to the global model but catered to the LMRB region. This research aims to further reveal the ability of machine learning to provide enhanced landslide prediction.

5.2. Data

5.2.1. Landslide Inventory

The landslide inventories used in this study were mapped by Amatya et al., (2021) using the Semi-Automatic Landslide Detection (SALaD) system and high resolution satellite imagery from Planet. This framework uses object-based image analysis of pre- and post-event imagery to

detect landslides. A total of 22 inventories (2 in Laos, 4 in Myanmar, 1 in Thailand, and 15 in Vietnam) from 2015 – 2020 were used in the training and validation of the models presented here. Of these inventories, 19 were mapped from 2015-2019 and used for training the models, and three inventories were mapped in 2020 and used for validation of the models.

5.2.2. CFS Soil Moisture

The Climate Forecast System (CFS) version 2 soil moisture is derived from a fully coupled land-atmosphere-ocean model representative of Earth's land and atmosphere interactions (Saha et al., 2011). This data was developed in March 2011 by the National Centers for Environmental Prediction (NCEP). The spatial resolution of this product is 0.25° x 0.25 ° (approximately 27 km x 27 km), and the temporal resolution is 6-hourly. This product represents the volumetric soil moisture content from 0 to 150 cm below the surface layer. For a full description of the methodology please refer to Saha et al., (2011). CFS soil moisture was selected in this study as it has been implemented successfully in the LMRB by Biswas et al., (2022). This product was selected for their study due to its public availability, minimized lag time, and accessibility in Google Earth Engine. It is used in this study to determine if current modelling efforts could be improved using various soil moisture products for comparison.

5.2.3. SMAP Soil Moisture

The Soil Moisture Active Passive (SMAP) was launched in January 2015 with the goal of combining radar and radiometer at L-band frequencies to record high resolution soil moisture measurements and freeze/thaw detection at global scale (Entekhabi et al., 2010). Unfortunately, shortly after the launch a hardware failure caused the radar to stop working, leaving the radiometer as the only operational mechanism to record data (Chan et al., 2018). SMAP uses lower frequency microwave radiometry (L Band) to map soil moisture at Earth's land surface because at lower frequencies the atmosphere is less opaque, vegetation is more transparent, and the results were more representative of the soil below the skin surface than when higher frequencies were used (Panciera et al., 2013; Colliander et al., 2017). The product used in this study is the SMAP L4 Global 3-hourly 9 km EASE-Grid Surface and Root Zone Soil Moisture Geophysical Data version 7, which uses SMAP L-band brightness temperature for data assimilation in a land surface model. Data is available from 2015 to present with a spatial resolution of 9 km x 9 km and

3-hourly temporal resolution. This product represents the volumetric soil moisture content from 0 to 100 cm below the surface layer. For a full description of the methodology please refer to Reichle et al., (2022). SMAP L4 was selected due to it being one of the most recent efforts to estimate global soil moisture via remote sensing and is currently being used in the operational global version of LHASA.

5.2.4. RHEAS Soil Moisture

The Regional Hydrologic Extremes Assessment System (RHEAS) is a software framework designed for hydrologic modeling and data assimilation. The RHEAS framework is used to assimilate soil moisture and other variables for the entire LMRB for applications by the Mekong River Commission for drought and agricultural monitoring at https://mdcw-servir.adpc.net. This product was developed under the SERVIR-Mekong program by the Asian Disaster Preparedness Center (ADPC), NASA Jet Propulsion Laboratory, and local technical partners in the LMRB. RHEAS utilizes a software framework for hydrologic modeling and data assimilation that automates the deployment of water resources nowcasting and forecasting applications (MDCW, 2020). Its methodology uses multiple satellite-based products for data assimilation, including precipitation, soil moisture, evapotranspiration, and vegetation indices. The spatial resolution of this dataset is 5 km x 5 km at daily temporal resolution. This product represents the volumetric soil moisture content from 0 to 10 cm below the surface layer. For a full description of the methodology please refer to Andreadis et al., (2017). This product was selected due to it being assimilated by local agencies in the LMRB and is readily available for use in the LMRB.

5.2.5. UVA Soil Moisture

The University of Virginia (UVA) 1 km SMAP Downscaled Soil Moisture was developed by Fang et al., (2022) and is based on thermal inertia theory. The algorithm uses the relationship between soil moisture and temperature difference which was determined using outputs from the Global Land Data Assimilation System–Noah (GLDAS) Land Surface Model and the Advanced Very High Resolution Radiometer Normalized Difference Vegetation Index (NDVI) data and then applied to the Aqua Moderate Resolution Imaging Spectroradiometer land surface temperature/NDVI data to produce a downscaled 1-km daily SM product, at 6:00 a.m. and 6:00 p.m. at global scale from 2015 to 2020. This algorithm uses soil moisture estimates from SMAP L2

9 km radiometer product. Validation attempts of this product have been performed using various in situ networks from the International Soil Moisture Network (ISMN) and results indicate that the 1 km downscaled product is more accurate than 9 km SMAP data (Fang et al., 2022). For a full description of the methodology please refer to Fang et al., (2022). This product was selected as it has yet to be applied in a landslide hazard assessment or landslide prediction study in existing literature and data availability.

5.2.6. IMERG Precipitation

The Global Precipitation Measurement (GPM) satellite provided Integrated Multi-satellitE Retrievals for GPM (IMERG) version 6 product uses an algorithm that provides rainfall estimates by combining data from microwave and infrared instruments and uses precipitation gauge data for calibration (Huffman et al., 2019). The spatial resolution of this product is 0.1° x 0.1° (approximately 10 km x 10 km) at half-hourly temporal resolution. In this study, the precipitation is converted into a 3-day accumulated rainfall estimate (mm) and from the 3-day accumulations, the 99th percentile of accumulated precipitation is estimated (mm). IMERG was selected for precipitation data due to its current usage in the operational global version of LHASA as well as its data availability from 2000-present. Information regarding the dynamic variables used in this study are shown in Table 5.1.

Table 5.1. Description of dynamic variables used in this study.

Data Product	**Description***	**Source**
Climate Forecast System (CFS) Soil Moisture V2	0 – 150 cm 0.25° 6-hourly	Saha, S., Moorthi, S., Wu, X., Wang, J., Nadiga, S., Tripp, P., Behringer, D., Hou, Y. T., Chuang, H. Y., Iredell, M., Ek, M., Meng, J., Yang, R., Mendez, M. P., Van Den Dool, H., Zhang, Q., Wang, W., Chen, M., & Becker, E. (2014). The NCEP climate forecast system version 2. Journal of Climate, 27(6), 2185–2208. https://doi.org/10.1175/JCLI-D-12-00823.1

Soil Moisture Active Passive (SMAP) L4	0 – 100 cm 9 km 3-hourly	Reichle, R., G. De Lannoy, R. D. Koster, W. T. Crow, J. S. Kimball, Q. Liu, and M. Bechtold. (2022). SMAP L4 Global 3-hourly 9 km EASE-Grid Surface and Root Zone Soil Moisture Geophysical Data, Version 7 [SPL4SMGP]. Boulder, Colorado USA. NASA National Snow and Ice Data Center Distributed Active Archive Center.
Regional Hydrologic Extremes Assessment System (RHEAS) Soil Moisture	0 – 10 cm 5 km Daily	Mekong Drought and Crop Watch (MDCW), (2020), ADPC/SERVIR Mekong, https://mdcw-servir.adpc.net
University of Virginia (UVA) 1 km SMAP Downscaled Soil Moisture	0 – 5 cm 1 km Twice-daily	Fang, B., Lakshmi, V., Cosh, M., Liu, P. W., Bindlish, R., & Jackson, T. J. (2022). A global 1-km downscaled SMAP soil moisture product based on thermal inertia theory. Vadose Zone Journal, 21(2). https://doi.org/10.1002/vzj2.20182
Global Precipitation Measurement satellite provided Integrated Multi-satellitE Retrievals for GPM (IMERG) Precipitation V6	0.1° Half-hourly	Huffman, G.J., E.F. Stocker, D.T. Bolvin, E.J. Nelkin, Jackson Tan (2019), GPM IMERG Final Precipitation L3 Half Hourly 0.1 degree x 0.1 degree V06, Greenbelt, MD, Goddard Earth Sciences Data and Information Services Center (GES DISC), Accessed: [Data Access Date], doi:10.5067/GPM/IMERG/3B-HH/06

*Description includes depth, spatial resolution, and temporal frequency for soil moisture products and spatial resolution and temporal frequency for the precipitation product.

5.2.7. Static Variables

Several static variables were used in this study alongside the dynamic products for soil moisture and precipitation. These static variables include distance to faults, lithology, slope, relief, topographic wetness index (TWI), distance to rivers, distance to roads, and forest loss. These variables are held constant as they are assumed to change very slowly over time unlike precipitation and soil moisture conditions. Information regarding the sources of the static variables can be found in Table 5.2.

Table 5.2. Static variables and their data sources used in this study

Variable	Source
Distance to Faults	Styron, R., & Pagani, M. (2020). "The GEM Global Active Faults Database." *Earthquake Spectra*, vol. 36, no. 1_suppl, pp. 160–180.
Lithology	Hartmann, J., & Moosdorf, N. (2012). The new global lithological map database GLiM: A representation of rock properties at the Earth surface. Geochemistry, Geophysics, Geosystems, 13(12).
Slope Relief Topographic Wetness Index (TWI)	Farr, T. G., & M. Kobrick, (2000). Shuttle Radar Topography Mission produces a wealth of data. Eos Trans. AGU, 81:583-583.
Distance to Rivers	Lehner, B., & Grill G. (2013). Global river hydrography and network routing: baseline data and new approaches to study the world's large river systems. Hydrological Processes, 27(15): 2171–2186.
Distance to Roads	Meijer, J. R., Huijbregts, M. A. J., Schotten, K. C. G. J., & Schipper, A. M. (2018). Global patterns of current and future road infrastructure. Environmental Research Letters, 13(6).
Forest Loss	Hansen, M. C., Potapov, P. V., Moore, R., Hancher, M., Turubanova, S. A., Tyukavina, A., Thau, D., Stehman, S. V., Goetz, S. J., Loveland, T. R., Kommareddy, A., Egorov, A., Chini, L., Justice, C. O., & Townshend, J. R. G. (2013). High-resolution global maps of 21st-century forest cover change. Science, 342(6160), 850–853.

5.3. Methodology

5.3.1. Precipitation Scaling

To normalize the precipitation data, the 99th percentile of 3-day accumulation is estimated from 2000-2020. The 99th percentile is used to represent extreme precipitation events. The log-normal distribution was then fitted to the 99th percentile precipitation as it fits remotely sensed rainfall well (Stanley et al., 2021). The fitted distribution is used to rescale the 3-day accumulated

precipitation, which is used to train the model framework (Biswas et al., 2022). Transforming using the log-normal distribution of extreme rainfall is often performed as it reduces skewness in the data distribution (Mohita Anand & Jai Bhagwan, 2010).

5.3.2. XGBoost Model

Two dynamic variables, precipitation and soil moisture, and eight static variables were incorporated in model training. A total of four models were trained varying only by the soil moisture product implemented in training and validation. The landslide inventory points from 2015 – 2019 were used for training and points from 2020 were used for validation of the model predictions. A ratio of 1:100 of landslide to non-landslide points was applied to avoid overfitting to landslide points during model training. A workflow diagram of the model methodology is shown in Figure 5.1. The XGBoost python library was utilized for training of the models as this machine learning approach is able to provide interaction and monotone constraints that are appropriate for landslide prediction (Biswas et al., 2022). The interaction constraints control the variables used in the same trees, and the monotone constraints determine which direction (positive or negative) the variables contribute to the predictions. Precipitation is the only variable allowed to interact with other variables during model training. The algorithm builds an ensemble of trees by creating a single tree at each iteration. Then, each subsequent tree corrects the deficiencies of the existing trees. These trees alone are considered "weak learners" as they are poorly predictive as individual trees but as a collective, they can be very effective. The algorithm was trained to detect binary (0 or 1) classification of presence or absence of landslides. The model parameters are defined in Table 5.3. Benefits of this machine learning methodology is that it has vast documentation and is accessible in multiple programming languages (Stanley et al., 2021).

Table 5.3. XGBoost model parameters

Model parameters	**Tuned value**
Maximum depth	2
Objective	Binary: logistic

Monotone constraints	Distance to Roads, Distance to Faults, Distance to rivers have inverse relationship, all others have a linear relationship
Interaction constraints	Only precipitation can interact with other variables

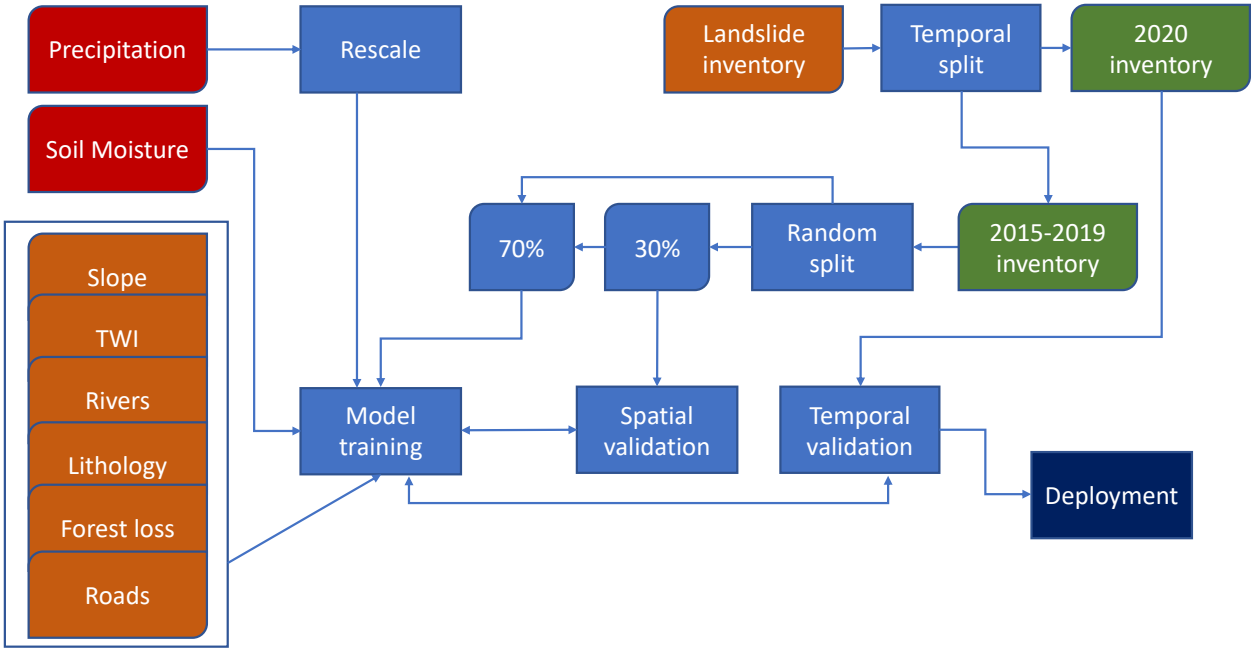

Figure 5.1. Workflow diagram for Landslide Hazard Assessment for Situational Awareness (LHASA) Model V2

5.3.3. Model Validation

The three event-based landslide inventories from 2020 were used for model validation. These landslide events occurred on October 12, October 18, and October 28. The prediction from each model on the day of the event was extracted at each landslide point. If the probability is higher than the threshold, it is considered a true positive, and if it is lower than the threshold, it is considered a false negative. From the true positives and false negatives, we can derive a true positive rate (TPR) by Equation 5.1.

$$\mathrm{TPR} = \frac{\text{true positives}}{\text{true positives} + \text{false negatives}} \qquad \text{(Equation 5.1)}$$

5.4. Results

The completeness of each soil moisture product was examined to determine the presence and extent of any potential data gaps. The missing values present in each dataset were calculated and shown in Figure 5.2. The UVA 1 km soil moisture data consisted of spatial and temporal variability in its daily estimates due to cloud contamination and the temporal variability in the overpasses of the satellite platforms. The percentage of missing pixel coverage ranged from 0.32% to 37.8%. Since the CFS, SMAP, and RHEAS products are all assimilated, they display no missing values. The RHEAS soil moisture pixels without estimates present were not considered as missing values as the number of missing pixels were consistent for each daily soil moisture profile estimate due to the product masking water bodies. To determine the ability of each soil moisture product to capture seasonal trends, the products are compared to rainfall estimates from IMERG with 0.1° spatial resolution at daily scale. The time series is shown in Figure 5.3 with precipitation represented in blue bars and the four soil moisture products represented below. The values represent daily soil moisture and precipitation averaged over the entire region from 2015 – 2020, the time period used for training (2015-2019) and validation (2020). Each of the soil moisture products were able to capture the seasonal trends present in precipitation, with higher values during the monsoon season and lower soil moisture during the dry season.

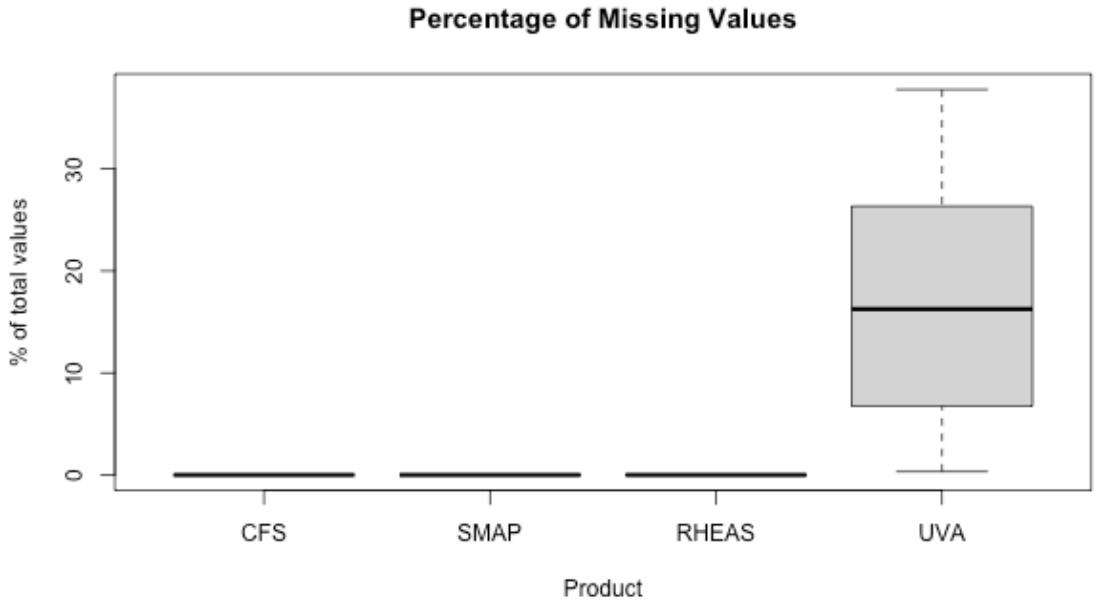

Figure 5.2. Boxplots showing the percentage of missing values in each product from 2015-2020.

As expected, the surface products, UVA and RHEAS, show higher variations in soil moisture values over time compared to the products estimating the total soil profile, CFS and SMAP. SMAP demonstrates lower soil moisture values than the other products all year but the difference is greater during the wet season. Overall, the soil moisture products used in this study are able to represent the seasonal patterns affected by precipitation over the LMRB.

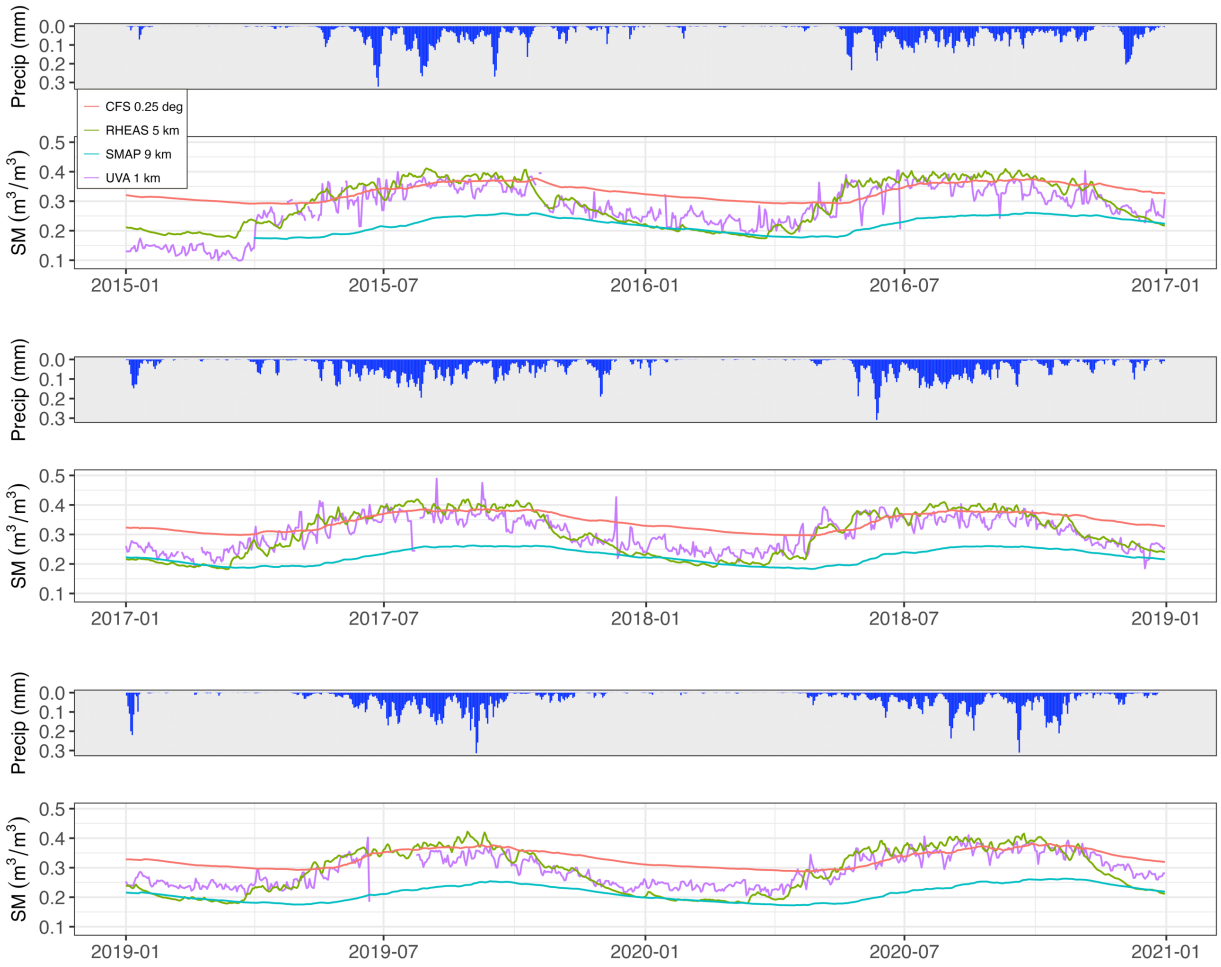

Figure 5.3. Time series of soil moisture products averaged over entire basin for 2015 – 2020.

Soil moisture at high resolution should show standard deviation ranges closer to in situ than coarser resolution soil moisture. The number of pixels, minimum, maximum, and standard deviation for the soil moisture profiles from each product over the area of a rainfall-triggered

landslide event on October 28, 2020 were determined and are shown in Table 5.3. The maximum values are much higher for RHEAS and UVA soil moisture than CFS and SMAP and this is most likely explained by the varying depths that the soil profiles are estimated, and UVA and RHEAS soil moisture estimating surface soil moisture within the top 5 or 10 cm, respectively. The standard deviation for the UVA 1 km soil moisture is greater than coarser resolution products, indicating it is better able to represent surface fluctuations more similar to in situ than the other products, which can also be explained by the greater number of pixels representing soil moisture estimates over the landslide area.

The soil moisture was examined alongside the occurrence of landslide events with the purpose of examining the drying of soil over time in response to a rainfall event. By evaluating the time series during a precipitation event triggering a landslide we are able to observe the near-surface soil moisture observations and whether they transition from saturated to dry conditions. However, it's important to note that surface soil moisture is more sensitive to rainfall than deeper soil layers, and a lag in soil moisture in response to rainfall at deeper layers (80-100 cm) may be present in the CFS or SMAP products (Dai et al., (2022). Figure 5.4. shows the time series comparison of the soil moisture estimates leading up to and immediately after the landslide event on October 28, 2020. The UVA 1 km soil moisture was interpolated to reduce data gaps and better observe dry down patterns centered around the landslide event date. Of all the products, RHEAS soil moisture was best able to capture the observed pattern typical of soil moisture during a landslide, however both RHEAS and UVA products indicate an increase in soil moisture prior to the landslide event. We expect a large increase in moisture right before or during the landslide and then a decrease in moisture content after the event. The CFS and SMAP products did not reflect any significant patterns and show little variation in soil moisture reflecting a rainfall-triggered landslide event. However, SMAP seems to capture the dry down pattern after the event represented by the peak in moisture conditions on October 31, 2020 followed by a dry down trend. The spatial resolution and variability of the daily soil moisture profiles from CFS, SMAP, RHEAS, and UVA for the same event are shown in Figure 5.5. Overall, the surface products better captured fluctuations in soil moisture due to precipitation that are present for the shallow landslide event on October 28, 2020 in Quang Nam, Vietnam.

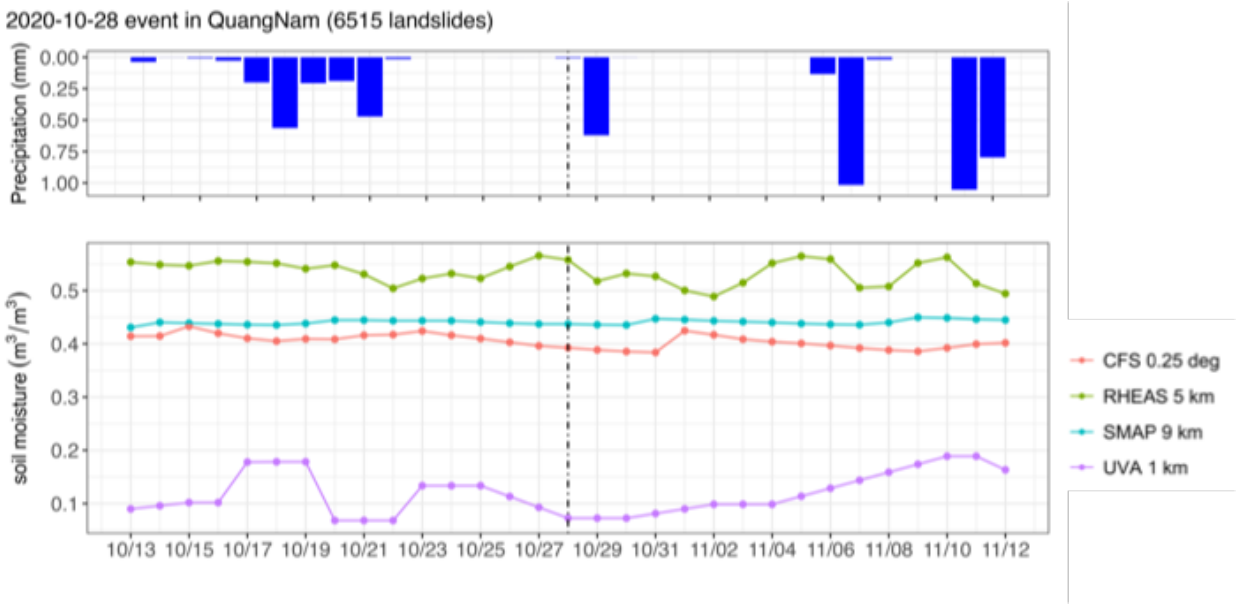

Figure 5.4. Time series of precipitation and soil moisture over landslide area in Quang Nam, Vietnam on 2020-10-28.

Table 5.3. Soil moisture product statistics for a landslide event on 2020-10-28

SM product	number of pixels	min	mean	max	standard deviation
CFS (0.25°)	12	0.390	0.393	0.394	0.001
SMAP (9 km)	40	0.430	0.437	0.441	0.003
RHEAS (5 km)	140	0.476	0.558	0.608	0.023
UVA (1 km)	4473	0.387	0.529	0.644	0.058

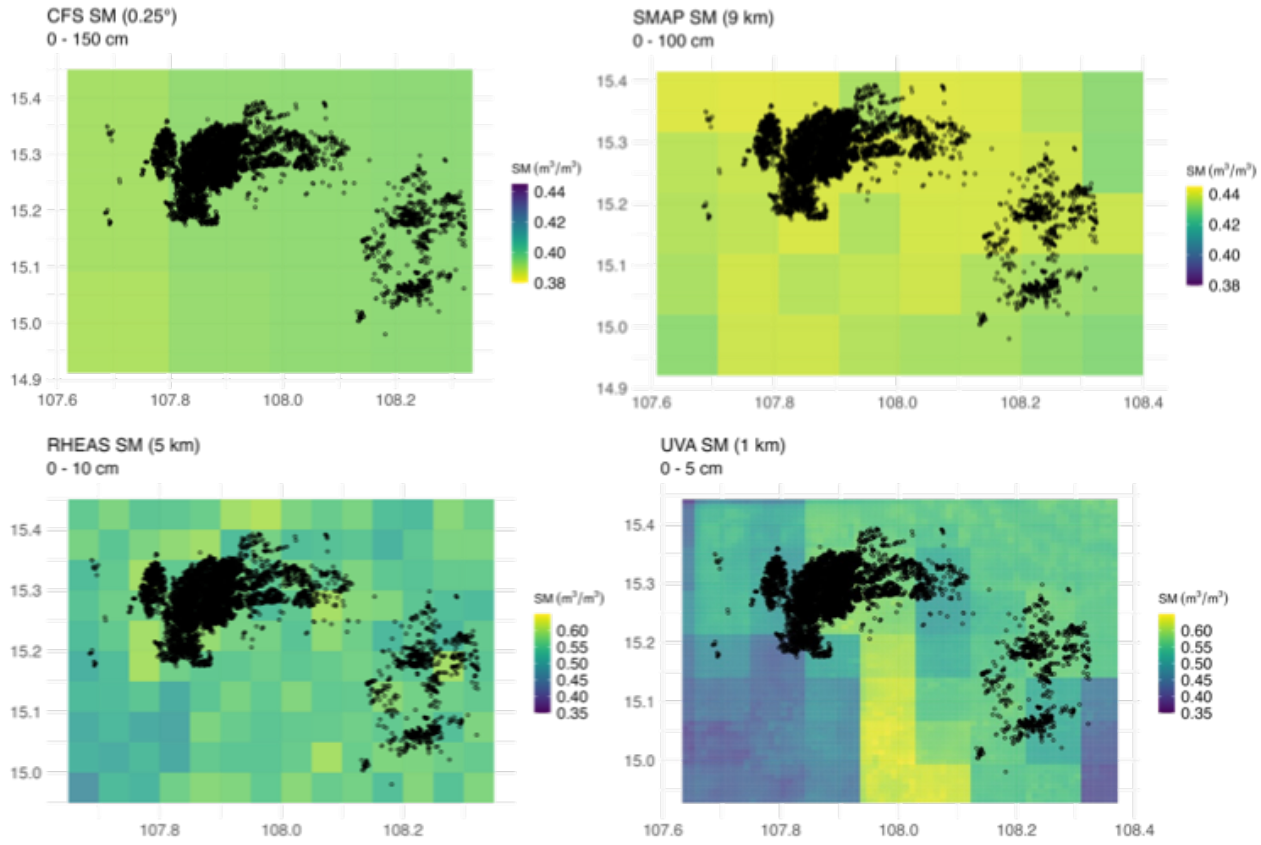

Figure 5.5. Spatial resolution and variability of the daily soil moisture profiles from CFS, SMAP, RHEAS, and UVA overlayed with landslide points from a landslide event on October 28, 2020.

SHAP (Shapley Additive Explanations) are commonly used to increase the interpretability of machine learning models. Figure 5.6. displays the SHAP values for each of the trained models using CFS, SMAP, RHEAS, and UVA soil moisture, respectively. Regarding the order of feature importance, models trained with CFS, SMAP, and RHEAS indicate soil moisture to be the second most important feature after precipitation. However the model trained with UVA data indicate slope and relief to both be more important than soil moisture. The SHAP plots display each feature value and its impact on the model output. For example, we would expect to see high values of precipitation and soil moisture to correlate with higher prediction estimates and lower values to produce a lower prediction estimate. Alternatively we expect to see variables such as distance to roads reduce prediction values as their values increase (i.e. the further a location is from a road, the less likely a landslide will occur in that location). All of the models found distance to rivers or forest loss to be the least important feature, meaning this variable did

not contribute to the model predictions compared to other variables used to train the models. The small differences in feature importance between models are to be expected as the only variation in model training is soil moisture.

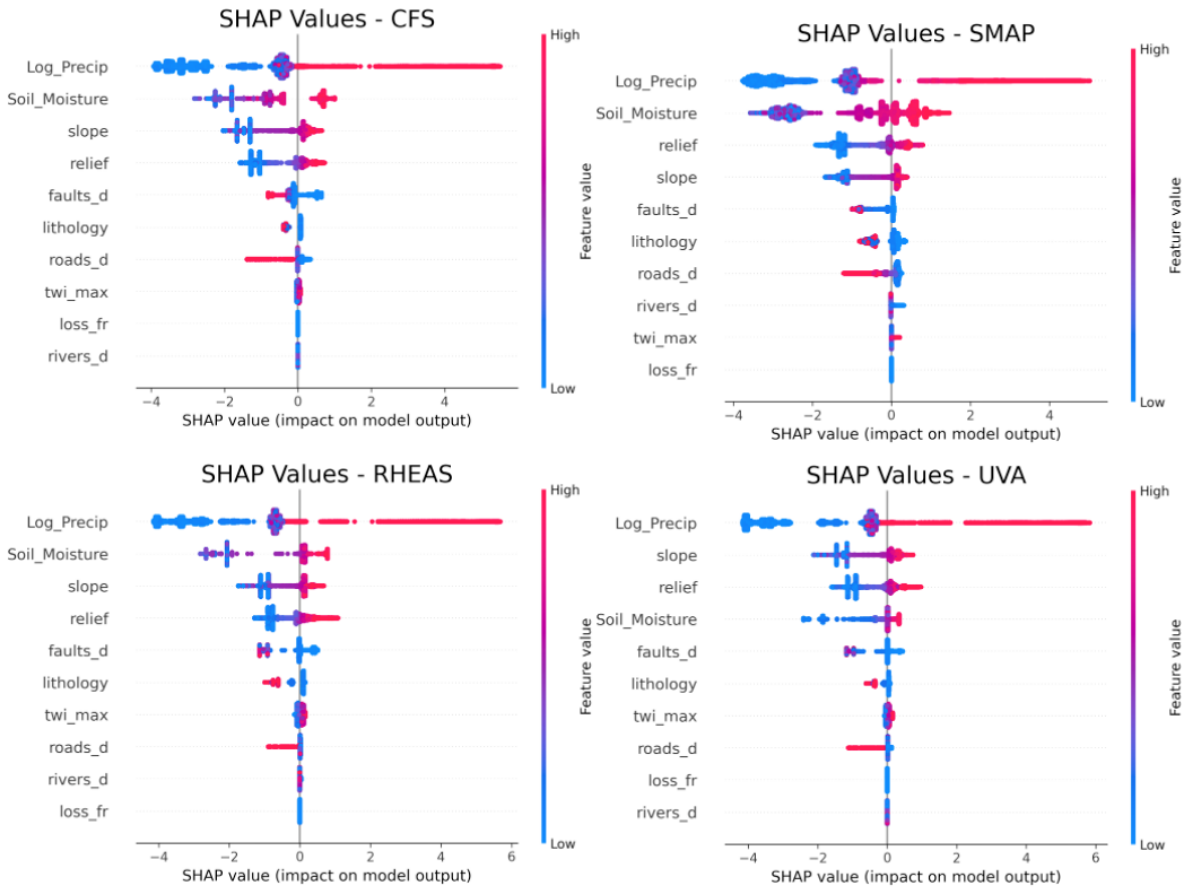

Figure 5.6. SHAP Values for each model trained with CFS, SMAP, RHEAS, and UVA soil moisture, respectively.

Table 5.4. shows the validation results for the three event inventories used for validation in 2020. The event on October 12, 2020 had 116 landslide points, the event October 18, 2020 had 1138 landslides, and the event on October 28, 2020 had 6515 landslide points for reference. The model with the UVA soil moisture data had the highest TPR on two dates, and RHEAS had the highest TPR for the event on October 18, 2020. Overall, the model trained with CFS performed the worst in terms of TPR. However, the results of this study indicate that the use of either of the

four of these soil moisture products could be useful for monitoring landslide hazard in the LMRB using the LHASA model based on the TPR. Higher resolution surface layer soil moisture is able to more closely resemble variations in moisture content for shallow landslides. However, considering moisture profiles that estimate soil conditions at deeper soil layers may be able to better represent the subsurface processes that contribute to slope failure and landslides deeper than the top few centimeters.

Table 5.4. True Positive Rates (TPR) % for each event inventory in 2020

	Soil Moisture Product			
Validation date	**CFS**	**SMAP**	**RHEAS**	**UVA**
10/12/20	TPR = 60.8	TPR = 93.9	TPR = 71.5	TPR = 95.7
10/18/20	TPR = 83.7	TPR = 86.8	TPR = 93.8	TPR = 92.3
10/28/20	TPR = 69.6	TPR = 60.1	TPR = 72.8	TPR = 78.0

5.5. Conclusions

In this study, four soil moisture products are compared in the LMRB and specifically there applicability for landslide monitoring are assessed. For two of these products, UVA 1 km soil moisture and RHEAS 5 km soil moisture this is a novel application of their effectiveness in landslide prediction. The UVA 1 km soil moisture was better able to capture dry down patterns regarding surface soil moisture, while RHEAS was better able to capture dry down patterns regarding total soil profile. High resolution soil moisture is better able to estimate antecedent soil moisture conditions than coarse resolution due to the relatively small area affected by a landslide. However, varying spatio-temporal availability limits the use of the UVA 1 km soil moisture due to inaccuracy of the model prediction where data gaps exist. In all models evaluated, low soil moisture conditions impacted landslide prediction in all models more so than high soil moisture values. The results of this research warrant a near-real time soil moisture product at 1 km that represents soil moisture and varying depths representing surface soil moisture as well as total soil profile is warranted for increased landslide prediction in the LMRB.

There are several limitations associated with this study that should be noted. First, only three event-based inventories in October 2020 were available to validate the LHASA models, and these

inventories were all located within the borders of Vietnam. Therefore, validation of the model predictions in other areas of the LMRB is unable to be performed. Additional inventories are needed to validate both spatially and temporally for a full understanding of how the soil moisture is affecting the models. The topography and climate varies throughout the LMRB, and model performance can't be fully determined without additional landslide inventories that represent a broader variety of locations. Another limitation involves the uncertainty associated with satellite-based estimations of soil moisture and the inability to validate the products with ground measurements due to the lack of an in-situ soil moisture network in the LMRB. Future research related to this study could apply a gap-filling method to the 1 km soil moisture to address the spatio-temporal variability it maintains at present. Additionally, this methodology can be applied as landslide inventory information becomes available. However, applying remotely sensed products in the LHASA framework has the ability to provide important insights into landslide hazard for regions lacking sufficient ground measurements like the LMRB. The methodology of this research can be applied to other data-sparse regions to estimate landslide hazard and risk as the datasets used in this study are publicly available or are available upon request. Insights into the applications and limitations of various soil moisture products can aid landslide hazard mitigation as antecedent soil moisture conditions play an important role in landslide occurrence.

Chapter 6. Conclusions

This dissertation includes the execution and planning of four projects with the broad goal of applying remote sensing and modelled data to address increasing rainfall-induced landslide hazards in the Lower Mekong River Basin (LMRB) due to climate change and human expansion. Using satellite-based products can supplement the sparse ground data available in this region and provide a better understanding of landslide susceptibility and risk that decision-makers require for disaster mitigation and prevention. The major findings of this dissertation are:

- Satellite-based estimates can be used in data sparse regions like the LMRB as they are able to represent the seasonality of the climate similar to rain gauges and correlate well with ground measurements where available for comparison.
- Dynamic land cover changes can influence landslide susceptibility especially in mountainous terrain. Natural revegetation after agricultural abandonment showed to contribute to landslide susceptibility more so than other alterations in land use, indicating these areas could be at more risk for landslide occurrence.
- Landslides are not reported uniformly globally or between the countries in the LMRB, despite it being one of the most landslide prone areas on the globe. Global landslide catalogs represent a minimum estimate of landslides that occur, and the LMRB is underestimated in global reporting especially in mountainous, remote regions with low population density.
- The inclusion of satellite-based soil moisture products can aid landslide monitoring in regions like the LMRB that lack an in situ soil moisture network. Satellite-based and modelled soil moisture are able to represent the variations and seasonality in antecedent moisture conditions necessary for landslide prediction.

Approaching landslide hazard in the LMRB with novel applications of datasets and methodology we can further understand landslide hazards and potential mitigation strategies in the region. The hydrologic significance of satellite-based products in the LMRB can be assessed

from the results of this study and other validation studies. The important broad impacts of this research are the implications of remotely sensed products for landslide hazard monitoring, specifically in the LMRB or similar un-gauged basins. Assessing the available remotely sensed products in data sparse regions is essential to look at the progression and advancement in satellite-based estimation in regions like the LMRB. With increasing temporal and spatial coverage, satellite-based inputs will serve as an improvement, compared to precipitation from ground measurements for landslide hazard modeling in basins like LMRB.

References

1. Abella, E. A. C., & Van Westen, C. J. (2007). Generation of a landslide risk index map for Cuba using spatial multi-criteria evaluation. Landslides, 4(4), 311–325. https://doi.org/10.1007/s10346-007-0087-y
2. Ahamed, A.; Bolten, J. A MODIS-based automated flood monitoring system for southeast asia. Int. J. Appl. Earth Obs. Geoinf. 2017, 61, 104–117.
3. Amatya P, Kirschbaum D, Stanley T, Tanyas H (2021a) Landslide mapping using object-based image analysis and open source tools. Eng Geol 282:. https://doi.org/10.1016/j.enggeo.2021.106000
4. Amatya P, Kirschbaum D, Stanley T, Tanyas H (2021b) Rainfall-induced landslide inventories for Lower Mekong based on Planet imagery and a semi-automatic mapping method. Geosci Data J
5. Amatya, P., Kirschbaum, D., & Stanley, T. (2019). Use of very high-resolution optical data for landslide mapping and susceptibility analysis along the Karnali highway, Nepal. Remote Sensing, 11(19). https://doi.org/10.3390/rs11192284
6. Amatya, P., Kirschbaum, D., & Stanley, T. (2022). Rainfall-induced landslide inventories for Lower Mekong based on Planet imagery and a semi-automatic mapping method. Geoscience Data Journal. https://doi.org/10.1002/gdj3.145
7. Andreadis, K. M., Das, N., Stampoulis, D., Ines, A., Fisher, J. B., Granger, S., Kawata, J., Han, E., & Behrangi, A. (2017). The regional hydrologic extremes assessment system: A software framework for hydrologic modeling and data assimilation. PLoS ONE, 12(5), 1–22. https://doi.org/10.1371/journal.pone.0176506
8. Andreadis, K. M., Das, N., Stampoulis, D., Ines, A., Fisher, J. B., Granger, S., Kawata, J., Han, E., & Behrangi, A. (2017). The regional hydrologic extremes assessment system: A software framework for hydrologic modeling and data assimilation. PLoS ONE, 12(5), 1–22. https://doi.org/10.1371/journal.pone.0176506
9. Ayehu, G.T.; Tadesse, T.; Gessesse, B.; Dinku, T. Validation of new satellite rainfall products over the Upper Blue Nile Basin, Ethiopia. In Atmospheric Measurement Techniques Discussions; Copernicus Publications on behalf of the European Geosciences Union. 2017; pp. 1–24.
10. Bai, L.; Shi, C.; Li, L.; Yang, Y.; Wu, J. Accuracy of CHIRPS Satellite-Rainfall Products over Mainland China. Remote Sens. 2018, 10, 362.
11. Batjes NH, Ribeiro E, Van Oostrum A (2020) Standardised soil profile data to support global mapping and modelling (WoSIS snapshot 2019). Earth Syst Sci Data 12:299–320. https://doi.org/10.5194/essd-12-299-2020
12. Benz, S. A., & Blum, P. (2019). Global detection of rainfall-triggered landslide clusters. Natural Hazards and Earth System Sciences, 19(7), 1433–1444. https://doi.org/10.5194/nhess-19-1433-2019
13. Beria, H.; Nanda, T.; Bisht, D.S.; Chatterjee, C. Does the GPM mission improve the systematic error component in satellite rainfall estimates over TRMM? An evaluation at a pan-India scale. Hydrol. Earth Syst. Sci. 2017, 21, 6117–6134.

14. Bessette-Kirton, E. K., Cerovski-Darriau, C., Schulz, W. H., Coe, J. A., Kean, J. W., Godt, J. W., Thomas, M. A., & Stephen Hughes, K. (2019). Landslides triggered by Hurricane Maria: Assessment of an extreme event in Puerto Rico. GSA Today, 29(6), 4–10. https://doi.org/10.1130/GSATG383A.1
15. Bhandary, N. P., Dahal, R. K., Timilsina, M., & Yatabe, R. (2013). Rainfall event-based landslide susceptibility zonation mapping. Natural Hazards, 69(1), 365–388. https://doi.org/10.1007/s11069-013-0715-x
16. Biswas, N. K., Stanley, T. A., Kirschbaum, D. B., Amatya, P. M., Meechaiya, C., Poortinga, A., & Towashiraporn, P. (2022). A dynamic landslide hazard monitoring framework for the Lower Mekong Region. Frontiers in Earth Science, 10 (November), 1–15. https://doi.org/10.3389/feart.2022.1057796
17. Biswas, N. K., Stanley, T. A., Kirschbaum, D. B., Amatya, P. M., Meechaiya, C., Poortinga, A., & Towashiraporn, P. (2022). A dynamic landslide hazard monitoring framework for the Lower Mekong Region. Frontiers in Earth Science, 10(November), 1–15. https://doi.org/10.3389/feart.2022.1057796
18. Blacutt, L.A.; Herdies, D.L.; De Goncalves, L.G.G.; Vila, D.A.; Andrade, M. Precipitation comparison for the CFSR, MERRA, TRMM3B42 and Combined Scheme datasets in Bolivia. Atmos. Res. 2015, 163, 117–131.
19. Boergens, E.; Dettmering, D.; Schwatke, C.; Seitz, F. Treating the Hooking Effect in Satellite Altimetry Data: A Case Study along the Mekong River and Its Tributaries. Remote Sens. 2016, 8, 91.
20. Bornaetxea T, Rossi M, Marchesini I, Alvioli M (2018) Effective surveyed area and its role in statistical landslide susceptibility assessments. Nat Hazards Earth Syst Sci Discuss 1–22. https://doi.org/10.5194/nhess-2018-88
21. Camilo DC, Lombardo L, Mai PM, et al (2017) Handling high predictor dimensionality in slope-unit-based landslide susceptibility models through LASSO-penalized Generalized Linear Model. Environ Model Softw 97:145–156. https://doi.org/10.1016/j.envsoft.2017.08.003
22. Chan, S.K.; Bindlish, R.; O'Neill, P.; Jackson, T.; Njoku, E.; Dunbar, S.; Kerr, Y.; Berg, A.; Chen, F.;Walker, J.; et al. Development and assessment of the SMAP enhanced passive soil moisture product. Remote Sens. Environ. 2018, 204, 931–941.
23. Chandrasekaran, S. S., Sayed Owaise, R., Ashwin, S., Jain, R. M., Prasanth, S., & Venugopalan, R. B. (2013). Investigation on infrastructural damages by rainfall-induced landslides during November 2009 in Nilgiris, India. Natural Hazards, 65(3), 1535–1557. https://doi.org/10.1007/s11069-012-0432-x
24. Chang, K., Chiang, S. Hao, Chen, Y. Chin, & Mondini, A. C. (2014). Modeling the spatial occurrence of shallow landslides triggered by typhoons. Geomorphology, 208, 137–148. https://doi.org/10.1016/j.geomorph.2013.11.020
25. Chau KT, Sze YL, Fung MK, Wong WY, Fong EL, Chan LCP (2004) Landslide hazard analysis for Hong Kong using landslide inventory and GIS. Comput Geosci 30:429–443. doi:10.1016/j.cageo.2003.08.013

26. Chen CY, Huang WL (2013) Land use change and landslide characteristics analysis for community-based disaster mitigation. Environ Monit Assess 185:4125–4139. https://doi.org/10.1007/s10661-012-2855-y
27. Chen L, Guo Z, Yin K, et al (2019) The influence of land use and land cover change on landslide susceptibility: A case study in Zhushan Town, Xuan'en County (Hubei, China). Nat Hazards Earth Syst Sci 19:2207–2228. https://doi.org/10.5194/nhess-19-2207-2019
28. Chen, Y. C., Chang, K. T., Chiu, Y. J., Lau, S. M., & Lee, H. Y. (2013). Quantifying rainfall controls on catchment-scale landslide erosion in Taiwan. Earth Surface Processes and Landforms, 38(4), 372–382. https://doi.org/10.1002/esp.3284
29. Colliander, A.; Jackson, T.J.; Bindlish, R.; Chan, S.; Das, N.; Kim, S.B.; Asanuma, J.; Aida, K.; Berg, A.; Bosch, D.; et al. Validation of SMAP surface soil moisture products with core validation sites. Remote Sens. Environ. 2017, 191, 215–231.
30. Collischonn, W.; Tucci, C.E.M. Daily hydrological modeling in the Amazon basin using TRMM rainfall estimates. J. Hydrol. 2008, 360, 207–216.
31. Crozier, M. J. (2010). Deciphering the effect of climate change on landslide activity: A review. Geomorphology, 124(3–4), 260–267. https://doi.org/10.1016/j.geomorph.2010.04.009
32. Culler, E., Livneh, B., Rajagopalan, B., & Tiampo, K. (2021). A data-driven evaluation of post-fire landslide susceptibility. Natural Hazards and Earth System Sciences, April, 1–24. https://doi.org/10.5194/nhess-2021-111
33. Dai FC, Lee CF, Ngai YY (2002) Landslide risk assessment and management: An overview. Eng Geol 64:65–87. https://doi.org/10.1016/S0013-7952(01)00093-X
34. Dai, L., Fu, R., Guo, X., Du, Y., Zhang, F., & Cao, G. (2022). Soil Moisture Variations in Response to Precipitation Across Different Vegetation Types on the Northeastern Qinghai-Tibet Plateau. Frontiers in Plant Science, 13. https://doi.org/10.3389/fpls.2022.854152
35. Dandridge C, Lakshmi V, Bolten J, Srinivasan R (2019) Evaluation of satellite-based rainfall estimates in the Lower Mekong River Basin (Southeast Asia). Remote Sens 11:. https://doi.org/10.3390/rs11222709
36. Dandridge, C., Stanley, T. A., Kirschbaum, D. B., & Lakshmi, V. (2023). Spatial and Temporal Analysis of Global Landslide Reporting Using a Decade of the Global Landslide Catalog. Sustainability (Switzerland), 15(4), 1–22. https://doi.org/10.3390/su15043323
37. Dandridge, C.; Fang, B.; Lakshmi, V. (2020). Downscaling of SMAP Soil Moisture in the Lower Mekong River Basin. Water, 12, 56.
38. Dandridge, C.; Fang, B.; Lakshmi, V. Downscaling of SMAP Soil Moisture in the Lower Mekong River Basin. Water 2020, 12, 56. https://doi.org/10.3390/w12010056
39. Dandridge, C.; Stanley, T.; Kirschbaum, D.; Amatya, P.; & Lakshmi, V. (2022). The influence of land use and land cover change on landslide susceptibility in the Lower Mekong River Basin. Natural Hazards, 0123456789. https://doi.org/10.1007/s11069-022-05604-4
40. Das G, Lepcha K (2019) Application of logistic regression (LR) and frequency ratio (FR) models for landslide susceptibility mapping in Relli Khola river basin of Darjeeling Himalaya, India. SN Appl Sci 1:1–22. https://doi.org/10.1007/s42452-019-1499-8
41. Degraff J V., Cannon SH, Gartner JE (2015) The timing of susceptibility to post-fire debris flows in the western United States. Environ Eng Geosci 21:277–292. https://doi.org/10.2113/gseegeosci.21.4.277

42. Deng X, Xu D, Zeng M, Qi Y (2018) Landslides and cropland abandonment in China's mountainous areas: Spatial distribution, empirical analysis and policy implications. Sustain 10:. https://doi.org/10.3390/su10113909
43. Dinku, T.; Chidzambwa, S.; Ceccato, P.; Connor, S.J.; Ropelewski, C.F. Validation of high-resolution satellite rainfall products over complex terrain. Int. J. Remote Sens. 2008, 29, 4097–4110.
44. Dos Reis, J.B.C.; Rennó, C.D.; Lopes, E.S.S. Validation of Satellite Rainfall Products over a Mountainous Watershed in a Humid Subtropical Climate Region of Brazil. Remote Sens. 2017, 9, 1240.
45. Emberson, R., Kirschbaum, D. B., Amatya, P., Tanyas, H., & Marc, O. (2022). Insights from the topographic characteristics of a large global catalog of rainfall-induced landslide event inventories. Natural Hazards and Earth System Sciences, 22(3), 1129–1149. https://doi.org/10.5194/nhess-22-1129-2022
46. Entekhabi, D.; Njoku, E.; Oneill, P.; Spencer, M.; Jackson, T.; Entin, J.; Jhonson, J.; Kimbal, J.; Kellogg, K.; Martin, N.; et al. The soil moisture active/passive mission (SMAP). Int. Geosci. Remote Sens. Symp. 2010, 98, 704–716.
47. Fang, B., Lakshmi, V., Cosh, M., Liu, P. W., Bindlish, R., & Jackson, T. J. (2022). A global 1-km downscaled SMAP soil moisture product based on thermal inertia theory. Vadose Zone Journal, 21(2). https://doi.org/10.1002/vzj2.20182
48. Fang, B., Lakshmi, V., Cosh, M., Liu, P. W., Bindlish, R., & Jackson, T. J. (2022). A global 1-km downscaled SMAP soil moisture product based on thermal inertia theory. Vadose Zone Journal, 21(2). https://doi.org/10.1002/vzj2.20182
49. Fang, B.; Kansara., P; Dandridge, C; Lakshmi, V. Drought Monitoring using High Spatial Resolution Soil Moisture Data over Australia in 2015-2019, J. of Hydrol. 2021, 594. https://doi.org/10.1016/j.jhydrol.2021.125960.
50. Farahmand, A. and AghaKouchak, A.: A satellite-based global landslide model, Nat. Hazards Earth Syst. Sci., 13, 1259–1267, https://doi.org/10.5194/nhess-13-1259-2013, 2013.
51. Farahmand, A., & Aghakouchak, A. (2013). A satellite-based global landslide model. 1259–1267. https://doi.org/10.5194/nhess-13-1259-2013
52. Farr, T. G., & M. Kobrick, (2000). Shuttle Radar Topography Mission produces a wealth of data. Eos Trans. AGU, 81:583-583.
53. Fayne, J. V., Bolten, J. D., Doyle, C. S., Fuhrmann, S., Rice, M. T., Houser, P. R., & Lakshmi, V. (2017). Flood mapping in the lower Mekong River Basin using daily MODIS observations. International Journal of Remote Sensing, 38(6), 1737–1757. https://doi.org/10.1080/01431161.2017.1285503
54. Felicísimo ÁM, Cuartero A, Remondo J, Quirós E (2013) Mapping landslide susceptibility with logistic regression, multiple adaptive regression splines, classification and regression trees, and maximum entropy methods: A comparative study. Landslides 10:175–189. https://doi.org/10.1007/s10346-012-0320-1
55. Food and Agriculture Organization and World Bank Population Density. Available online: https://data.worldbank.org/indicator/EN.POP.DNST (accessed on March 15 2022).
56. Food and Agriculture Organization Surface Area. Available online: https://data.worldbank.org/indicator/AG.SRF.TOTL.K2 (accessed on March 15 2022).

57. Forbes K, Broadhead J, Bischetti GB, et al (2012) The role of trees and forests in the prevention of landslides and rehabilitation of landslide-affected areas in Asia Second edition In collaboration with. For landslides 12–21
58. Froude, M. J., & Petley, D. N. (2018). Global fatal landslide occurrence from 2004 to 2016. Natural Hazards and Earth System Sciences, 18(8), 2161–2181. https://doi.org/10.5194/nhess-18-2161-2018
59. Funk, C.; Peterson, P.; Landsfeld, M.; Pedreros, D.; Verdin, J.; Shukla, S.; Husak, G.; Rowland, J.; Harrison, L.; Hoell, A.; Michaelsen, J. The climate hazards infrared precipitation with stations—a new environmental record for monitoring extremes. Sci Data. 2015, 2, 150066, doi:10.1038/sdata.2015.66.
60. Gariano SL, Petrucci O, Rianna G, et al (2018) Impacts of past and future land changes on landslides in southern Italy. Reg Environ Chang 18:437–449. https://doi.org/10.1007/s10113-017-1210-9
61. Gariano, S. L., & Guzzetti, F. (2016). Landslides in a changing climate. Earth-Science Reviews, 162, 227–252. https://doi.org/10.1016/j.earscirev.2016.08.011
62. Gebremichael, M.; Bitew, M.M.; Hirpa, F.A.; Tesfay, G.N. Accuracy of satellite rainfall estimates in the Blue Nile Basin: Lowland plain versus highland mountain. Water Resour. Res. 2014, 50, 8775–8790.
63. Glade T (2003) Landslide occurrence as a response to land use change: A review of evidence from New Zealand. Catena 51:297–314. https://doi.org/10.1016/S0341-8162(02)00170-4
64. Golian, S.; Moazami, S.; Kirstetter, P.-E.; Hong, Y. Evaluating the Performance of Merged Multi-Satellite Precipitation Products Over a Complex Terrain. Water Resour. Manag. 2015, 29, 4885–4901.
65. Gorsevski P V., Gessler PE, Foltz RB, Elliot WJ (2006) Spatial prediction of landslide hazard using logistic regression and ROC analysis. Trans GIS 10:395–415. https://doi.org/10.1111/j.1467-9671.2006.01004.x
66. Guo, H.; Bao, A.; Liu, T.; Ndayisaba, F.; He, D.; Kurban, A.; De Maeyer, P. Meteorological Drought Analysis in the Lower Mekong Basin Using Satellite-Based Long-Term CHIRPS Product. Sustainability 2017, 9, 901.
67. Guzzetti F (2000) Landslide fatalities and the evaluation of landslide risk in Italy. Eng Geol 58:89–107. doi:10.1016/S0013-7952(00)00047-8
68. Guzzetti F, Cardinali M, Reichenbach P (1994) The AVI project: a bibliographical and archive inventory of landslides and floods in Italy. Environ Manag 18:623–633. doi:10.1007/BF02400865
69. Hansen MC, Potapov P V., Moore R, et al (2013) High-resolution global maps of 21st-century forest cover change. Science (80-) 342:850–853. https://doi.org/10.1126/science.1244693
70. Hansen, M. C., Potapov, P. V., Moore, R., Hancher, M., Turubanova, S. A., Tyukavina, A., Thau, D., Stehman, S. V., Goetz, S. J., Loveland, T. R., Kommareddy, A., Egorov, A., Chini, L., Justice, C. O., & Townshend, J. R. G. (2013). High-resolution global maps of 21st-century forest cover change. Science, 342(6160), 850–853.

71. Hartmann, J., & Moosdorf, N. (2012). The new global lithological map database GLiM: A representation of rock properties at the Earth surface. Geochemistry, Geophysics, Geosystems, 13(12).
72. Hemasinghe H, Rangali RSS, Deshapriya NL, Samarakoon L (2018) Landslide susceptibility mapping using logistic regression model (a case study in Badulla District, Sri Lanka). Procedia Eng 212:1046–1053. https://doi.org/10.1016/j.proeng.2018.01.135
73. Hengl T, De Jesus JM, Heuvelink GBM, et al (2017) SoilGrids250m: Global gridded soil information based on machine learning
74. Hermance, J.F.; Sulieman, H.M. Adequacy of the daily TMPA 3B42 high-resolution satellite precipitation product for monitoring hydrometeorological hazards in the Southeast Sahel of Africa. Int. J. Remote Sens. 2018, 39, 2579–2596.
75. Hewawasam T (2010) Effect of land use in the upper Mahaweli catchment area on erosion landslides and siltation in hydropower reservoirs of Sri Lanka. J Natl Sci Found Sri Lanka 38:3–14. https://doi.org/10.4038/jnsfsr.v38i1.1721
76. Highland L, Bobrowsky P (2008) The Landslide Handbook-A Guide to Understanding Landslides. Landslide Handbook - A Guide to Understanding Landslides 4–42.
77. Hong, Y., Adler, R. & Huffman, G. Use of satellite remote sensing data in the mapping of global landslide susceptibility. Nat Hazards43, 245–256 (2007). https://doi.org/10.1007/s11069-006-9104-z
78. Horafas D, Gkeki T (2017) Applying Logistic Regression for Landslide Susceptibility Mapping . The Case Study of Krathis Watershed , North Peloponnese , Greece. 6:23–28. https://doi.org/10.5923/s.ajgis.201701.03
79. Huffman, G.; Adler, R.; Bolvin, D.; Guojun, G.; Nelkin, E.; Bowman, K.; Hong, Y.; Stocker, E.; Wolff, D. The TRMM Multisatellite Precipitation Analysis (TMPA): Quasi-global, multiyear, combined-sensor precipitation estimates at fine scales. J. Hydrometeorol. 2007, 8, 38–55.
80. Huffman, G.J., D.T. Bolvin, E.J. Nelkin, and R.F. Adler (2016), TRMM (TMPA) Precipitation L3 1 day 0.25 degree x 0.25 degree V7, Edited by Andrey Savtchenko, Goddard Earth Sciences Data and Information Services Center (GES DISC).
81. Huffman, G.J., E.F. Stocker, D.T. Bolvin, E.J. Nelkin, Jackson Tan (2019), GPM IMERG Final Precipitation L3 Half Hourly 0.1 degree x 0.1 degree V06, Greenbelt, MD, Goddard Earth Sciences Data and Information Services Center (GES DISC), Accessed: [Data Access Date], doi:10.5067/GPM/IMERG/3B-HH/06
82. Huffman, G.J.; Bolvin, D.T.; Braithwaite, D.; Hsu, K.; Joyce, R. NASA Global Precipitation Measurement (GPM) Integrated Multi-satellitE Retrievals for GPM (IMERG). In Algorithm Theoretical Basis Document (ATBD) Version 4.5; NASA: Greenbelt, MD, USA, 2015.
83. Hughes, D. Comparison of satellite rainfall data with observations from gauging station networks. J. Hydrol. 2006, 327, 399–410.
84. Hughes, K.S., and Schulz, W.H., (2020). Map depicting susceptibility to landslides triggered by intense rainfall, Puerto Rico: U.S. Geological Survey Open-File Report 2020–1022, 91 p., 1 plate, scale 1:150,000, https://doi.org/10.3133/ofr20201022.

85. Indhanu T, Chub-Uppakarn T, Chalermyanont T (2020) Geotechnical Analysis of a Landslide in Nakorn Si Thammarat Province, Southern Thailand. Lect Notes Civ Eng 62:923–927. https://doi.org/10.1007/978-981-15-2184-3_120
86. Jaboyedoff M, Michoud C, Derron MH, et al (2016) Human-Induced Landslides: Toward the analysis of anthropogenic changes of the slope environment. Landslides Eng Slopes Exp Theory Pract 1:217–232. https://doi.org/10.1201/b21520-20
87. Juang, C. S., Stanley, T. A., & Kirschbaum, D. B. (2019). Using citizen science to expand the global map of landslides: Introducing the cooperative open online landslide repository (COOLR). PLoS ONE, 14(7), 1–28. https://doi.org/10.1371/journal.pone.0218657
88. Kafy A- Al, Shahinoor Rahman M, Ferdous L (2017) Exploring the Association of Land Cover Change and Landslides in the Chittagong Hill Tracts (Cht): a Remote Sensing Perspective. Proceedings, Int Conf Disaster Risk Mitig
89. Karsli F, Atasoy M, Yalcin A, et al (2009) Effects of land-use changes on landslides in a landslide-prone area (Ardesen, Rize, NE Turkey). Environ Monit Assess 156:241–255. https://doi.org/10.1007/s10661-008-0481-5
90. Katsanos, D.; Lagouvardos, K.; Kotroni, V.; Huffmann, G.J. Statistical evaluation of MPA-RT high-resolution precipitation estimates from satellite platforms over the central and eastern Mediterranean. Geophys. Res. Lett. 2004, 31, doi:10.1029/2003GL019142.
91. Kean JW, Staley DM, Cannon SH (2011) In situ measurements of post-fire debris flows in southern California: Comparisons of the timing and magnitude of 24 debris-flow events with rainfall and soil moisture conditions. J Geophys Res Earth Surf 116:1–21. https://doi.org/10.1029/2011JF002005
92. Khan H, Shafique M, Khan MA, et al (2019) Landslide susceptibility assessment using Frequency Ratio, a case study of northern Pakistan. Egypt J Remote Sens Sp Sci 22:11–24. https://doi.org/10.1016/j.ejrs.2018.03.004
93. Kimani, M.W.; Hoedjes, J.C.B.; Su, Z. An Assessment of Satellite-Derived Rainfall Products Relative to Ground Observations over East Africa. Remote Sens. 2017, 9, 430.
94. Kirschbaum, D. B., Adler, R., Hong, Y., Hill, S., & Lerner-Lam, A. (2010). A global landslide catalog for hazard applications: Method, results, and limitations. Natural Hazards, 52(3), 561–575. https://doi.org/10.1007/s11069-009-9401-4
95. Kirschbaum, D. B., Adler, R., Hong, Y., Kumar, S., Peters-Lidard, C., & Lerner-Lam, A. (2012). Advances in landslide nowcasting: Evaluation of a global and regional modeling approach. Environmental Earth Sciences, 66(6), 1683–1696. https://doi.org/10.1007/s12665-011-0990-3
96. Kirschbaum, D. B., Stanley, T., & Simmons, J. (2015). A dynamic landslide hazard assessment system for Central America and Hispaniola. Natural Hazards and Earth System Sciences, 15(10), 2257–2272. https://doi.org/10.5194/nhess-15-2257-2015
97. Kirschbaum, D. B., T. Stanley, & Y. Zhou. (2015) Spatial and temporal analysis of a global landslide catalog. Geomorphology, 249 (Geohazard Databases): 4-15. http://dx.doi.org/10.1016/j.geomorph.2015.03.016
98. Kirschbaum, D.B., Adler, R., Adler, D., Peters-Lidard, C., & Huffman, G. (2012). Global distribution of extreme precipitation and high-impact landslides in 2010 relative to

previous years. Journal of Hydrometeorology, 13(5), 1536–1551. https://doi.org/10.1175/JHM-D-12-02.1
99. Kummu, M.; Varis, O. Sediment-related impacts due to upstream reservoir trapping, the Lower Mekong River. Geomorphology 2007, 85, 275–293.
100. Lakshmi, V. The role of satellite remote sensing in the Prediction of Ungauged Basins. Hydrol. Process. 2004, 18, 1029–1034.
101. Lakshmi, V., Le, M., Goffin, B. D., Besnier, J., Pham, H. T., Do, H., Fang, B., Mohammed, I., & Bolten, J. D. (2023). Journal of Hydrology : Regional Studies Regional analysis of the 2015 – 16 Lower Mekong River basin drought using NASA satellite observations. Journal of Hydrology: Regional Studies, 46(March), 101362. https://doi.org/10.1016/j.ejrh.2023.101362
102. Larsen MC, Parks JE (1997) How wide is a road? The association of roads and mass-wasting in a forested montane environment. Earth Surf Process Landforms 22:835–848. https://doi.org/10.1002/(SICI)1096-9837(199709)22:9<835::AID-ESP782>3.0.CO;2-C
103. Lauri, H.; De Moel, H.; Ward, P.J.; Räsänen, T.A.; Keskinen, M.; Kummu, M. Future changes in Mekong River hydrology: Impact of climate change and reservoir operation on discharge. Hydrol. Earth Syst. Sci. Discuss. 2012, 9, 6569–6614.
104. Le, H. M., Sutton, J. R. P., Bui, D. Du, Bolten, J. D., & Lakshmi, V. (2018). Comparison and bias correction of TMPA precipitation products over the lower part of Red-Thai Binh River Basin of Vietnam. Remote Sensing, 10(10). https://doi.org/10.3390/rs10101582
105. Lee S, Sambath T (2006) Landslide susceptibility mapping in the Damrei Romel area, Cambodia using frequency ratio and logistic regression models. Environ Geol 50:847–855. https://doi.org/10.1007/s00254-006-0256-7
106. Lehner, B., & Grill G. (2013). Global river hydrography and network routing: baseline data and new approaches to study the world's large river systems. Hydrological Processes, 27(15): 2171–2186.
107. Leiba, M. (2013). Impact of landslides in Australia to December 2011. Australian Journal of Emergency Management, 28(1).
108. Li, J., Wang, X., Jia, H., Liu, Y., Zhao, Y., Shi, C., Zhang, F., & Wang, K. (2021). Assessing the soil moisture effects of planted vegetation on slope stability in shallow landslide- Billah prone areas.
109. Li, Z.; Yang, D.; Hong, Y. Multi-scale evaluation of high-resolution multi-sensor blended global precipitation products over the Yangtze River. J. Hydrol. 2013, 500, 157–169.
110. Liao, Z., Hong, Y., Wang, J., Fukuoka, H., Sassa, K., Karnawati, D., & Fathani, F. (2010). Prototyping an experimental early warning system for rainfall-induced landslides in Indonesia using satellite remote sensing and geospatial datasets. Landslides, 7(3), 317–324. https://doi.org/10.1007/s10346-010-0219-7
111. Lin, L., Lin, Q., & Wang, Y. (2017). Landslide susceptibility mapping on a global scale using the method of logistic regression. Natural Hazards and Earth System Sciences, 17(8), 1411–1424. https://doi.org/10.5194/nhess-17-1411-2017
112. Lin, Q., & Wang, Y. (2018). Spatial and temporal analysis of a fatal landslide inventory in China from 1950 to 2016. Landslides, 15(12), 2357–2372. https://doi.org/10.1007/s10346-018-1037-6

113. Liu J, Wu Z, Zhang H (2021) Analysis of changes in landslide susceptibility according to land use over 38 years in lixian county, china. Sustain 13:. https://doi.org/10.3390/su131910858
114. Liu, L., Bai, P., Liu, C., Tian, W., & Liang, K. (2020). Changes in Extreme Precipitation in the Mekong Basin. Advances in Meteorology, 2020, 8874869. https://doi.org/10.1155/2020/8874869
115. Lombardo L, Mai PM (2018) Presenting logistic regression-based landslide susceptibility results. Eng Geol 244:14–24. https://doi.org/10.1016/j.enggeo.2018.07.019
116. Loo, Y.Y., Billa, L., & Singh, A. (2015). Effect of climate change on seasonal monsoon in Asia and its impact on the variability of monsoon rainfall in Southeast Asia. Geosci Front 6:817–823. https://doi.org/10.1016/j.gsf.2014.02.009
117. Lu, X.; Wei, M.; Tang, G.; Zhang, Y. Evaluation and correction of the TRMM 3B43V7 and GPM 3IMERGM satellite precipitation products by use of ground-based data over Xinjiang, China. Environ. Earth Sci. 2018, 77, 209.
118. Luo, S., Sarabandi, K., Tong, L., & Pierce, L. E. (2016). Landslide prediction using soil moisture estimation derived from polarimetric Radarsat-2 data and SRTM. June 2018. https://doi.org/10.1109/IGARSS.2016.7730403
119. Manconi, A., & Giordan, D. (2016). Landslide failure forecast in near-real-time. Geomatics, Natural Hazards and Risk, 7(2), 639–648. https://doi.org/10.1080/19475705.2014.942388
120. Marc, O., Jucá Oliveira, R. A., Gosset, M., Emberson, R., & Malet, J. P. (2022). Global assessment of the capability of satellite precipitation products to retrieve landslide-triggering extreme rainfall events. Earth Interactions, 26(1), 122–138. https://doi.org/10.1175/EI-D-21-0022.1
121. Marc, O., Stumpf, A., Malet, J. P., Gosset, M., Uchida, T., & Chiang, S. H. (2018). Initial insights from a global database of rainfall-induced landslide inventories: The weak influence of slope and strong influence of total storm rainfall. Earth Surface Dynamics, 6(4), 903–922. https://doi.org/10.5194/esurf-6-903-2018
122. McAdoo BG, Quak M, Gnyawali KR, et al (2018) Roads and landslides in Nepal: How development affects environmental risk. Nat Hazards Earth Syst Sci 18:3203–3210. https://doi.org/10.5194/nhess-18-3203-2018
123. Meijer JR, Huijbregts MAJ, Schotten KCGJ, Schipper AM (2018) Global patterns of current and future road infrastructure. Environ Res Lett 13:. https://doi.org/10.1088/1748-9326/aabd42
124. Meijer, J. R., Huijbregts, M. A. J., Schotten, K. C. G. J., & Schipper, A. M. (2018). Global patterns of current and future road infrastructure. Environmental Research Letters, 13(6).
125. Mekong Drought and Crop Watch (MDCW), 2020, ADPC/SERVIR Mekong, https://mdcw-servir.adpc.net
126. Micheletti, N., Foresti, L., Robert, S., Leuenberger, M., Pedrazzini, A., Jaboyedoff, M., & Kanevski, M. (2014). Machine Learning Feature Selection Methods for Landslide Susceptibility Mapping. Mathematical Geosciences, 46(1), 33–57. https://doi.org/10.1007/s11004-013-9511-0
127. Mirus, B. B., Jones, E. S., Baum, R. L., Godt, J. W., Slaughter, S., Crawford, M. M., Lancaster, J., Stanley, T., Kirschbaum, D. B., Burns, W. J., Schmitt, R. G., Lindsey, K. O., & McCoy, K.

M. (2020). Landslides across the USA: occurrence, susceptibility, and data limitations. Landslides, 17(10), 2271–2285. https://doi.org/10.1007/s10346-020-01424-4
128. Mohammed IN, Bolten JD, Srinivasan R, Lakshmi V (2018) Satellite observations and modeling to understand the Lower Mekong River Basin streamflow variability. J Hydrol 564:559–573. https://doi.org/10.1016/j.jhydrol.2018.07.030
129. Mohammed, I.N.; Bolten, J.D.; Srinivasan, R.; Lakshmi, V. Improved Hydrological Decision Support System for the Lower Mekong River Basin Using Satellite-Based Earth Observations. Remote Sens. 2018, 10, 885.
130. Mohita Anand, S., & Jai Bhagwan, S. (2010). Use of Probability Distribution in Rainfall Analysis. New York Science Journal, 3(9), 40–49.
131. Mondal, A., Le, M. H., & Lakshmi, V. (2022). Land use, climate, and water change in the Vietnamese Mekong Delta (VMD) using earth observation and hydrological modeling. Journal of Hydrology: Regional Studies, 42. https://doi.org/10.1016/j.ejrh.2022.101132
132. Mugagga F, Kakembo V, Buyinza M (2012) Land use changes on the slopes of Mount Elgon and the implications for the occurrence of landslides. Catena 90:39–46. https://doi.org/10.1016/j.catena.2011.11.004
133. Naeimi, V.; Leinenkugel, P.; Sabel, D.; Wagner, W.; Apel, H.; Kuenzer, C. Evaluation of soil moisture retrieval from the ERS and metop scatterometers in the lower mekong basin. Remote Sens. 2013, 5, 1603–1623.
134. NASA JPL (2020) NASADEM Merged DEM Global 1 arc second V001. NASA EOSDIS Land Processes DAAC. Accessed from https://doi.org/10.5067/MEaSUREs/NASADEM/NASADEM_HGT.001
135. O, S.; Foelsche, U.; Kirchengast, G.; Fuchsberger, J.; Tan, J.; Petersen, W.A. Evaluation of GPM IMERG Early, Late, and Final rainfall estimates using WegenerNet gauge data in southeastern Austria. Hydrol. Earth Syst. Sci. 2017, 21, 6559–6572.
136. Oddo, P.C.; Ahamed, A.; Bolten, J.D. Socioeconomic Impact Evaluation for Near Real-Time Flood Detection in the Lower Mekong River Basin. Hydrology 2018, 5, 23.
137. Owen, Lewis , White, Gilbert F. and Jacobs, Jeffrey W. "Mekong River". Encyclopedia Britannica, 2023, https://www.britannica.com/place/Mekong-River.
138. Panciera, R.; Walker, J.P.; Jackson, T.J.; Gray, D.A.; Tanase, M.A.; Ryu, D.; Wu, X.L.; Yardley, H.; Monerris, A.; Gao, Y.; et al. The soil moisture active passive experiments (SMAPEx): Toward soil moisture retrieval from the SMAP mission. IEEE Trans. Geosci. Remote Sens. 2013, 52, 490–507.
139. Penna D, Borga M, Aronica GT, et al (2014) The influence of grid resolution on the prediction of natural and road-related shallow landslides. Hydrol Earth Syst Sci 18:2127–2139. https://doi.org/10.5194/hess-18-2127-2014
140. Persichillo MG, Bordoni M, Meisina C (2017) The role of land use changes in the distribution of shallow landslides. Sci Total Environ 574:924–937. https://doi.org/10.1016/j.scitotenv.2016.09.125
141. Petley, D. (2012). Global patterns of loss of life from landslides. Geology, 40(10), 927–930. https://doi.org/10.1130/G33217.1

142. Petley, D. N., Hearn, G. J., Hart, A., Rosser, N. J., Dunning, S. A., Oven, K., & Mitchell, W. A. (2007). Trends in landslide occurrence in Nepal. Natural Hazards, 43(1), 23–44. https://doi.org/10.1007/s11069-006-9100-3
143. Pisano L, Zumpano V, Malek, et al (2017) Variations in the susceptibility to landslides, as a consequence of land cover changes: A look to the past, and another towards the future. Sci Total Environ 601–602:1147–1159. https://doi.org/10.1016/j.scitotenv.2017.05.231
144. Ponziani, F., Pandolfo, C., Stelluti, M., Berni, N., Brocca, L., & Moramarco, T. (2012). Assessment of rainfall thresholds and soil moisture modeling for operational hydrogeological risk prevention in the Umbria region (central Italy). Landslides, 9(2), 229–237. https://doi.org/10.1007/s10346-011-0287-3
145. Pourghasemi HR, Moradi HR, Fatemi Aghda SM (2013) Landslide susceptibility mapping by binary logistic regression, analytical hierarchy process, and statistical index models and assessment of their performances. Nat Hazards 69:749–779. https://doi.org/10.1007/s11069-013-0728-5
146. Prakash, S.; Mahesh, C.; Gairola, R.M. Comparison of TRMM Multi-satellite Precipitation Analysis (TMPA)-3B43 version 6 and 7 products with rain gauge data from ocean buoys. Remote Sens. Lett. 2013, 4, 677–685.
147. Prastica RMS, Apriatresnayanto R, Marthanty DR (2019) Structural and green infrastructure mitigation alternatives prevent Ciliwung River from water-related landslide. Int J Adv Sci Eng Inf Technol 9:1825–1832. https://doi.org/10.18517/ijaseit.9.6.8413
148. Rabby, Y. W., Hossain, M. B., & Abedin, J. (2022). Landslide susceptibility mapping in three Upazilas of Rangamati hill district Bangladesh: application and comparison of GIS-based machine learning methods. Geocarto International, 37(12), 3371–3396. https://doi.org/10.1080/10106049.2020.1864026
149. Reichenbach P, Busca C, Mondini AC, Rossi M (2014) The Influence of Land Use Change on Landslide Susceptibility Zonation: The Briga Catchment Test Site (Messina, Italy). Environ Manage 54:1372–1384. https://doi.org/10.1007/s00267-014-0357-0
150. Reichenbach P, Rossi M, Malamud BD, et al (2018) A review of statistically-based landslide susceptibility models. Earth-Science Rev 180:60–91. https://doi.org/10.1016/j.earscirev.2018.03.001
151. Reichle, R. H., R. A. Lucchesi, J. V. Ardizzone, G.-K. Kim, E. B. Smith, and B. H. Weiss, 2022: Soil Moisture Active Passive (SMAP) Mission Level 4 Surface and Root Zone Soil Moisture (L4_SM) Product Specification Document. GMAO Office Note No. 10 (Version 1.6), 84 pp, NASA Goddard Space Flight Center, Greenbelt, MD, USA. Available from http://gmao.gsfc.nasa.gov/pubs/office_notes
152. Reichle, R., G. De Lannoy, R. D. Koster, W. T. Crow, J. S. Kimball, Q. Liu, and M. Bechtold. (2022). SMAP L4 Global 3-hourly 9 km EASE-Grid Surface and Root Zone Soil Moisture Geophysical Data, Version 7 [SPL4SMGP]. Boulder, Colorado USA. NASA National Snow and Ice Data Center Distributed Active Archive Center. https://doi.org/10.5067/EVKPQZ4AFC4D. Date Accessed 02-03-2023.
153. Remondo J, González A, Díaz de Terán JR, et al (2003) Validation of landslide susceptibility maps; examples and applications from a case study in northern Spain. Nat Hazards 30:437–449. https://doi.org/10.1023/B:NHAZ.0000007201.80743.fc

154. Saah D, Tenneson K, Poortinga A, et al (2020) Primitives as building blocks for constructing land cover maps. Int J Appl Earth Obs Geoinf 85:101979. https://doi.org/10.1016/j.jag.2019.101979
155. Sabo, J.L.; Ruhi, A.; Holtgrieve, G.W.; Elliott, V.; Arias, M.E.; Ngor, P.B.; Räsänen, T.A.; Nam, S. Designing river flows to improve food security futures in the Lower Mekong Basin. Science 2017, 358, eaao1053.
156. Saha, S., Moorthi, S., Wu, X., Wang, J., Nadiga, S., Tripp, P., Behringer, D., Hou, Y. T., Chuang, H. Y., Iredell, M., Ek, M., Meng, J., Yang, R., Mendez, M. P., Van Den Dool, H., Zhang, Q., Wang, W., Chen, M., & Becker, E. (2014). The NCEP climate forecast system version 2. Journal of Climate, 27(6), 2185–2208. https://doi.org/10.1175/JCLI-D-12-00823.1
157. Sahin, E. K. (2020). Assessing the predictive capability of ensemble tree methods for landslide susceptibility mapping using XGBoost, gradient boosting machine, and random forest. SN Applied Sciences, 2(7), 1–17. https://doi.org/10.1007/s42452-020-3060-1
158. Silalahi FES, Pamela, Arifianti Y, Hidayat F (2019) Landslide susceptibility assessment using frequency ratio model in Bogor, West Java, Indonesia. Geosci Lett 6:. https://doi.org/10.1186/s40562-019-0140-4
159. Simery, J.; Kean, D. Mekong River Commission Annual Report; Mekong River Commission. 2009.
160. Spruce J, Bolten J, Mohammed IN, et al (2020) Mapping Land Use Land Cover Change in the Lower Mekong Basin From 1997 to 2010. Front Environ Sci 8:. https://doi.org/10.3389/fenvs.2020.00021
161. Spruce J, Bolten J, Srinivasan R, Lakshmi V (2018) Developing land use land cover maps for the lower mekong basin to aid hydrologic modeling and basin planning. Remote Sens 10:. https://doi.org/10.3390/rs10121910
162. Stanley, T. A., & Kirschbaum, D. B. (2017), A heuristic approach to global landslide susceptibility mapping, Nat. Hazards, 1–20, doi:10.1007/s11069-017-2757-y
163. Stanley, T. A., Kirschbaum, D. B., Benz, G., Emberson, R. A., Amatya, P. M., Medwedeff, W., & Clark, M. K. (2021). Data-Driven Landslide Nowcasting at the Global Scale. Frontiers in Earth Science, 9(May), 1–15. https://doi.org/10.3389/feart.2021.640043
164. Styron, R., & Pagani, M. (2020). "The GEM Global Active Faults Database."Earthquake Spectra, vol. 36, no. 1_suppl, pp. 160–180.
165. Su, F.; Hong, Y.; Lettenmaier, D.P. Evaluation of TRMM Multisatellite Precipitation Analysis (TMPA) and Its Utility in Hydrologic Prediction in the La Plata Basin. J. Hydrometeorol. 2008, 9, 622–640.
166. Tan, M.L.; Duan, Z. Assessment of GPM and TRMM Precipitation Products over Singapore. Remote Sens. 2017, 9, 720.
167. Tang, G.; Zeng, Z.; Long, D.; Guo, X.; Yong, B.; Zhang, W.; Hong, Y. Statistical and Hydrological Comparisons between TRMM and GPM Level-3 Products over a Midlatitude Basin: Is Day-1 IMERG a Good Successor for TMPA 3B42V7? J. Hydrometeorol. 2016, 17, 121–137.
168. Tote, C.; Patricio, D.; Boogaard, H.; Van Der Wijngaart, R.; Tarnavsky, E.; Funk, C. Evaluation of Satellite Rainfall Estimates for Drought and Flood Monitoring in Mozambique. Remote Sens. 2015, 7, 1758–1776.

169. Trisurat, Y.; Aekakkararungroj, A.; Ma, H.-O.; Johnston, J.M. Basin-wide Impacts of Climate Change on Ecosystem Services in the Lower Mekong Basin. Ecol. Res. 2017, 33, 73–86.
170. Try, S., Tanaka, S., Tanaka, K., Sayama, T., Lee, G., & Oeurng, C. (2020). Assessing the effects of climate change on flood inundation in the lower Mekong Basin using high-resolution AGCM outputs. Progress in Earth and Planetary Science, 7(1). https://doi.org/10.1186/s40645-020-00353-z
171. van Westen, C. J., & Zhang, J. (2018). Landslides and floods triggered by Hurricane Maria. Unitar-Unosat. http://www.unitar.org/unosat/node/44/2762
172. Vennari, C., Salvati, P., Bianchi, C., Casarano, D., Parise, M., Basso, A., & Marchesini, I. (2022). AReGeoDatHa: Apulian Regional GeoDatabase for geo-hydrological Hazards. Journal of Environmental Management, 322. https://doi.org/10.1016/j.jenvman.2022.116051
173. Wang, S., Zhuang, J., Zheng, J., Fan, H., Kong, J., & Zhan, J. (2021). Application of Bayesian Hyperparameter Optimized Random Forest and XGBoost Model for Landslide Susceptibility Mapping. Frontiers in Earth Science, 9(July), 1–18. https://doi.org/10.3389/feart.2021.712240
174. Wang, W.; Lu, H.; Yang, D.; Sothea, K.; Jiao, Y.; Gao, B.; Peng, X.; Pang, Z. Modelling Hydrologic Processes in the Mekong River Basin Using a Distributed Model Driven by Satellite Precipitation and Rain Gauge Observations. PLoS ONE 2016, 11, e0152229.
175. Wang, W.; Lu, H.; Zhao, T.; Jiang, L.; Shi, J. Evaluation and Comparison of Daily Rainfall from Latest GPM and TRMM Products Over the Mekong River Basin. IEEE J. Sel. Top. Appl. Earth Obs. Remote Sens. 2017, 10, 1–10.
176. Whiteley, J. S., Chambers, J. E., Uhlemann, S., Wilkinson, P. B., & Kendall, J. M. (2019). Geophysical Monitoring of Moisture-Induced Landslides: A Review. Reviews of Geophysics, 57(1), 106–145. https://doi.org/10.1029/2018RG000603
177. Whiteley, J. S., Chambers, J. E., Uhlemann, S., Wilkinson, P. B., & Kendall, J. M. (2019). Geophysical Monitoring of Moisture-Induced Landslides: A Review. Reviews of Geophysics, 57(1), 106–145. https://doi.org/10.1029/2018RG000603
178. Wilkinson, P. L., Anderson, M. G., & Lloyd, D. M. (2002). An integrated hydrological model for rain-induced landslide prediction. Earth Surface Processes and Landforms, 27(12), 1285–1297. https://doi.org/10.1002/esp.409
179. Winter MG, Dixon N, Wasowski J, Dijkstra TA (2010) Introduction to land-use and climate change impacts on landslides. Q J Eng Geol Hydrogeol 43:367–370. https://doi.org/10.1144/1470-9236/10-035
180. World Bank and OECD National Accounts data files GDP Per Capita. Available online: https://data.worldbank.org/indicator/NY.GDP.PCAP.CD (accessed on March 15 2022).
181. Xian, L.; Wenqi, W.; Daming, H.; Yungang, L.; Xuan, J. Hydrological Simulation Using TRMM and CHIRPS Precipitation Estimates in the Lower Lancang-Mekong River Basin. Chin. Geogr. Sci. 2019, 29, 13–25, doi:10.1007/s11769-019-1014-6.
182. Zhang, J., Ma, X., Zhang, J., Sun, D., Zhou, X., Mi, C., & Wen, H. (2023). Insights into geospatial heterogeneity of landslide susceptibility based on the SHAP-XGBoost model. Journal of Environmental Management, 332(August 2022), 117357. https://doi.org/10.1016/j.jenvman.2023.117357

183. Zhou C, Yin K, Cao Y, et al (2018) Landslide susceptibility modeling applying machine learning methods: A case study from Longju in the Three Gorges Reservoir area, China. Comput Geosci 112:23–37. https://doi.org/10.1016/j.cageo.2017.11.019